Applications of Quantum Dots in Biology

An Overview

Charles Z. Hotz

- Size dependent emission spectra
- Single excitation
- Higher photostability
- Narrow emission peak
- Low toxicity for coated quantum dots

Nucleation and Growth of CdSe on ZnS Quantum Crystallite Seeds, and Vice Versa, in Inverse Micelle Media

A. R. Kortan, R. Hull, R. L. Opila, M. G. Bawendi, M. L. Steigerwald, P. J. Carroll, and L. E. Brus*

Contribution from AT&T Bell Laboratories, Murray Hill, New Jersey 07974.
Received June 20, 1989

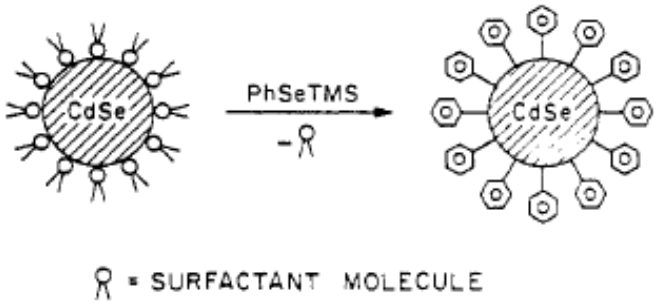

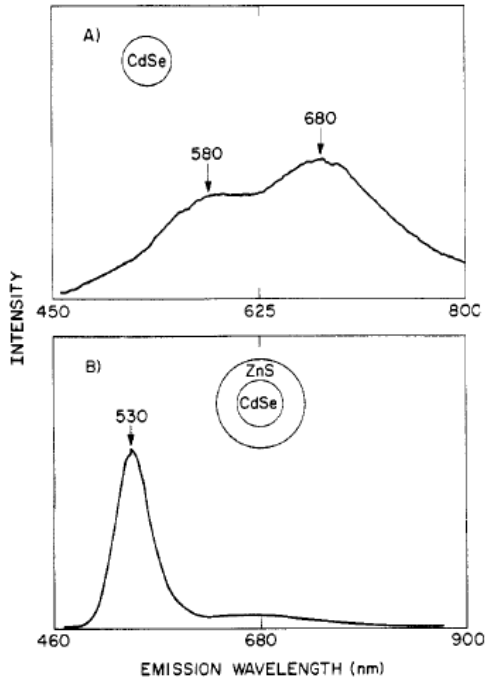

Figure 2. Room temperature luminescence spectra after annealing: (A) (CdSe)Ph, (B) $(CdSe)_1(ZnS)_4Ph$. The integrated quantum yield in B is more than an order of magnitude higher than in A.

Semiconductor Nanocrystals as Fluorescent Biological Labels

Marcel Bruchez Jr., Mario Moronne, Peter Gin, Shimon Weiss,*
A. Paul Alivisatos*

SCIENCE VOL 281 25 SEPTEMBER 1998

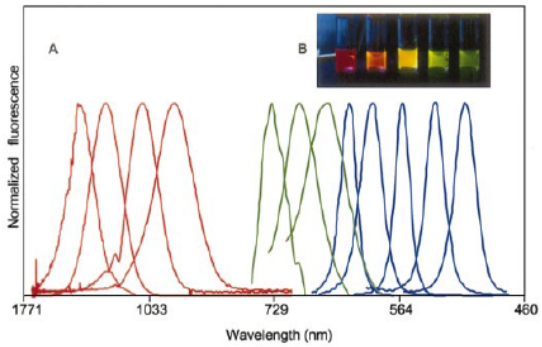

Fig. 2. (**A**) Size- and material-dependent emission spectra of several surfactant-coated semiconductor nanocrystals in a variety of sizes. The blue series represents different sizes of CdSe nanocrystals (*16*) with diameters of 2.1, 2.4, 3.1, 3.6, and 4.6 nm (from right to left). The green series is of InP nanocrystals (*26*) with diameters of 3.0, 3.5, and 4.6 nm. The red series is of InAs nanocrystals (*16*) with diameters of 2.8, 3.6, 4.6, and 6.0 nm. (**B**) A true-color image of a series of silica-coated core (CdSe)–shell (ZnS or CdS) nanocrystal probes in aqueous buffer, all illuminated simultaneously with a handheld ultraviolet lamp.

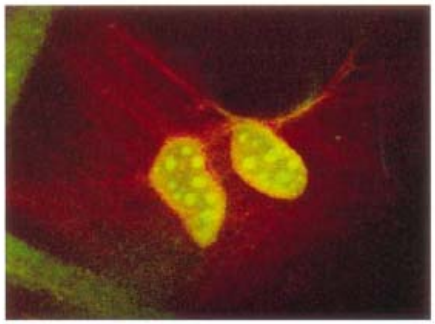

Fig. 3. Cross section of a dual-labeled sample examined with a Bio-Rad 1024 MRC laser-scanning confocal microscope with a 40× oil 1.3 numerical aperture objective. The mouse 3T3 fibroblasts were grown and prepared as described in (*27*). A false-colored image was obtained with 363-nm excitation, with simultaneous two-channel detection (522DF 35-nm FWHM narrow-pass filter for the green, and a 585-nm long-pass filter for the red). Image width: 84 μm.

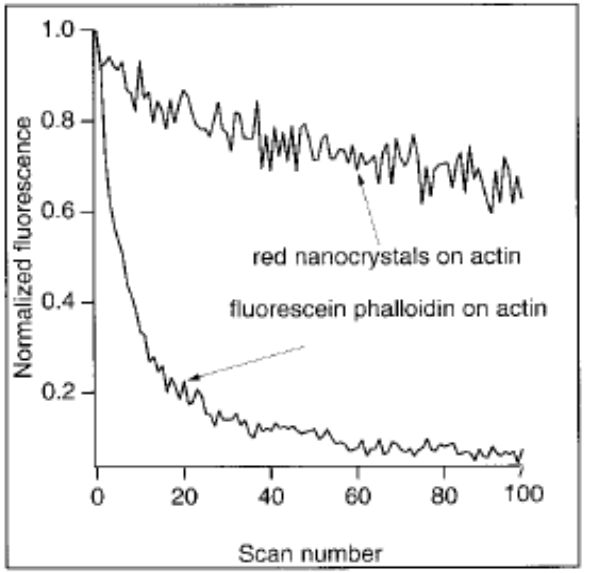

Fig. 4. Sequential scan photostability comparison of fluorescein-phalloidin–labeled actin fibers compared with nanocrystal-labeled actin fibers. Fluorescein was excited at 488 nm and the nanocrystals at 363 nm by a laser scanning confocal microscope with a 12-μs dwell time and ~20-mW power for each laser. The average intensity of four pixels was followed in each sample through 100 successive scans and normalized to its initial value. The intensity of the fluorescein drops quickly to autofluorescence levels, whereas the intensity of the nanocrystals drops only slightly.

Quantum Dot Bioconjugates for Ultrasensitive Nonisotopic Detection

Warren C. W. Chan and Shuming Nie*

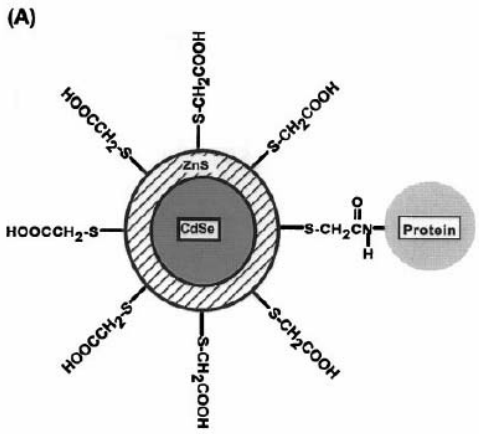

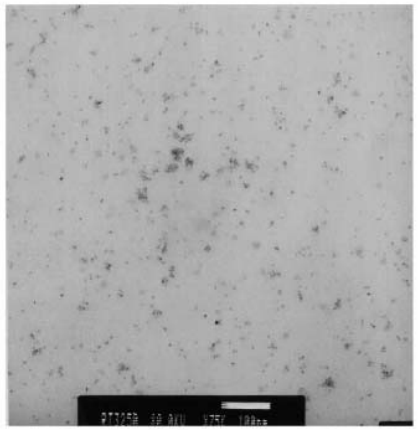

Fig. 1. (**A**) Schematic of a ZnS-capped CdSe QD that is covalently coupled to a protein by mercaptoacetic acid. (**B**) TEM of QD-transferrin (an iron-transport protein) conjugates. Scale bar, 100 nm. Clusters of closely spaced particles were mainly formed by sample spreading and drying on the carbon grid and not by chemical cross-linking. ZnS-capped QDs with a CdSe core size of 4.2 nm were prepared according to the procedure developed by Hines and Guyot-Sionnest (*7*). The colloidal QDs were dissolved in chloroform and were reacted with glacial mercaptoacetic acid (~1.0 M) for 2 hours. An aqueous phosphate-buffered saline (PBS) solution (pH 7.4) was added to this reaction mixture at a 1:1 volume ratio. After vigorous shaking and mixing, the chloroform and water layers separated spontaneously. The aqueous layer, which contained mercapto-coated QDs, was extracted. Excess mercaptoacetic acid was removed by four or more rounds of centrifugation. The purified QDs were conjugated to transferrin and IgG with the cross-linking reagent ethyl-3-(dimethyl-aminopropyl)carbodiimide. Standard protocols were followed (*16*), except the excess proteins were removed by repeated centrifugation. The purified conjugates were stored in PBS at room temperature.

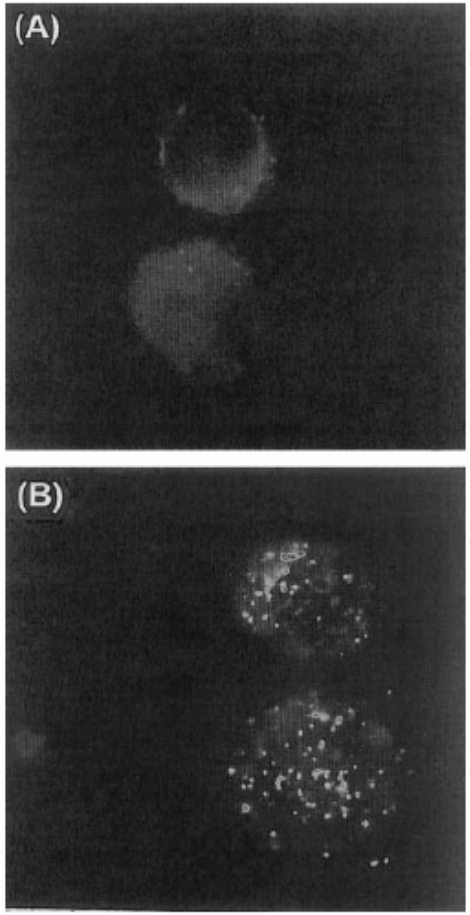

Fig. 4. Luminescence images of cultured HeLa cells that were incubated with (**A**) mercapto-QDs and (**B**) QD-transferrin conjugates. The QD bioconjugates were transported into the cell by receptor-mediated endocytosis and were detected as clusters or aggregates. Luminescence "blinking" was not observed for these clusters because of statistical averaging. The images were obtained with an epifluorescence microscope that was equipped with a high-resolution CCD camera (1.4 million pixels) (Photometrix, Tucson, Arizona) and a 100-W Hg excitation lamp. HeLa cells were grown in a minimum essential medium containing 10% fetal calf serum, 1% antibiotics (penicillin and streptomycin), and fungizone. The cultured cells were incubated overnight with either control QDs or the transferrin conjugates at 37°C. After repeated washings to eliminate excess QDs, the cells were removed from the petri dish and placed on a glass cover slip for imaging. The trypsin-treated cells had a spherical shape on the cover slip. Cell diameter, ~10 μm.

Optical Properties

- Broadband Absorption
  - Single laser excitation
- Sharp Emission
  - 20-30 nm symmetric emission
- High Quantum Yield
  - 20 x more than R6G
- Good Photostability
  - 100 x more stable for R6G (4 Hrs vs 10 mins)
- Loner fluorescent lifetime (20-40 ns vs 5 ns)

Structure

- Core quantum dot
  - CdSe, hydrophobic, not stable, lower QE (~5%)
  - Defects =>Trap state
- Core-shell quantum dot
  - ZnS/CdSe, hydrophobic, stable, higher QE (~50%)
  - Coated with higher bandgap materials or passivation reduces defects
- Water soluble quantum dot
  - Hydrophilic polymer coating
- Quantum dot bioconjugation
  - Bioconjugate to hydrophilic quantum dot

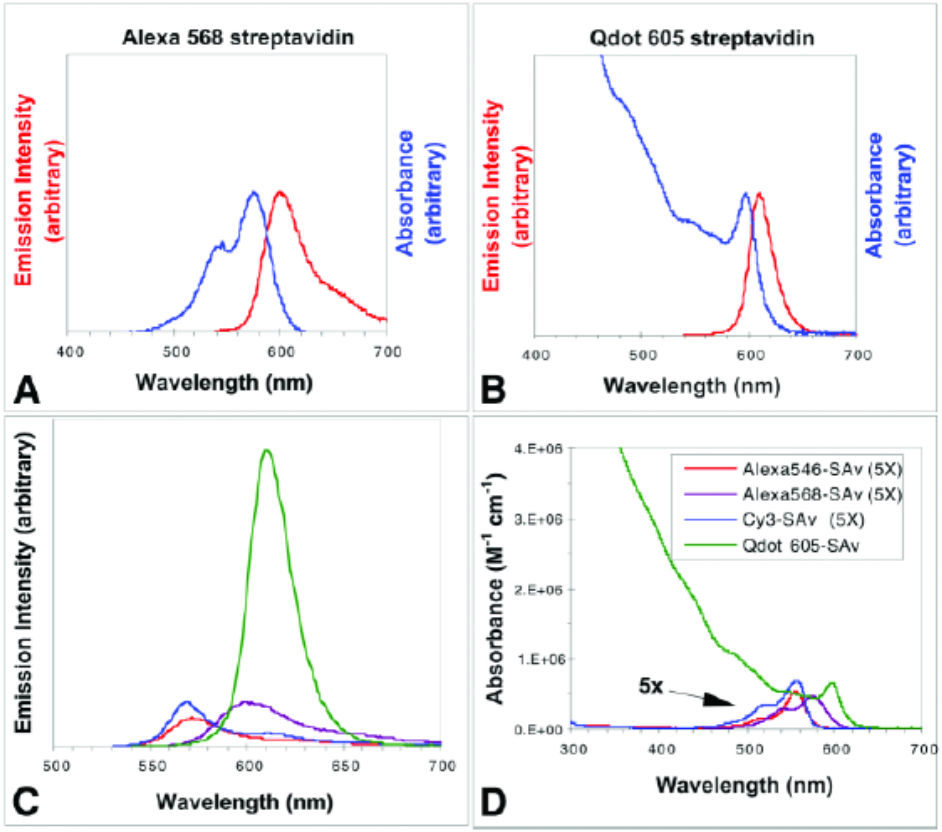

Fig. 1. Comparison of absorbance and emission spectra (normalized) of **(A)** Alexa® 568 streptavidin conjugate and **(B)** Qdot® 605 streptavidin conjugate. Note that the quantum dot conjugate can absorb light efficiently far to the blue of the emission. **(C)** Comparison of emission spectra (nonnormalized) of streptavidin conjugates of Qdot 605 (—), Alexa 546 (—), Alexa 568 (—), and Cy3® (—). The spectra were taken under conditions in which each fluorophore absorbed the same amount of excitation light. The measured quantum yields of the conjugates were 55, 8, 16, and 11%, respectively. **(D)** Comparison of absorbance spectra (nonnormalized, each 1 μ*M* flurophore) of Qdot 605 streptavidin conjugate (—), Cy3 streptavidin conjugate (—), Alexa 546 streptavidin conjugate (—), and Alexa 568 streptavidin conjugate (—). Note that all dye spectra are enhanced fivefold for clarity. Alexa, Cy3, and Qdot are registered trademarks of Molecular Probes, Amersham Biosciences, and Quantum Dot Corporation, respectively.

Table 1
Optical Properties of Quantum Dots Compared to Common Dyes[a]

Fluorescent dye	$\lambda_{excitation}$ (nm)	$\lambda_{emission}$ (nm)	$\varepsilon(mol^{-1}\text{-}cm^{-1})$
Qdot 525	400	525	280,000
Alexa 488	495	519	78,000
Fluorescein	494	518	79,000
Qdot 565	400	565	960,000
Cy3	550	570	130,000
Alexa 555	555	565	112,000
Qdot 585	400	585	1,840,000
R-Phycoerythrin	565	578	1,960,000
TMR	555	580	90,000
Qdot 605	400	605	2,320,000
Alexa 568	578	603	88,000
Texas Red	595	615	96,000
Qdot 655	400	655	4,720,000
APC	650	660	700,000
Alexa 647	650	668	250,000
Cy5	649	670	200,000
Alexa 647-PE	565	668	1,960,000

[a]The extinction coefficients (ε) are generally much larger for quantum dots than for fluorescent dyes. Furthermore, the excitation wavelength ($\lambda_{excitation}$) can be much farther from the emission ($\lambda_{emission}$).

Photo Stability

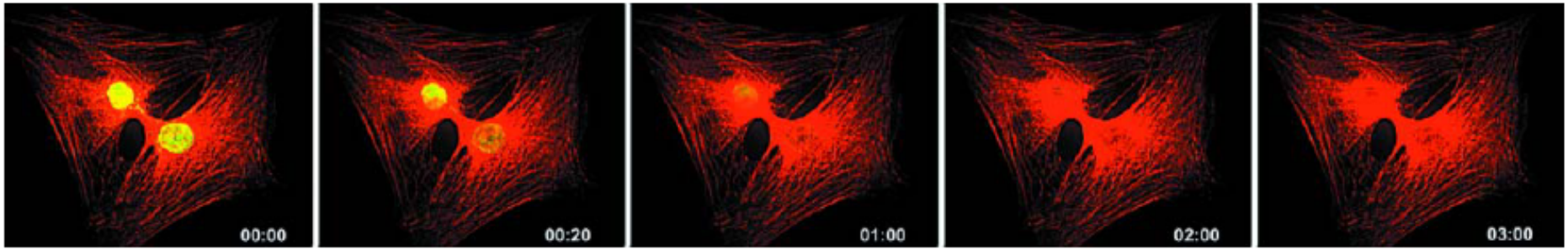

Fig. 2. Comparison of photostability between Qdot® 605 and Alexa Fluor® 488 streptavidin conjugates. Actin filaments in two 3T3 mouse fibroblast cells were labeled with Qdot 605 streptavidin conjugate (red), and the nuclei were stained with Alexa Fluor 488 streptavidin (green). The specimens were continuously illuminated for 3 min with light from a 100-W mercury lamp under a ×100 1.30 oil objective. An excitation filter (excitation: 485 ± 20 nm) was used to excite both Alexa 488 and Qdot 605. Emission filters (emission: 535 ± 10 and em 605 ± 10 nm) on a motorized filter wheel were used to collect Alexa 488 and Qdot 605 signals, respectively. Images were captured with a cooled charge-coupled device camera at 10-s intervals for each color automatically. Images at 0, 20, 60, 120, and 180 s are shown. Whereas Alexa 488 labeling signal faded quickly and became undetectable within 2 min, the Qdot 605 signal showed no obvious change for the entire 3-min illumination period.

QD Blinking

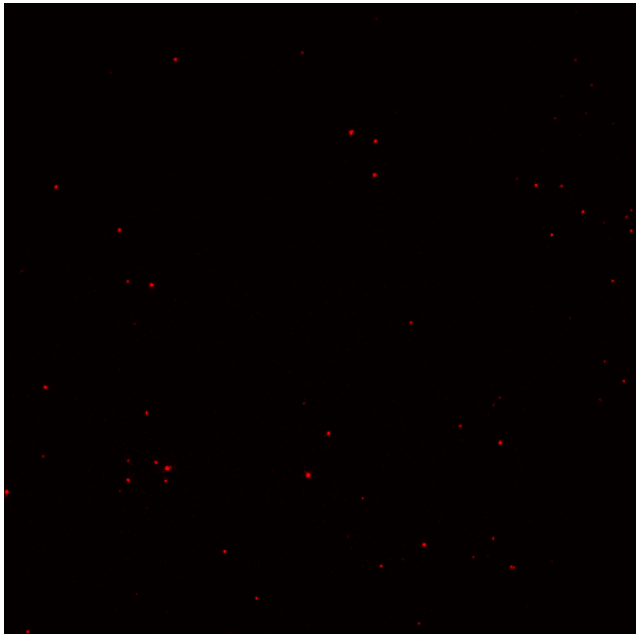

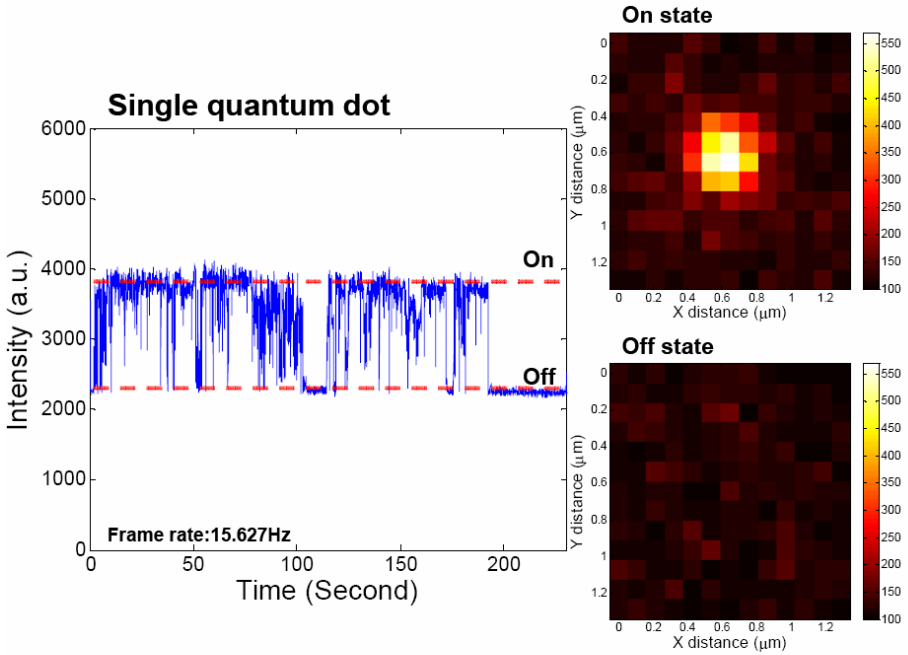
Single quantum dot
Intensity (a.u.)
Time (Second)
Frame rate:15.627Hz
On
Off
On state
Off state
Y distance (μm)
X distance (μm)

Near-Complete Suppression of Quantum Dot Blinking in Ambient Conditions

Sungchul Hohng, and Taekjip Ha

J. Am. Chem. Soc., **2004**, 126 (5), 1324-1325• DOI: 10.1021/ja039686w • Publication Date (Web): 20 January 2004

140 mM BME

β-mercaptoethanol

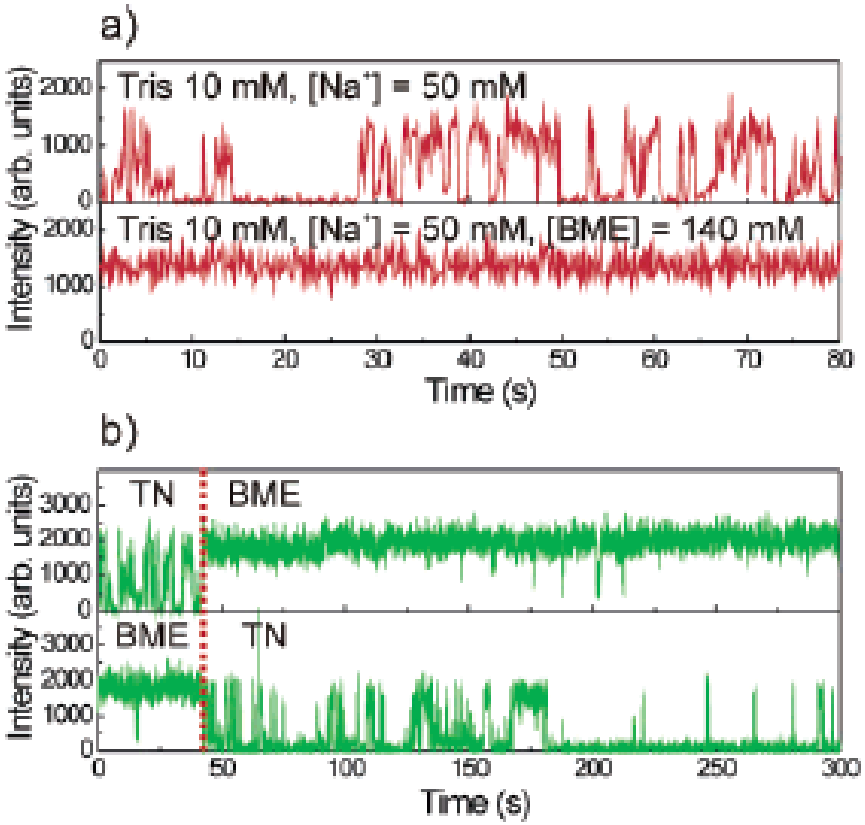

Multiplexing by Q-dot

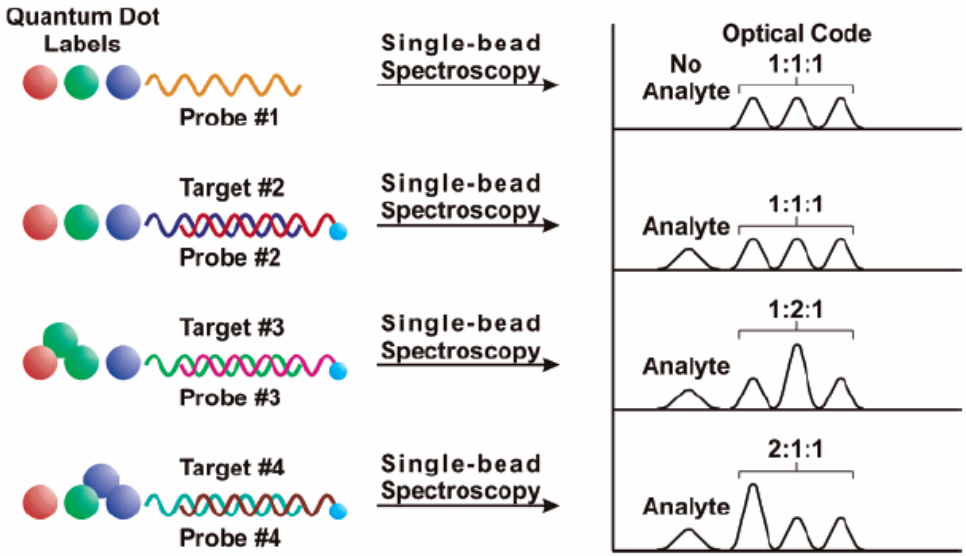

Figure 3. Quantum dots can be employed for detecting multiple targets in a single assay. Specifically, varying the numbers and ratios of different quantum dots per target results in a unique fluorescent signal for each individual target. (Reprinted with permission of Nature Publishing Group. *Nature Biotech.*, Vol. 19, 2001, by Nie, et al.)

Encoding

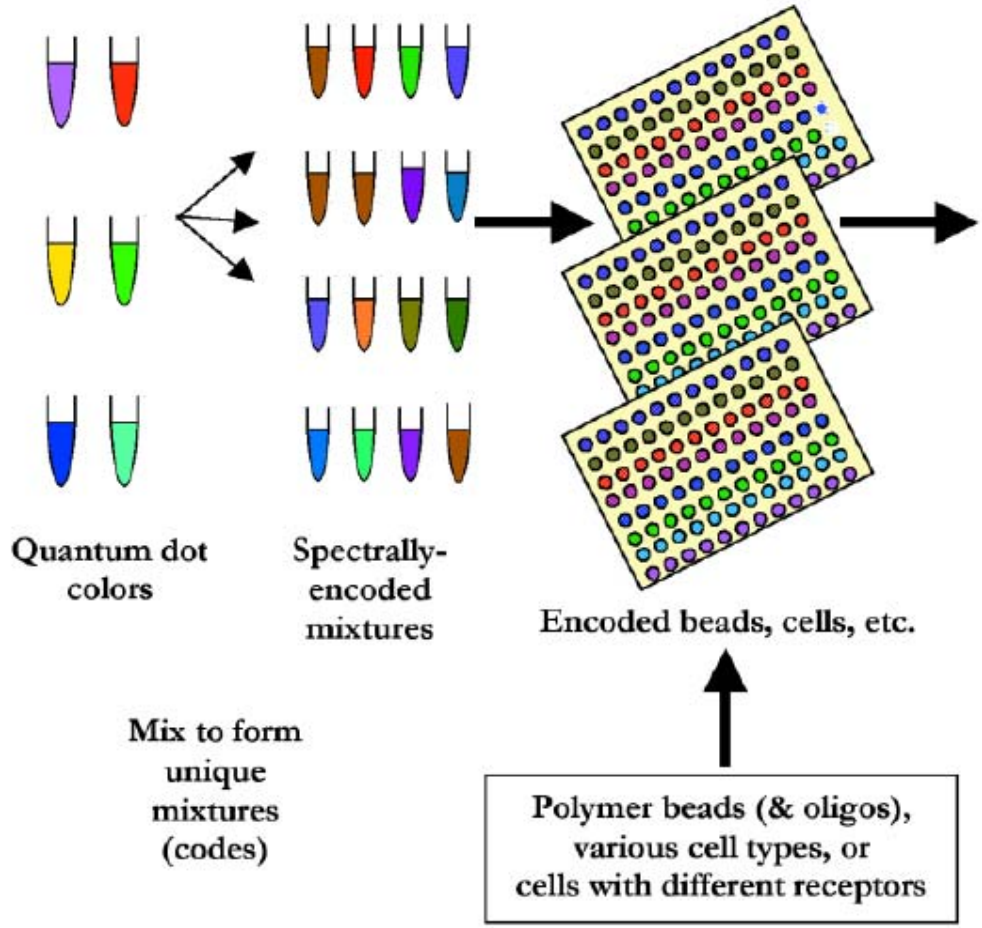

Application	Format
Multiplexed gene expression	Encoded beads each with gene-specific oligos
Multiplexed SNP genotyping	Encoded beads with allele-specific oligos
Multiplexed immunoassays	Encoded beads with antibodies
Multiplexed cell-based assays	Mixed cell types encoded with quantum dots
Multiplexed reporter assays	Encoded cell lines expressing various receptors

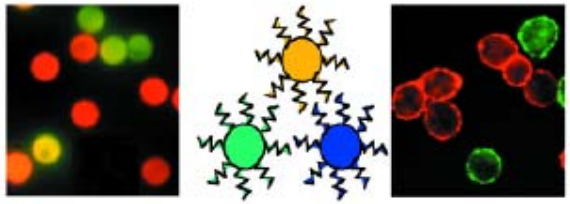

Fig. 6. Concept of encoding using quantum dots. Quantum dot colors can be mixed to produce spectral codes. These mixtures can be combined with polymer beads to produce encoded beads that can be subsequently coupled to distinct oligonucleotides or other affinity molecules. Alternatively, the quantum dot spectral codes can be used to label cells to differentiate cell lines, or cell lines bearing different receptors. SNP, single nucleotide polymorphism.

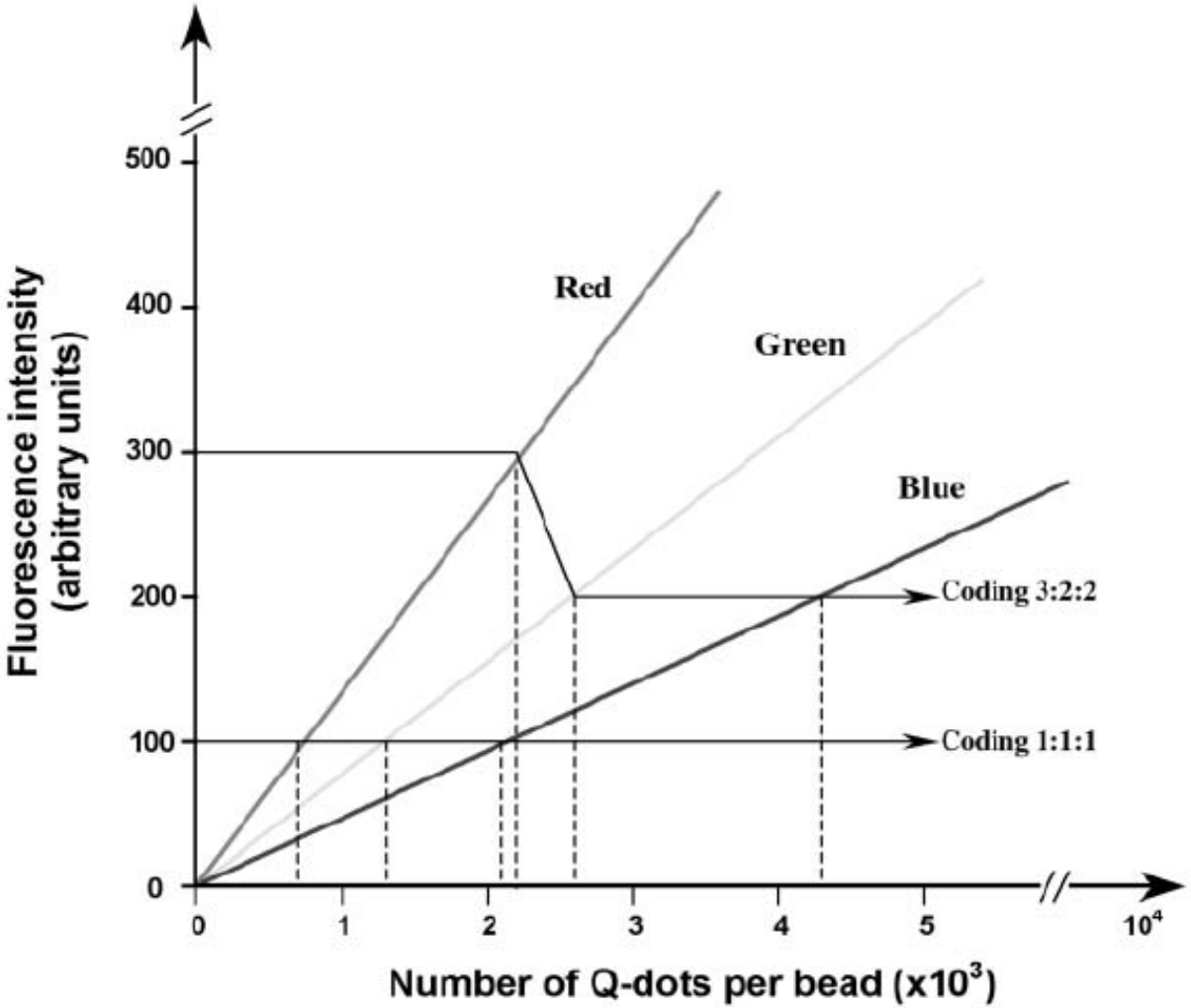

Fig. 1. Schematic drawing of working curves for preparation of multicolor quantum dot microbeads. Arrows depict two representative beads coded with intensity ratios of 1 : 1 : 1 and 3 : 2 : 2, and the number of quantum dots (or concentration) can be obtained from the x axis. Each single bead may contain quantum dots (Q-dots) ranging from several hundred to millions, depending on the bead size and surface area.

Quantum Dot Bio-conjugation

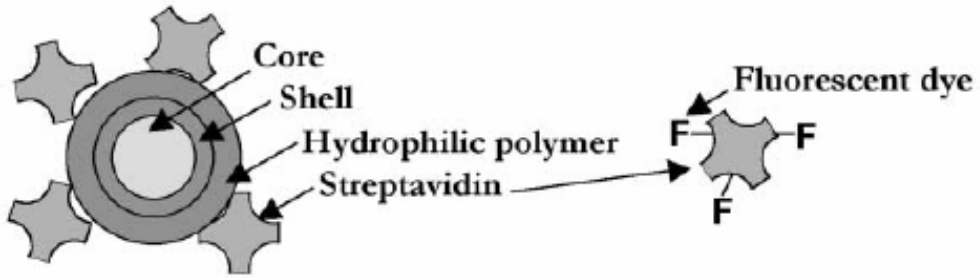

Fig. 3. Schematic of Qdot™ Nanocrystal Probe compared to a typically labeled fluorescent dye protein conjugate (see text for descriptions). Proteins generally carry several fluorescent dye labels (F). By contrast, each quantum dot is conjugated to multiple protein molecules.

Q-dot Aggregation

Clustering

Non-Clustering

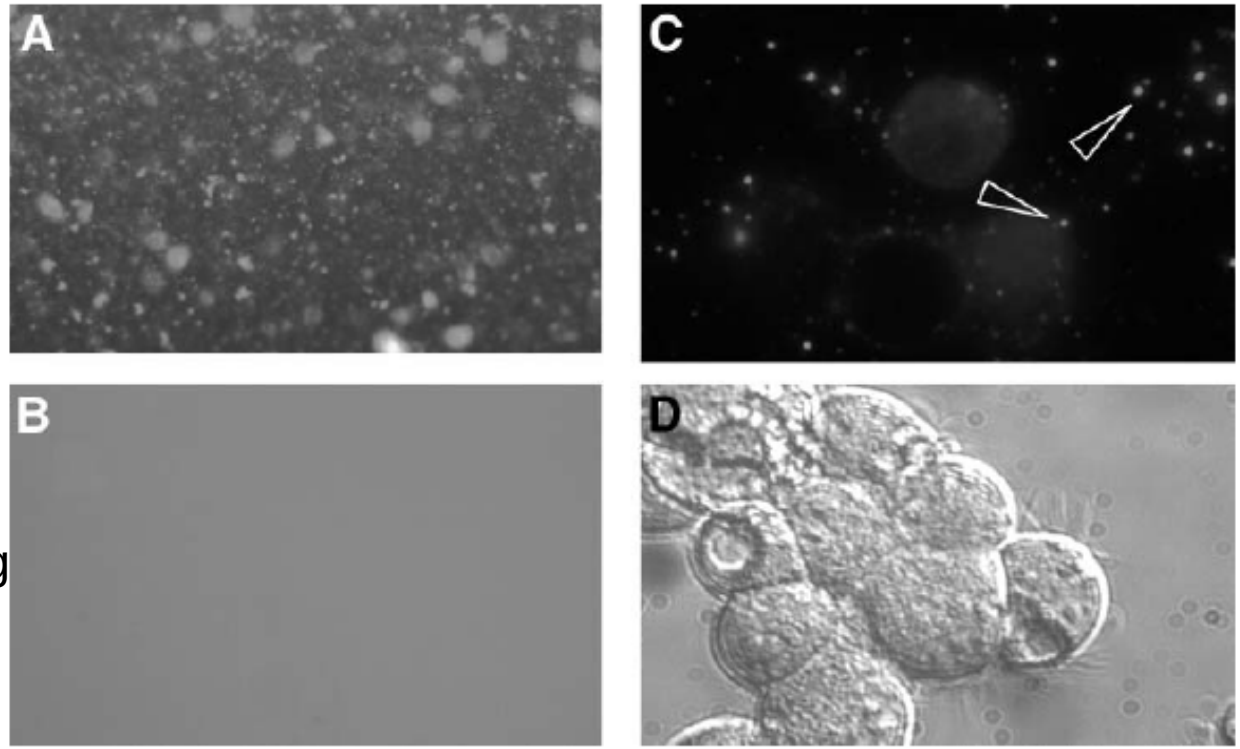

Clustering

Fig. 4. Evidence for quantum dot aggregation (magnification: ×40): **(A)** fluorescent image of aggregated SA-quantum dots in absence of cells; **(B)** image of nonaggregated SA-quantum dots in absence of cells; **(C)** image of cells surrounded by aggregated SA-quantum dots (arrowheads); **(D)** bright-field image.

Biotinylated Cell

Cell + Biotin

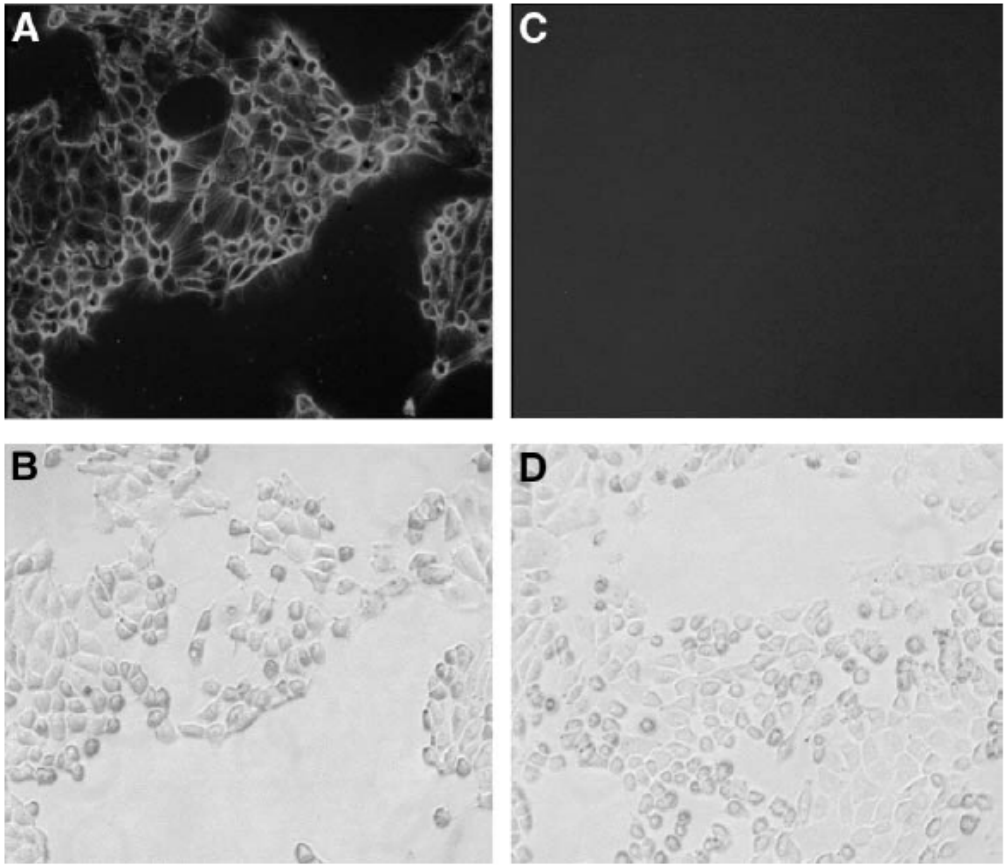

Fig. 1. Labeling of biotinylated HEK293 cells with SA-quantum dots (magnification: ×10). Three-day-old HEK293 cells cultured on poly-D-lysine glass-bottomed microwell dishes were biotinylated as described in **Subheading 3.2.1.** **(A,B)** Biotinylated HEK293 cells incubated with SA-quantum dots (50 n*M*); **(C,D)** biotinylated HEK293 cells labeled with SA-quantum dots after preincubating with 2 mg/mL of biotin.

Q-dot Antibody Labeling

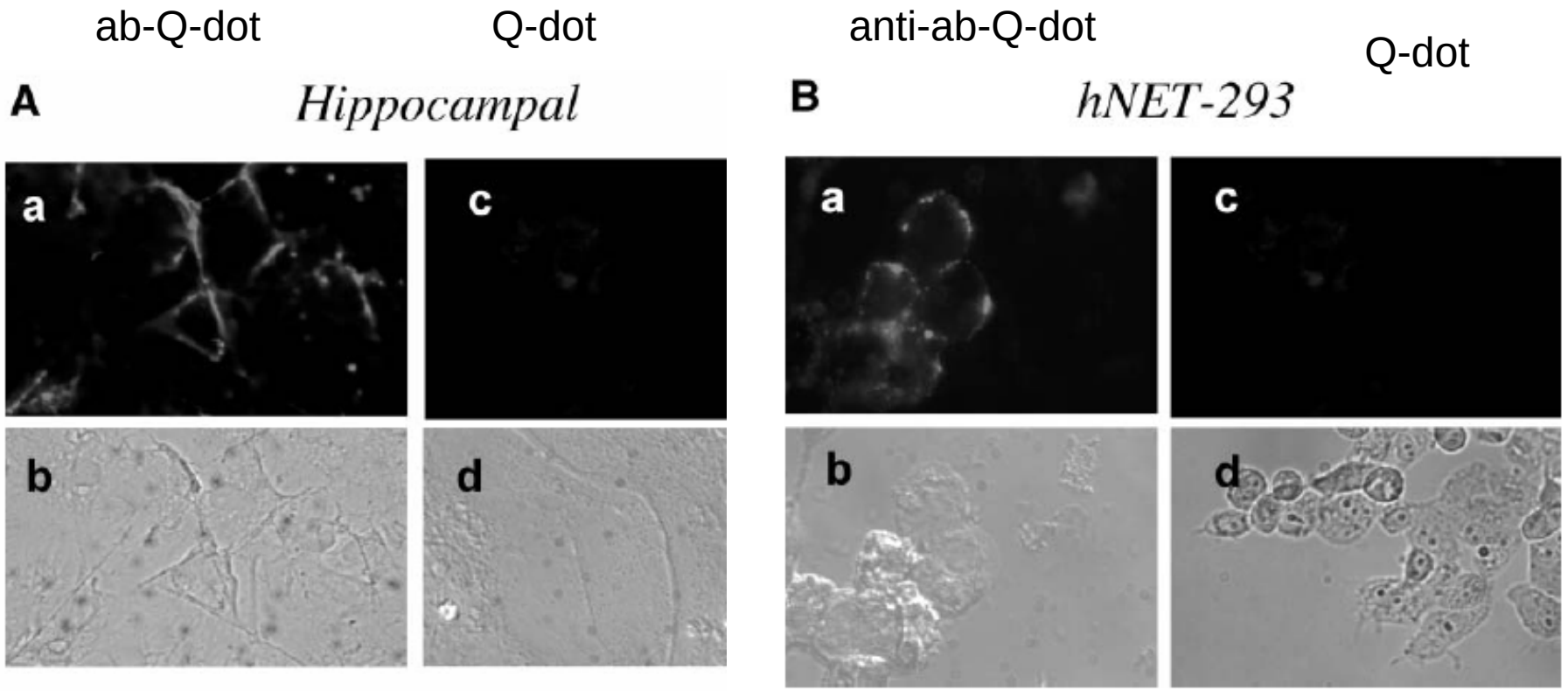

Fig. 5. SA-quantum dots and SA-Alexa Red recognize biotin-modified antibody-labeled cultures. **(A)** Eight-day-old *fixed* primary hippocampal cultures incubated with anti-LAMP followed by SA-quantum dots (a, b) or SA-quantum dots alone (c, d); **(B)** labeling of live hNET-293 cells with anti-hNET + biotinylated anti-rabbit IgG followed by SA-quantum dots (a, b) or SA-quantum dots alone (c, d).

Intracellular Delivery of Quantum Dots for Live Cell Labeling and Organelle Tracking**

By *Austin M. Derfus, Warren C. W. Chan*, and *Sangeeta N. Bhatia**

- Adv. Mater. 2004,16, no.12,961

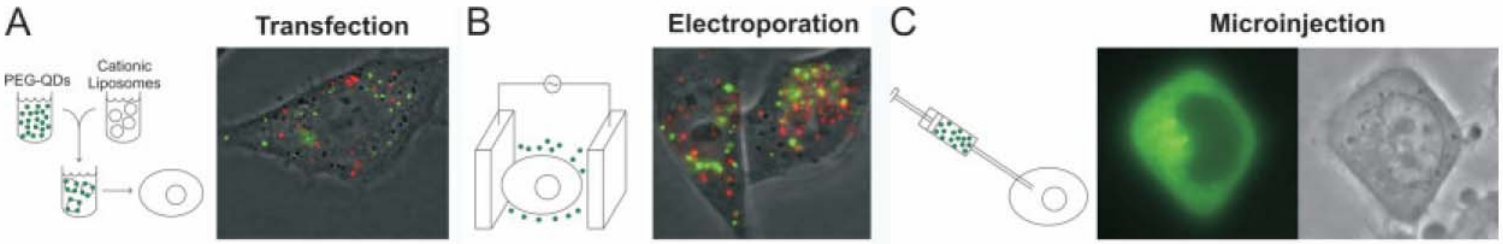

(1)23mer nuclear localization sequence peptide from SV40 T antigen plus additional residues.

(2) 28mer mitochondrial localization sequence peptide

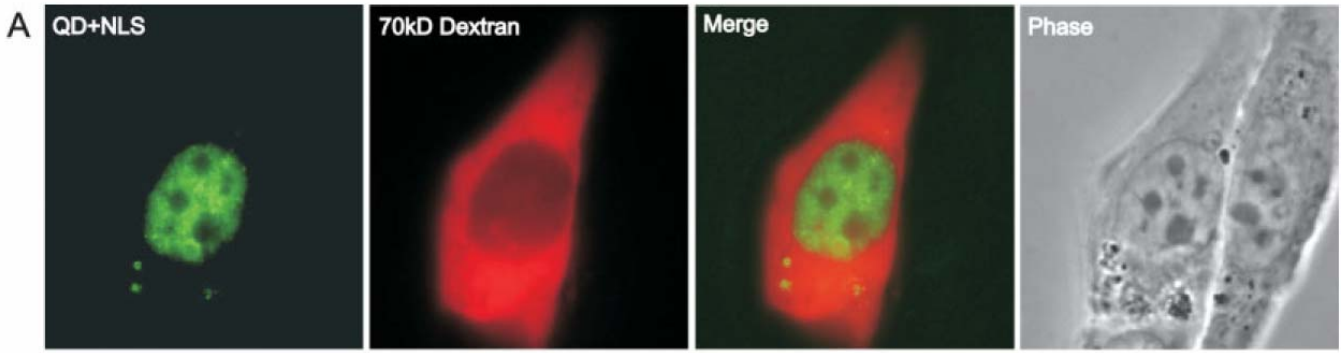

Microbiol. Immunol., **48**(12), 985–994, 2004

Editor-Communicated Paper

Quantum Dots Targeted to the Assigned Organelle in Living Cells

QDs conjugated with (1)nuclear- and(2) mitochondria-targeting ligands.

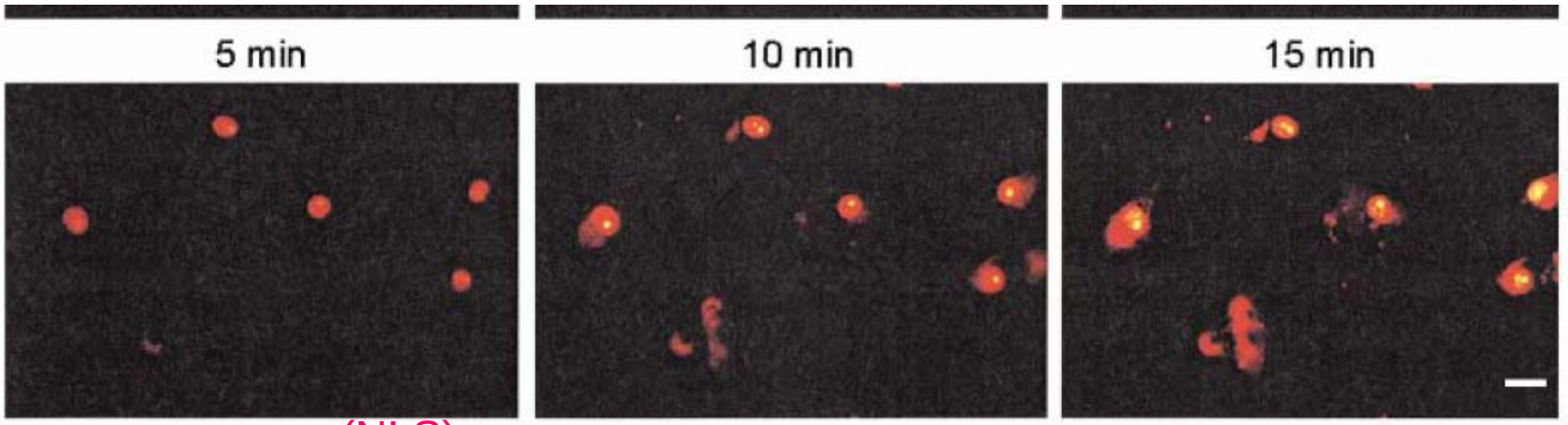

(NLS)

Fig. 3. Localization of R_{11}KC-conjugated QDs to nucleus. (a) Cells were pre-stained with Hoechst®33342, and stimulated with FITC-labeled QD-conjugated R_{11}KC peptide (1 μM final) for 3 hr at 37 C with 5% CO_2 condition. (b) Cells were pre-stained with Hoechst®33342, and stimulated with QD-R^{11}KC (1 μM final) for the indicated time at 37 C under 5% CO_2 condition with a culture fluorescence microscope (IM-310 system, Olympus). Images were taken using D1X digital camera (Nikon) equipped with IM-310 system at the indicated time by a 3 sec exposure. Bars indicated 10 μm.

1176 *Bioconjugate Chem.* **2005,** *16,* 1176–1180

Tat Peptide as an Efficient Molecule To Translocate Gold Nanoparticles into the Cell Nucleus

Jesus M. de la Fuente*,§ and Catherine C. Berry

Centre for Cell Engineering, Institute of Biomedical and Life Science, Joseph Black Building, University of Glasgow, Glasgow G12 8QQ, U.K Received February 9, 2005; Revised Manuscript Received June 10, 2005

- We report in this article the synthesis of water-soluble gold nanoparticles functionalized with a Tat protein-derived peptide sequence

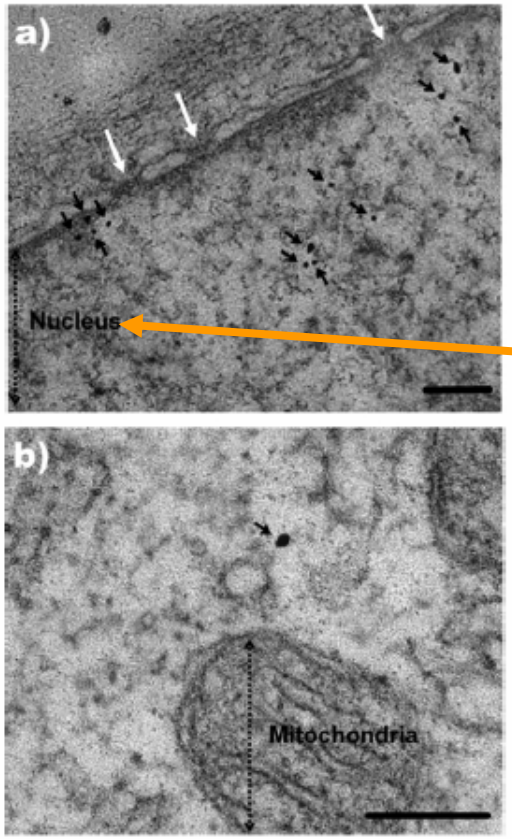

Figure 3. Transmission electron micrographs of human fibroblasts incubated with **Au@Tat** (a) and **Au@tiopronin** (b) nanoparticles. The black dots indicated with arrows are nanoparticles, and white arrows show nuclear membrane pores. (scale bars = 50 nm).

Au@tiopronin with the Tat protein-derived sequence (GRKKRRQRRR) was carried out using the reactivity of the free carboxyl group of the tiopronin (Scheme 1).

the specificity of **Au@Tat** particles to be translocated and accumulate in the cell nucleus.

Cellular Trajectories of Peptide-Modified Gold Particle Complexes: Comparison of Nuclear Localization Signals and Peptide Transduction Domains

Alexander G. Tkachenko, Huan Xie, Yanli Liu, Donna Coleman, Joseph Ryan, Wilhelm R. Glomm, Mathew K. Shipton, Stefan Franzen,* and Daniel L. Feldheim*

Table 1. Peptide Sequences Used in Nanoparticle−BSA−Peptide Complexes[a]

no.	peptide sequence	origin of peptide	nuclear localization prediction, %	cytoplasm localization prediction, %
M1	CGGGPKKKRKVGG	SV40 large T NLS	82.6	13
M2	CGGRKKRRQRRRAP	HIV-1 Tat protein NLS	73.9	21.7
M3	CGGFSTSLRARKA	adenoviral NLS	47.8	47.8
M4	CKKKKKKGGRGDMFG	integrin binding domain and oligolysine	73.9	17.4

Table 3. Location of Peptide-Coated Nanoparticles after 3-h Incubation Times with Various Cell Lines

no.	peptide sequence	HeLa	3T3/NIH	HepG2
M1	CGGGPKKKRKVGG	cytoplasm	cytoplasm	cytoplasm
M2	CGGRKKRRQRRRAP	cytoplasm	no uptake	cytoplasm
M3	CGGFSTSLRARKA	nucleus	cytoplasm	no uptake
M4	CKKKKKKGGRGDMFG	nucleus	cytoplasm	nucleus

Self-Assembled Quantum Dot–Peptide Bioconjugates for Selective Intracellular Delivery

James B. Delehanty,[†,*] Igor L. Medintz,[†] Thomas Pons,[‡,||] Florence M. Brunel,[§] Philip E. Dawson,[§] and Hedi Mattoussi[‡,*]

- The polyhistidine sequence allows the peptide to self-assemble onto the QD surface via metal-affinity interactions, -
- (2) CdSe- Zns QDs- HIV 1

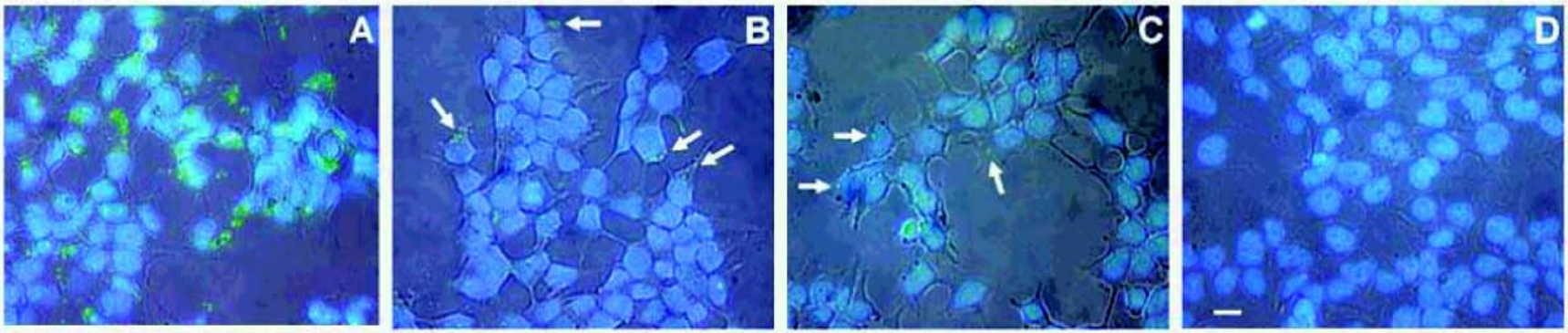

Figure 2. Dose-dependent cellular internalization of QD–CPP assemblies. HEK 293T/17 cells were incubated with 510-nm QD–CPP assemblies (QD:CPP ratio 1:50) at QD concentrations of 250 nM (A), 60 nM (B), 15 nM (C), or with 250 nM QDs without CPP (D); cells were also stained with DAPI. Overlay of phase contrast, QD fluorescence (green), and DAPI fluorescence (blue), show the dose-dependent nature of the QD–CPP delivery. Images also show that QD staining is nonnuclear, punctate fluorescence located in the cytoplasm. Negligible cell-surface associated fluorescence was observed. Arrows indicate regions of QD–CPP internalization at lower concentrations. Scale bar is 10 μm.

Figure 3. QD-CPP internalization and colocalization within endocytotic vesicles.

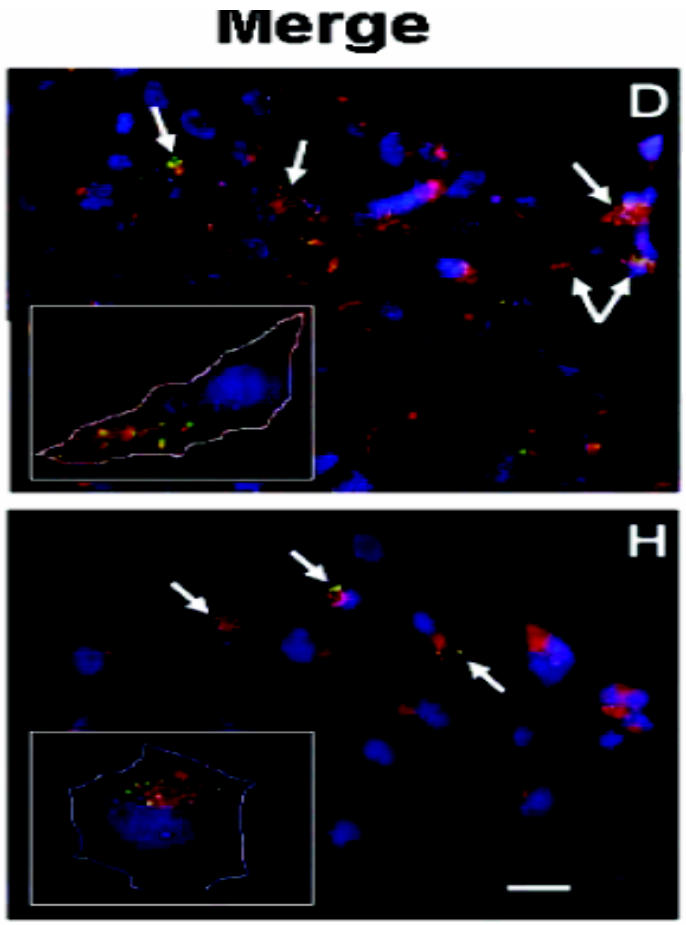

920 *Bioconjugate Chem.* **2006**, *17*, 920–927

Self-Assembled Quantum Dot−Peptide Bioconjugates for Selective Intracellular Delivery

James B. Delehanty,[†,*] Igor L. Medintz,[†] Thomas Pons,[‡,||] Florence M. Brunel,[§] Philip E. Dawson,[§] and Hedi Mattoussi[‡,*]

QDs –peptides assemlies were colocalized within endosomes.

Multifunctional Gold Nanoparticle–Peptide Complexes for Nuclear Targeting

Alexander G. Tkachenko, Huan Xie, Donna Coleman, Wilhelm Glomm, Joseph Ryan, Miles F. Anderson, Stefan Franzen,* and Daniel L. Feldheim*

- JACS,2003, 125, 4700

Table 1. Peptide Sequences Used in Nanoparticle–BSA–Peptide Complexes[a]

#	peptide sequence	origin of peptide	peptide/BSA
1	CGGGPKKKRKVGG	SV40 large T NLS	7 ± 1
2	CGGFSTSLRARKA	adenoviral NLS	8 ± 1
3	CKKKKKKSEDEYPYVPN	adenoviral RME	9 ± 2
4	CKKKKKKKSEDEYPYVP-NFSTSLRARKA	adenoviral fiber protein	6 ± 2

NLS RME

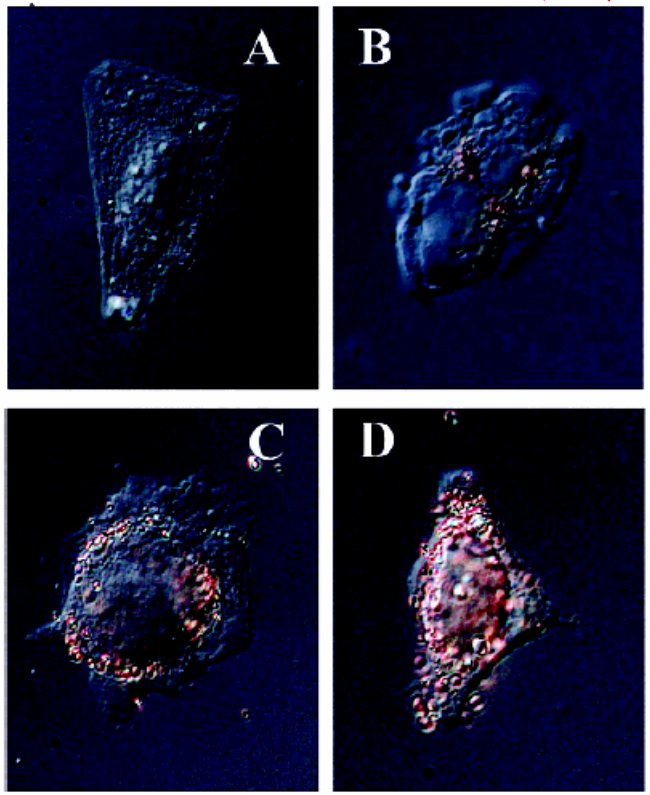

Figure 1. Nanoparticle−peptide complexes incubated with HepG2 cells for 2 h: #2 (A), #3 (B), #4 (C), and #2/#3 (D). The HepG2 cell line was

NLS+RME

Feldherr has shown that peptide #1, the NLS from SV-40 virus, is translocated to the nucleus when attached to gold nanoparticles, if the particles are injected into the cytoplasm.2e

Surprisingly, when these complexes were added to cell growth media, they were found inside the cytoplasm of HepG2 cells; however, they did not enter the nucleus.

- JACS,2003, 125, 4700

Fluorescent CdSe/ZnS Nanocrystal–Peptide Conjugates for Long-term, Nontoxic Imaging and Nuclear Targeting in Living Cells

Fanqing Chen, and Daniele Gerion

Nano Letters, **2004**, 4 (10), 1827-1832• DOI: 10.1021/nl049170q • Publication Date (Web): 09 September 2004

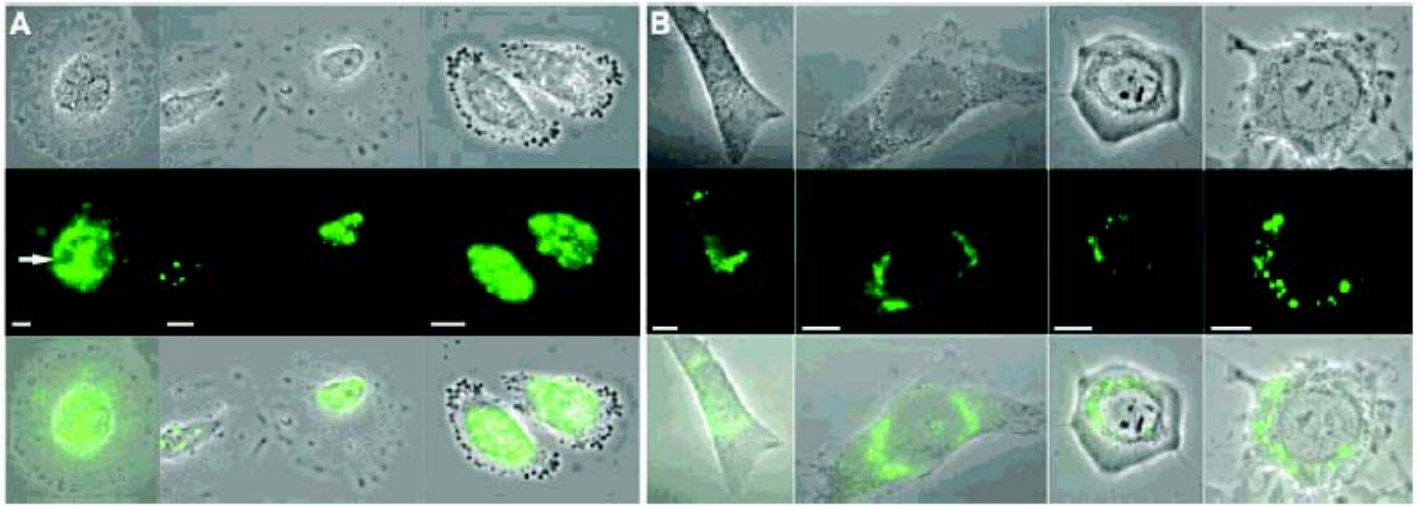

Figure 2. Localization of NLS−qdots in the nucleus (A) or in the perinuclear region (B). In both panels, the top row represents the phase

The NLS-qdot conjugates are observed either in the cell nucleus (Figure 2, panel A) or in the perinuclear region (Figure 2, panel B).

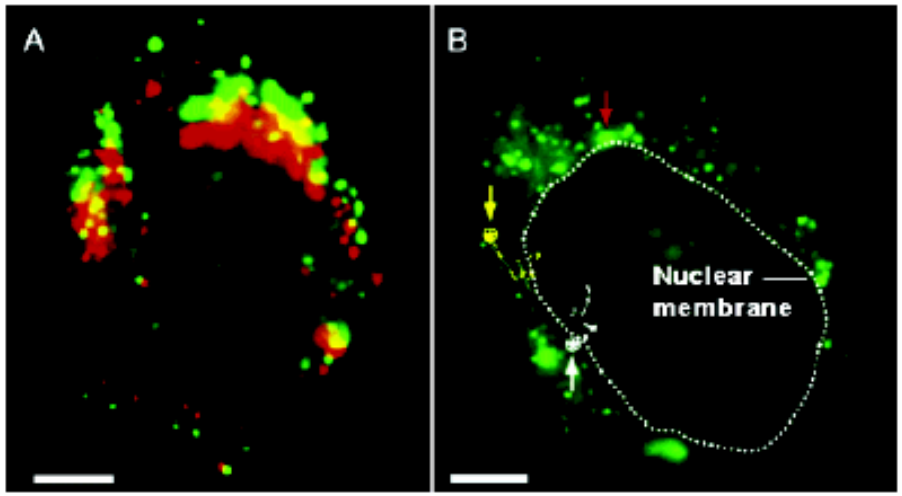

Figure 4. Movement of NLS−qdot conjugates. (A) False-color overlay of fluorescence from a cell taken at 4 min intervals, about 2 h after transfection. In 4 min, the dots moved from the green to the red position. The features at the top of the image go downward and the features on the bottom go upward. Notice the movement of the fluorescent dots at the bottom of the image toward the nucleus. Integration time: 700 ms. (B) An example of a large aggregate of NLS−qdots is indicated with the red arrow. This feature is immobile during the entire period of illumination (15 min). In contrast, smaller, weaker, blurred yet distinguishable features move continuously during the measurement. The pathways of two of these spots are shown. The positions of the spots at the beginning of the measurement are indicated by the circled stars and the arrows. Positions are determined every 15 s for a total time of 15 min. Integration time: 500 ms/frame. Scale bar: 5 μm.

The general direction of movements of the NLS-qdots goes from the periphery of the cytoplasm to the perinuclear region (Figure 4A).

Foster Resonance Energy Transfer (FRET)

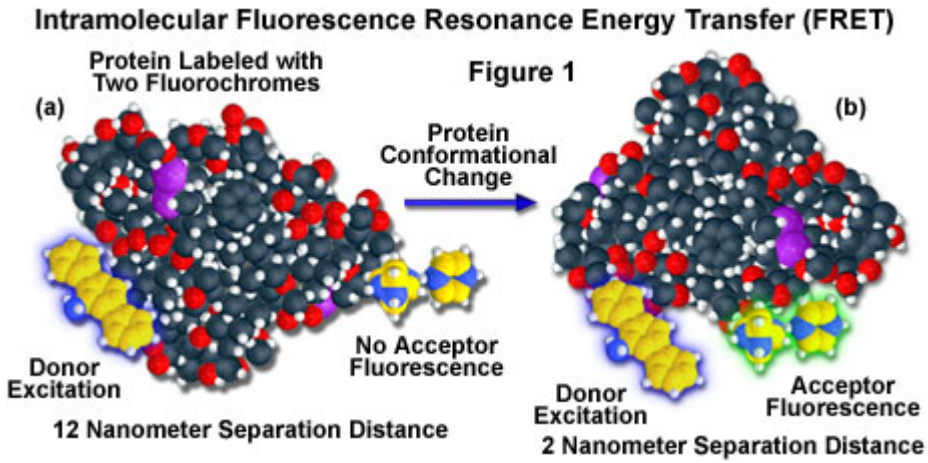

$$E = \frac{k_{ET}}{k_f + k_{ET} + \sum k_i}$$

$$E = \frac{1}{1 + (r/R_0)^6}$$

FRET

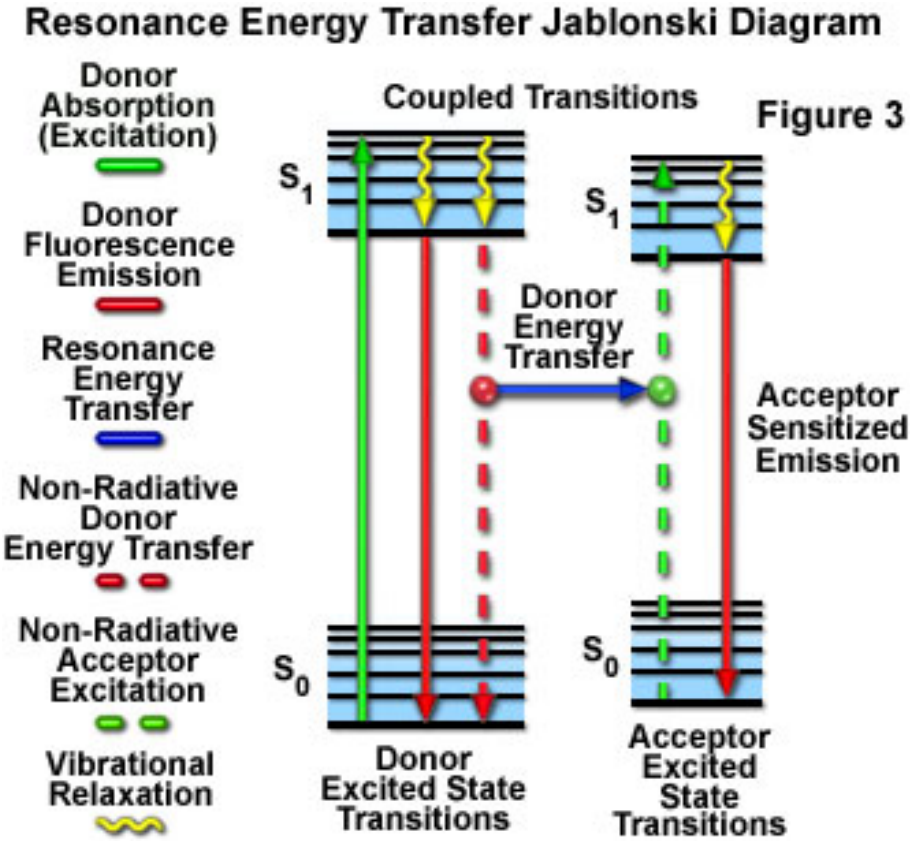

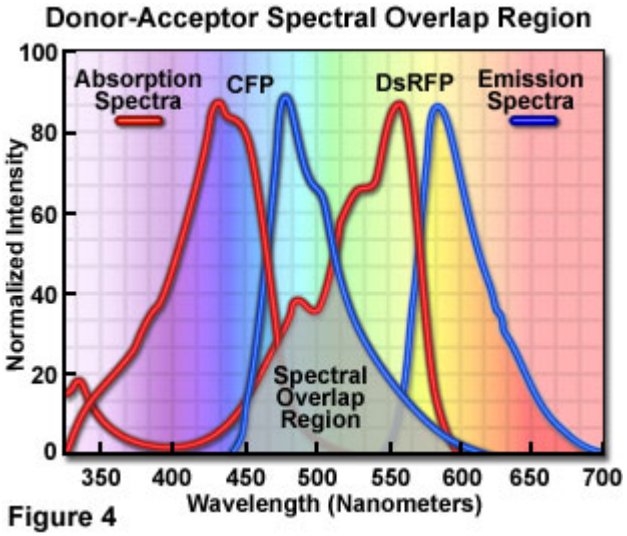

Figure 4

FRET

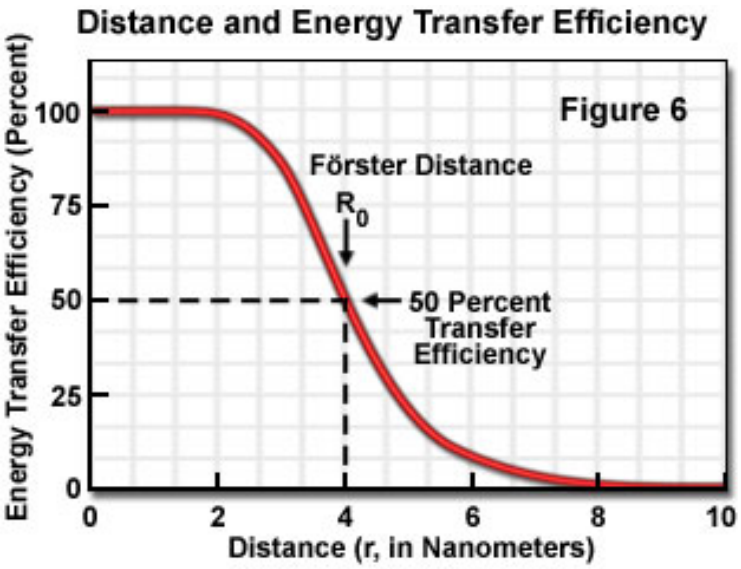
Distance and Energy Transfer Efficiency
Figure 6
Förster Distance
R_0
50 Percent Transfer Efficiency
Energy Transfer Efficiency (Percent)
100
75
50
25
0
0
2
4
6
8
10
Distance (r, in Nanometers)

2-8 nm

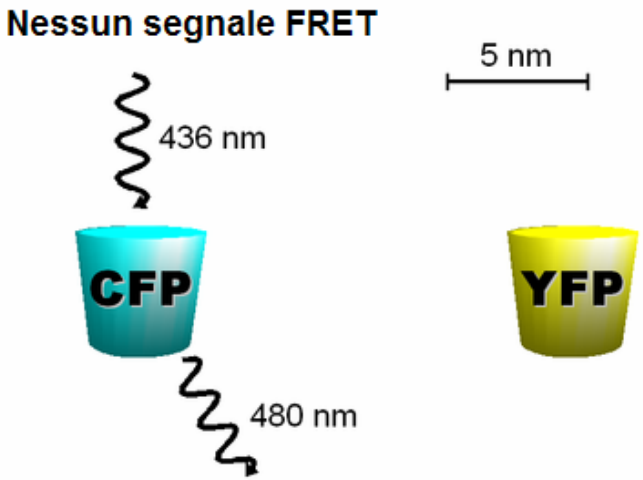
Nessun segnale FRET
5 nm
436 nm
CFP
YFP
480 nm

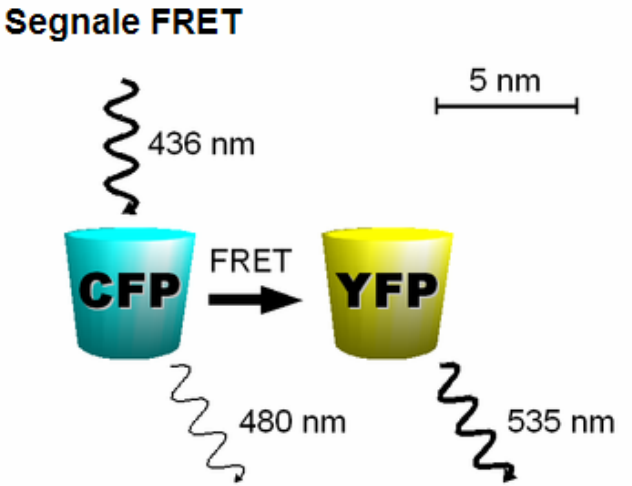
Segnale FRET
5 nm
436 nm
CFP
FRET
YFP
480 nm
535 nm

FRET

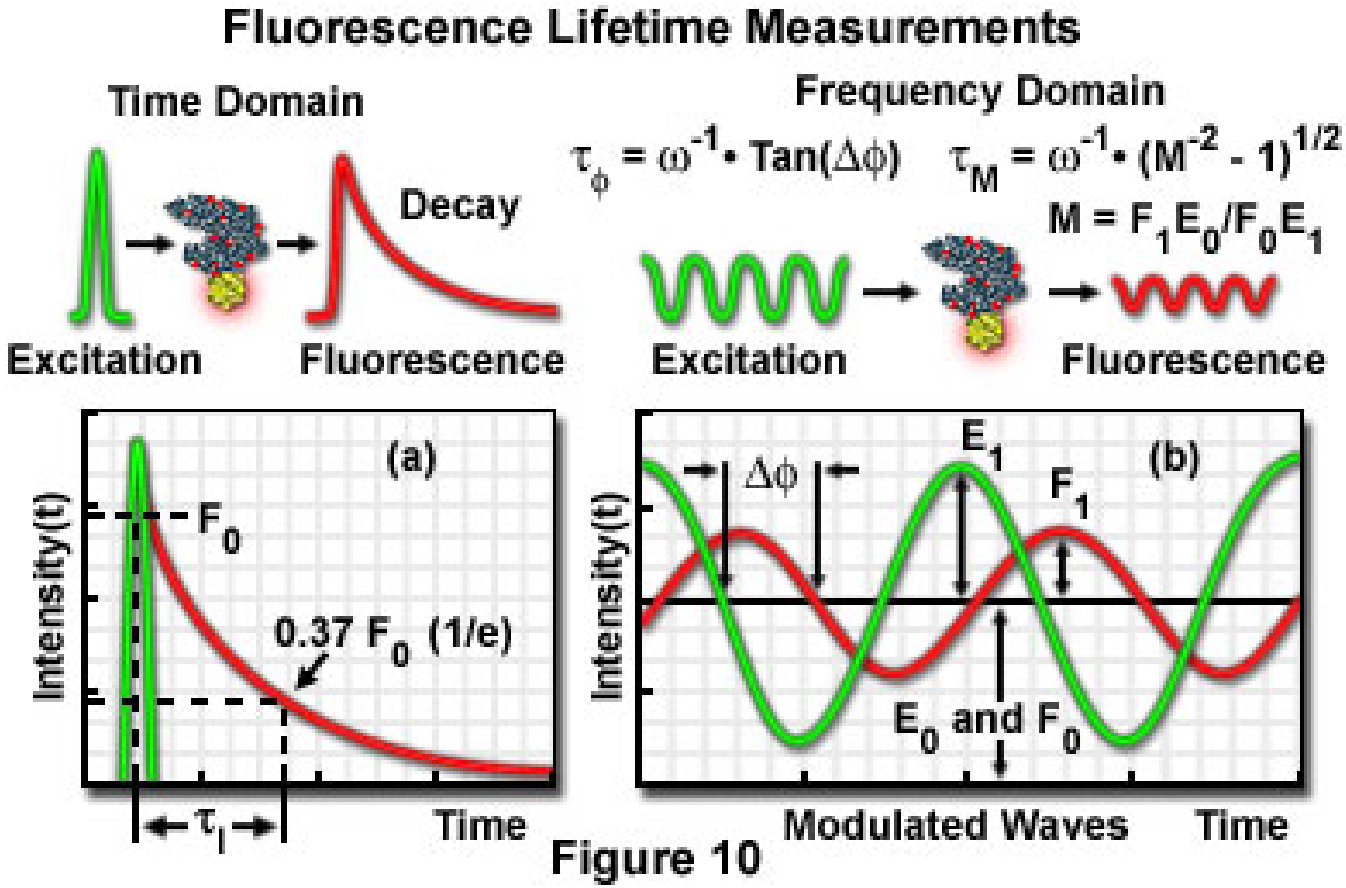

Figure 10

Applications

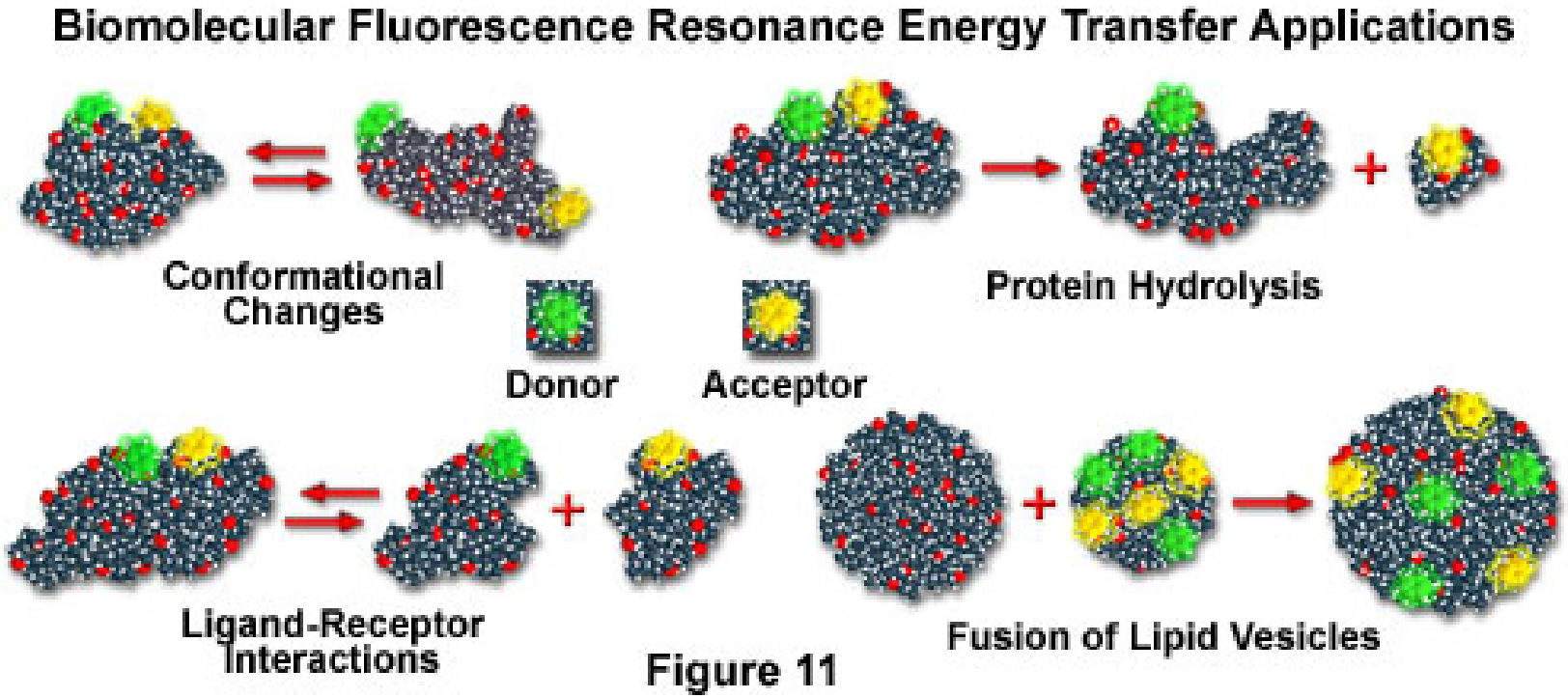

Figure 11

Diffraction Limit

$$d = \lambda/(2n \sin \alpha)$$

, $k_0 = 2NA/\lambda_{em}$

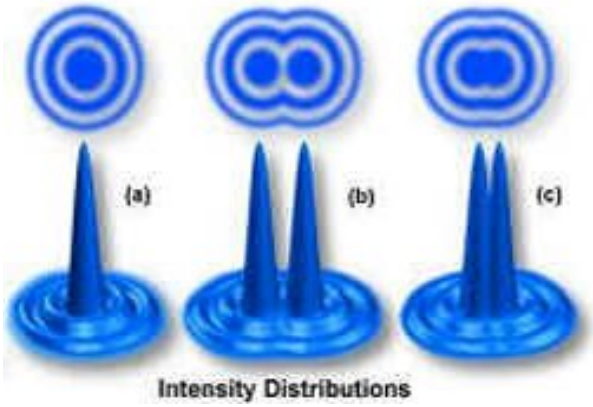

Localization

$$I(x, y) = I_{\text{background}} + A. \exp\left\{-1/2\left[\left(\frac{x - x_0}{s_x}\right)^2 + \left(\frac{y - y_0}{s_y}\right)^2\right]\right\},$$

$$\sigma^{\mu}_{x,y} = \sqrt{\frac{s^2_{x,y}}{N_{\text{photons}}} + \frac{a^2}{12.N_{\text{photons}}} + \frac{8.\pi.s^4_{x,y}.b^2}{a^2.N_{\text{photons}}}},$$

Fluorescence Imaging with One Nanometer Accuracy (FIONA)

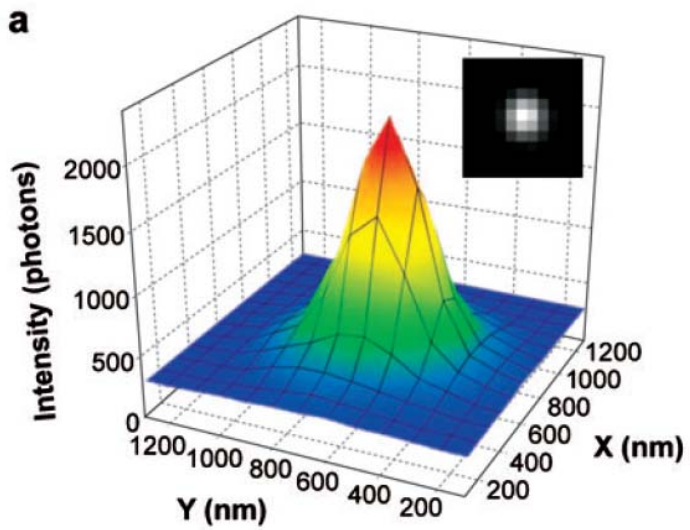

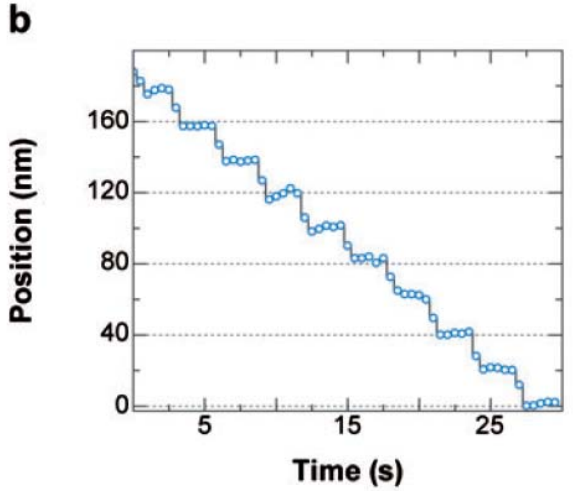

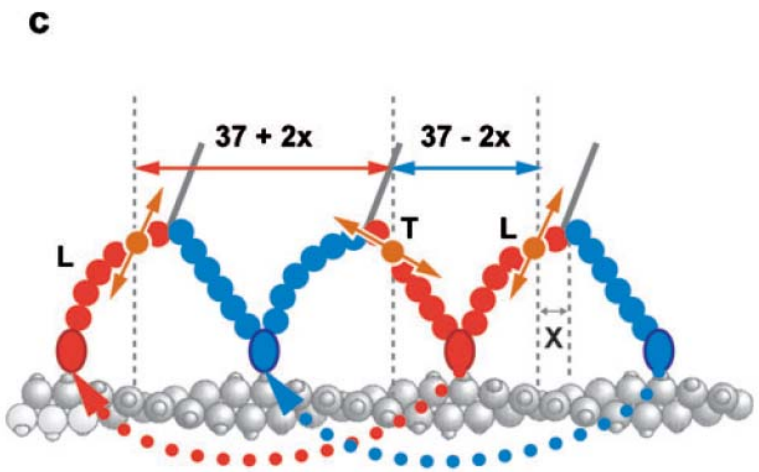

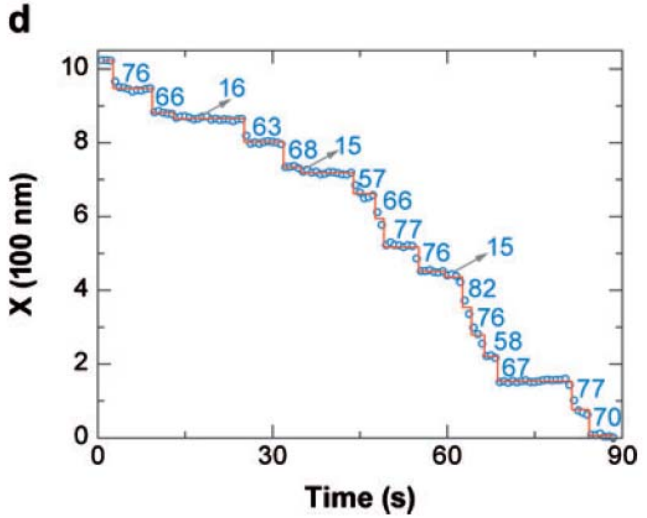

Fluorescence Imaging with One-Nanometer Accuracy (FIONA)

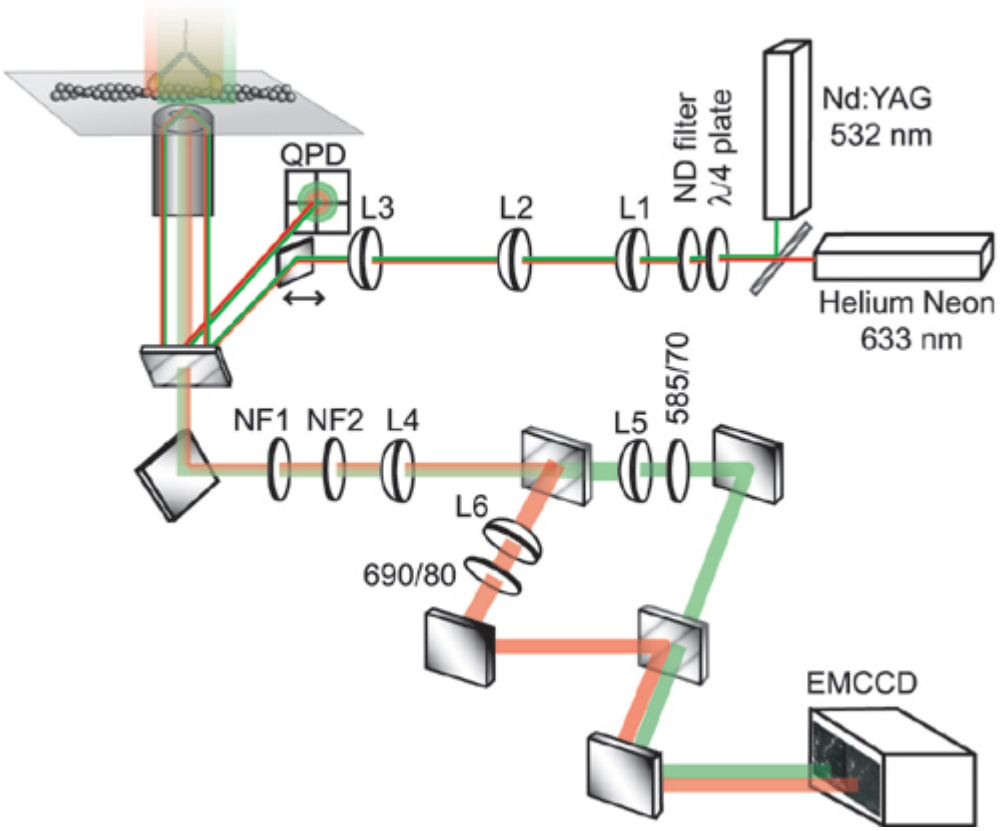

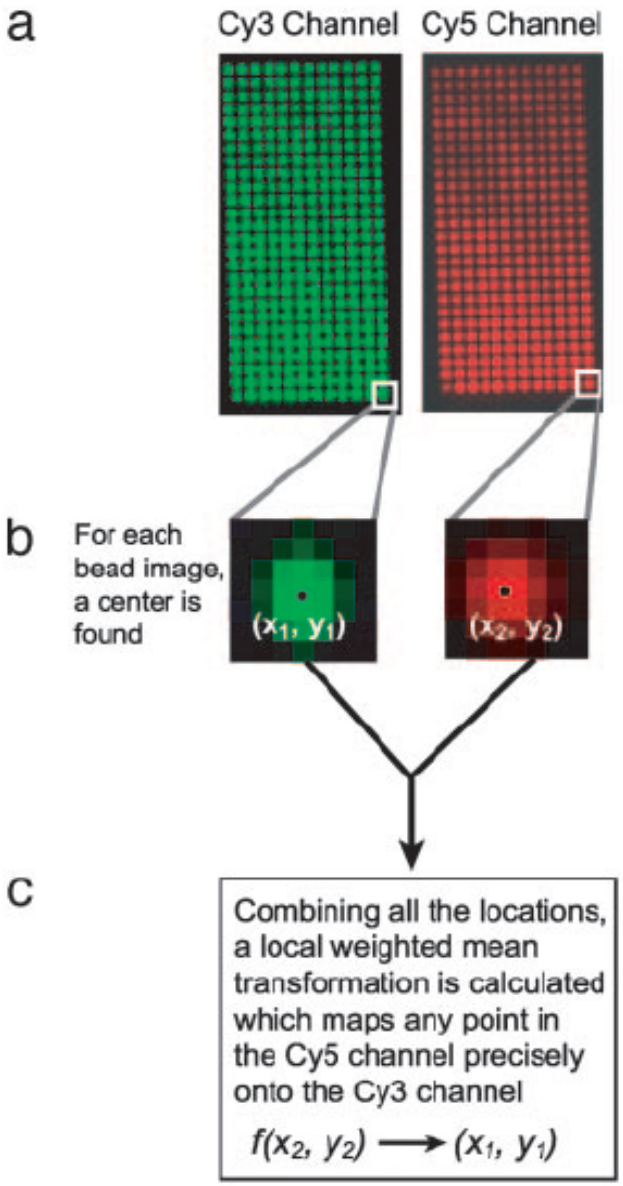

PNAS | February 1, 2005 | vol. 102 | no. 5 | 1419–1423

$$f(x, y) = z_0 + A \exp\left(\frac{1}{2}\left[\left(\frac{x - \mu_x}{\sigma_x}\right)^2 + \left(\frac{y - \mu_y}{\sigma_y}\right)^2\right]\right)$$

$$\sigma_\mu = \sqrt{(\sigma_x^2 + \sigma_y^2)} \Big/ \sqrt{N_\gamma - 1}.$$

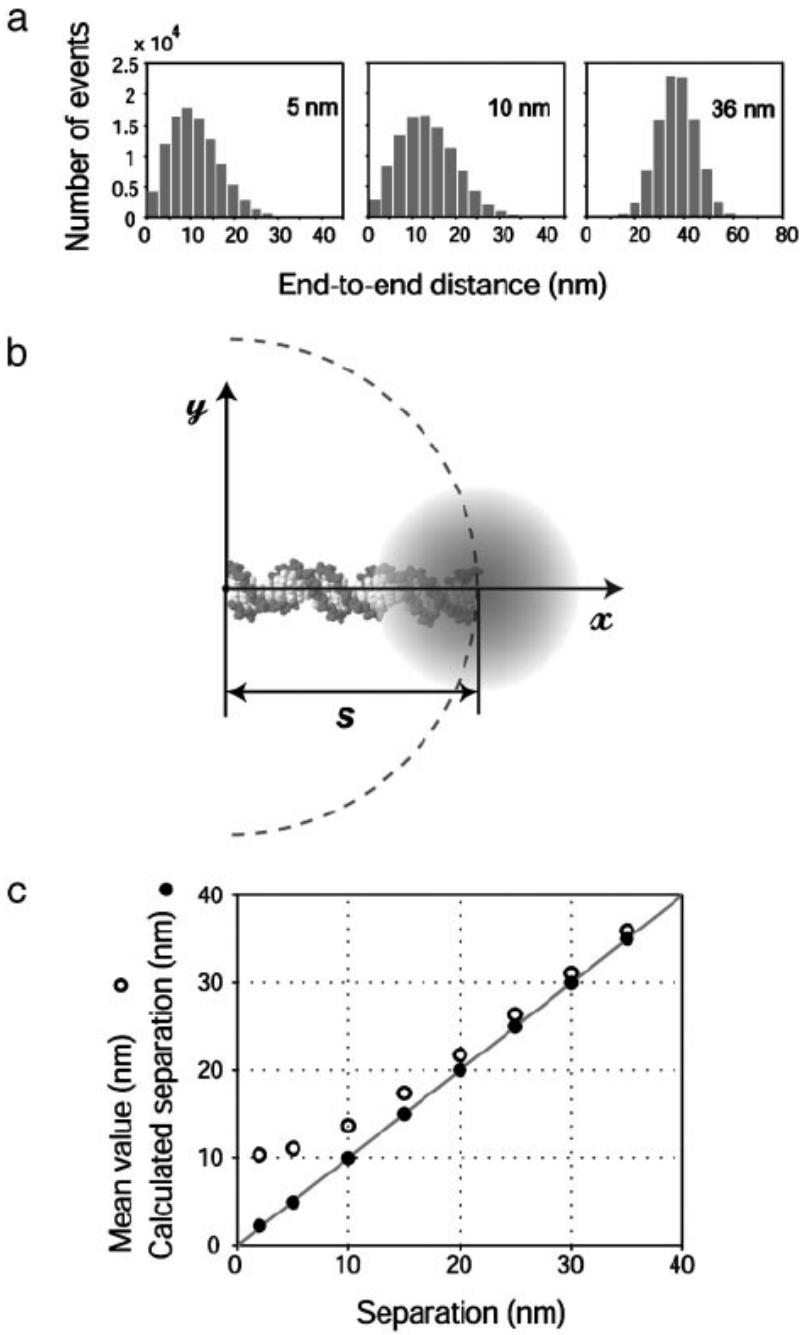

Fig. 2. Determining the accurate end-to-end distance from the skewed distribution of distance measurements. (*a*) The distance probability distribution was calculated by means of Monte Carlo simulations. (*b*) The skew in the histograms toward large values can be understood from a geometric argument. If one end of the DNA molecule is measured to reside at the origin, then only points lying on the circumference of a circle with radius *s* and origin (0, 0) will yield the true end-to-end distance. It is more likely that a point will lie outside of the dashed-line semicircle than inside it, which gives the distance distribution a long tail. (*c*) Despite the non-Gaussian nature of the distance distribution, the end-to-end separation can be calculated using the geometric mean, variance, and localization errors.

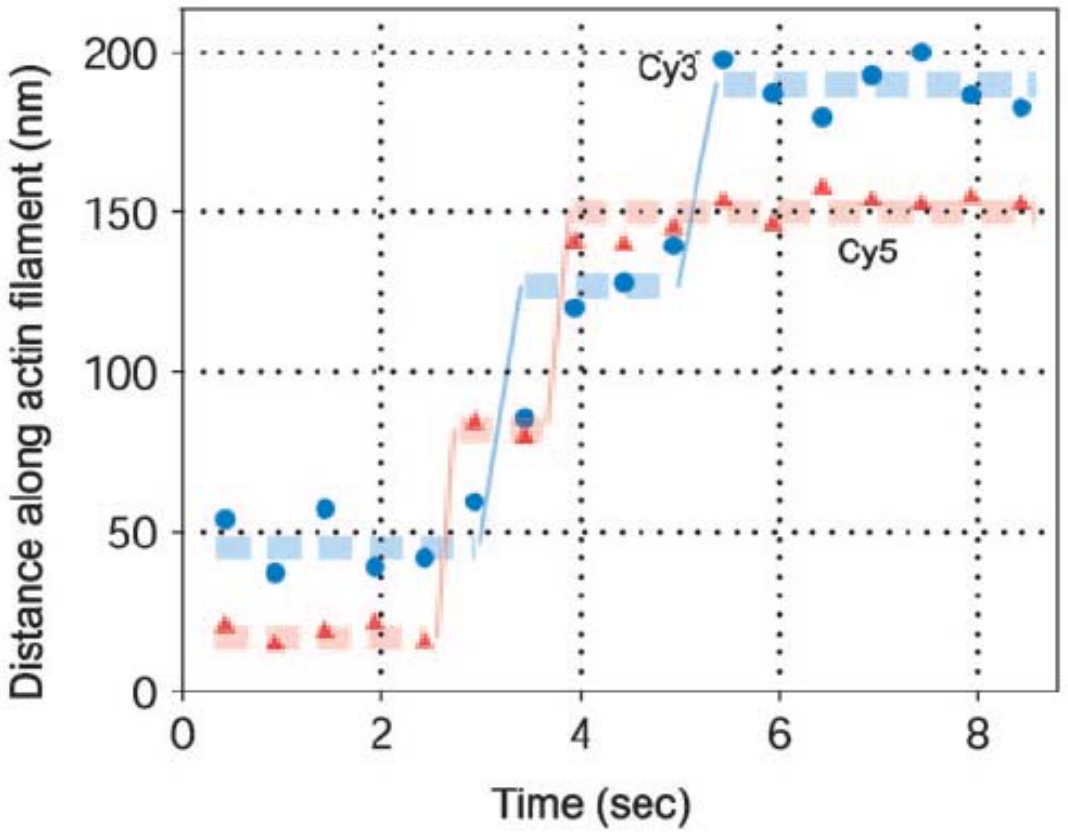

Fig. 4. Time trace of a differentially labeled myosin V molecule walking along an actin filament. The labels (Cy3 and Cy5) are covalently attached to calmodulins that were exchanged onto the myosin V molecule. In this trace, both of the fluorescent probe's locations are taking 72-nm steps, indicating that the calmodulins were exchanged close to the motor domain. The alternating positions of the probes provide a direct observation of myosin V's hand-over-hand walking mechanism.

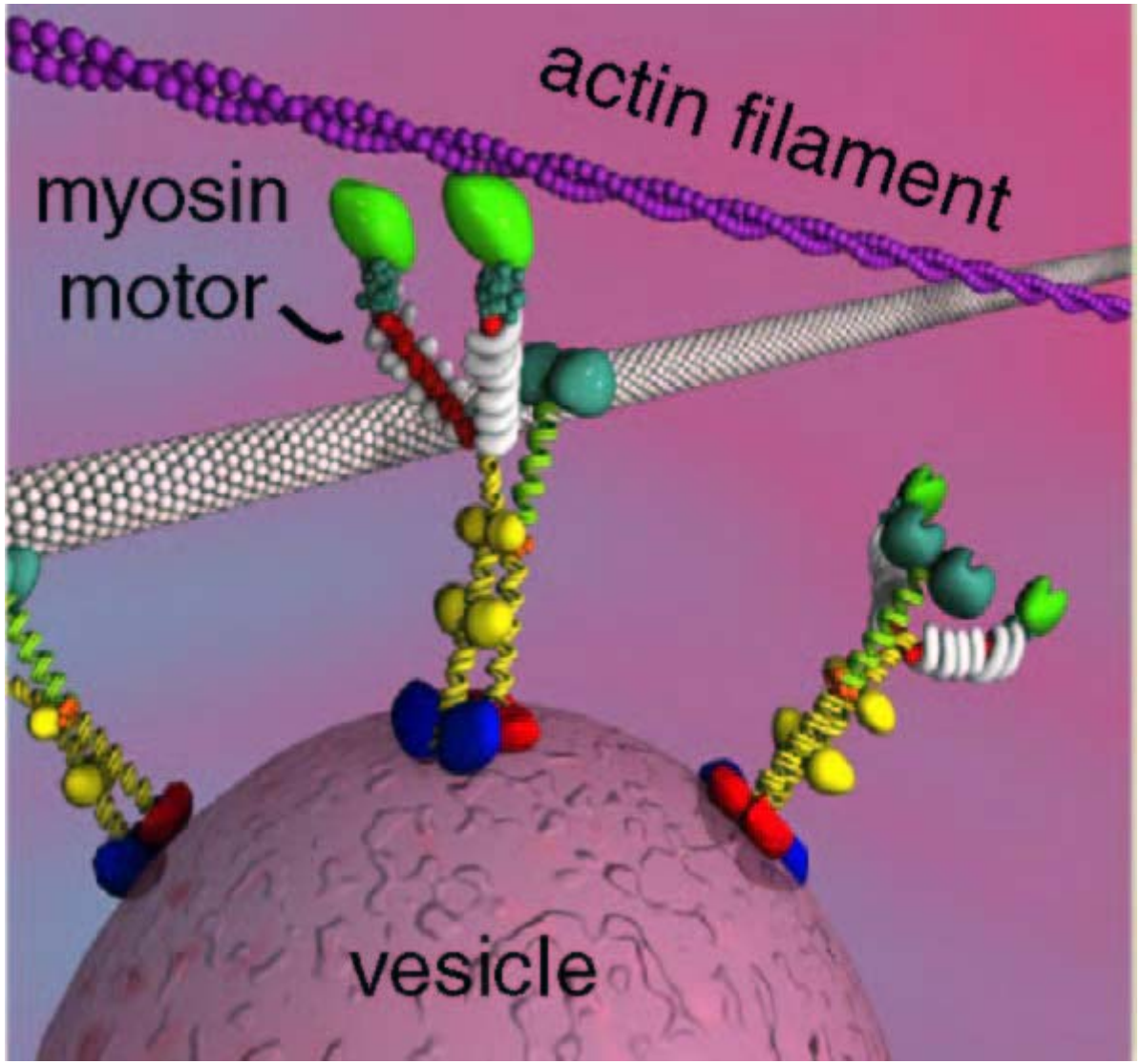
actin filament
myosin
motor
vesicle

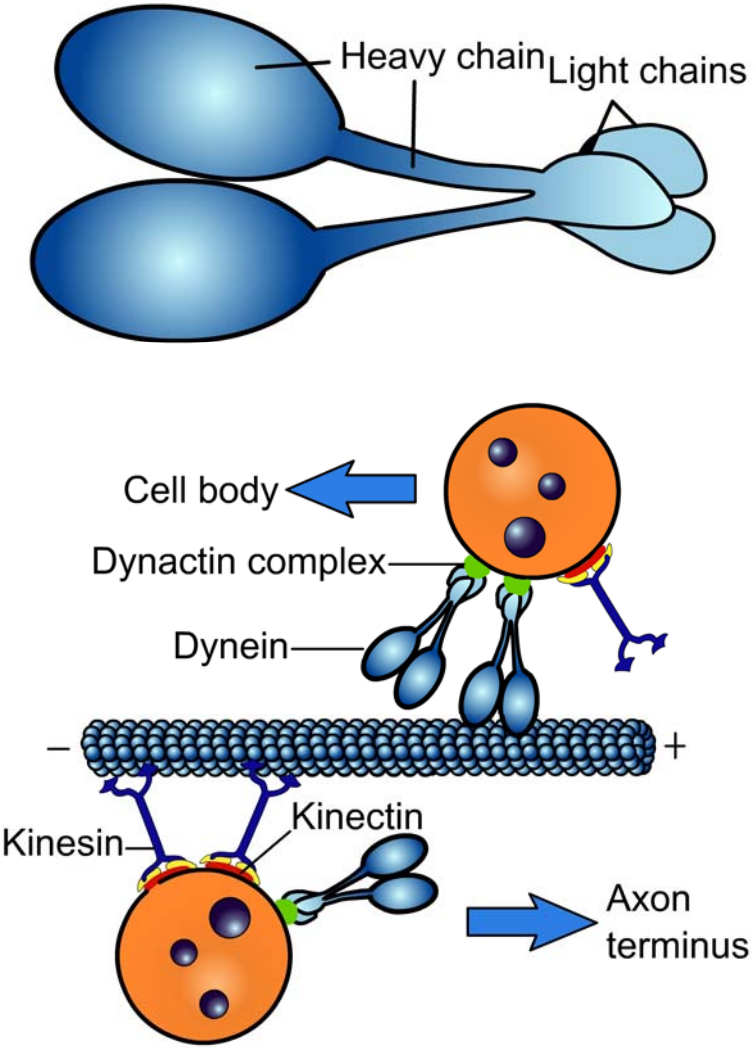
Heavy chain
Light chains
Cell body
Dynactin complex
Dynein
–
+
Kinesin
Kinectin
Axon
terminus

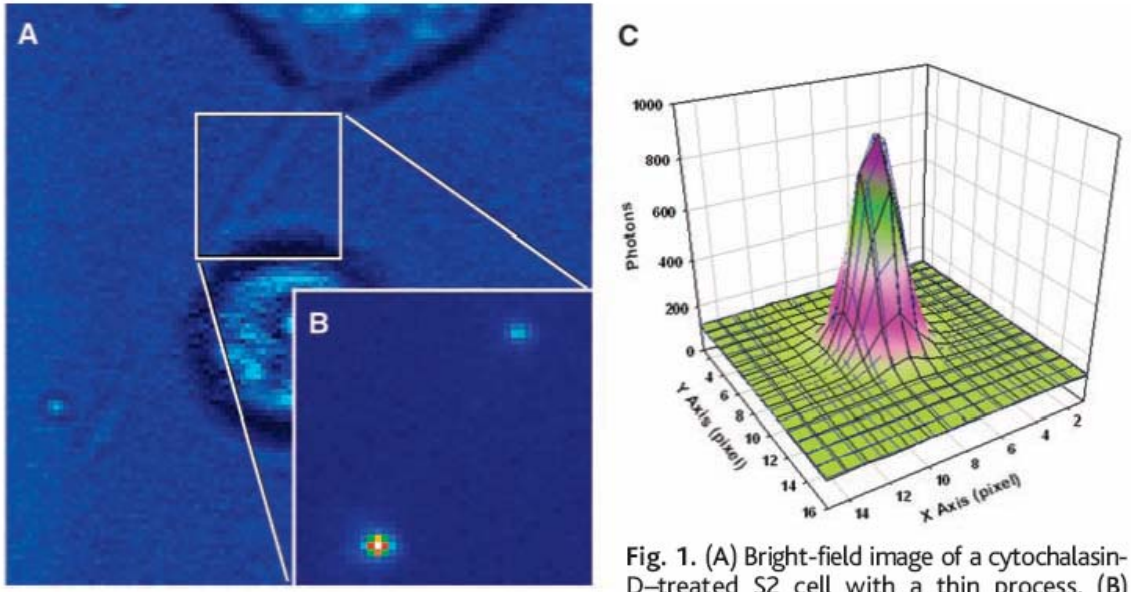

Fig. 1. (A) Bright-field image of a cytochalasin-D–treated S2 cell with a thin process. (B) Fluorescence image of the GFP-labeled peroxisomes within the process. (C) Fluorescence image of a peroxisome can be fit to a two-dimensional Gaussian (correlation coefficient $r^2 = 0.992$), enabling the center to be determined to 1.5 nm within 1.1 ms.

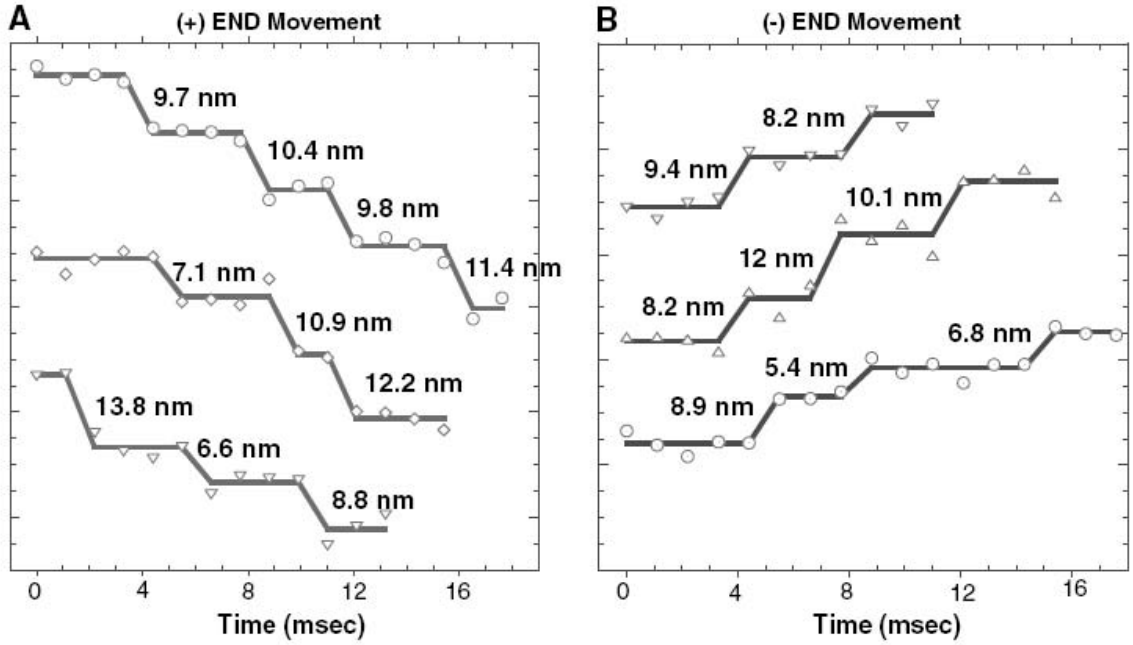

Kinesin and Dynein Move a Peroxisome in Vivo: A Tug-of-War or Coordinated Movement?

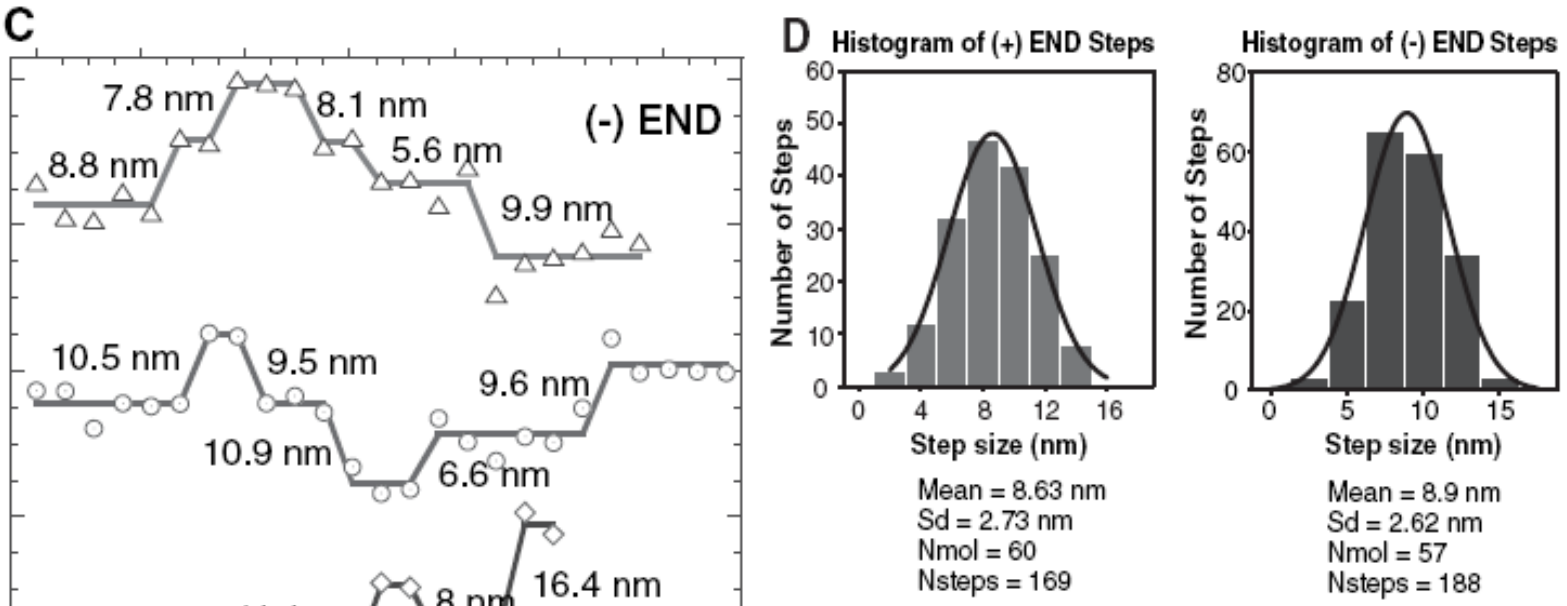

Fig. 2. Step-by-step movement of peroxisomes carried by (A) a single kinesin, (B) a single dynein, and (C) a coordination of kinesin and dynein. (D) Histograms of the individual steps of anterograde (kinesin) and retrograde (dynein) movement. A pairwise displacement of kinesin and dynein, showing the multiples of 8-nm displacement, is shown in fig. S6.

Single-molecule High-Resolution Colocalization (SHREC)

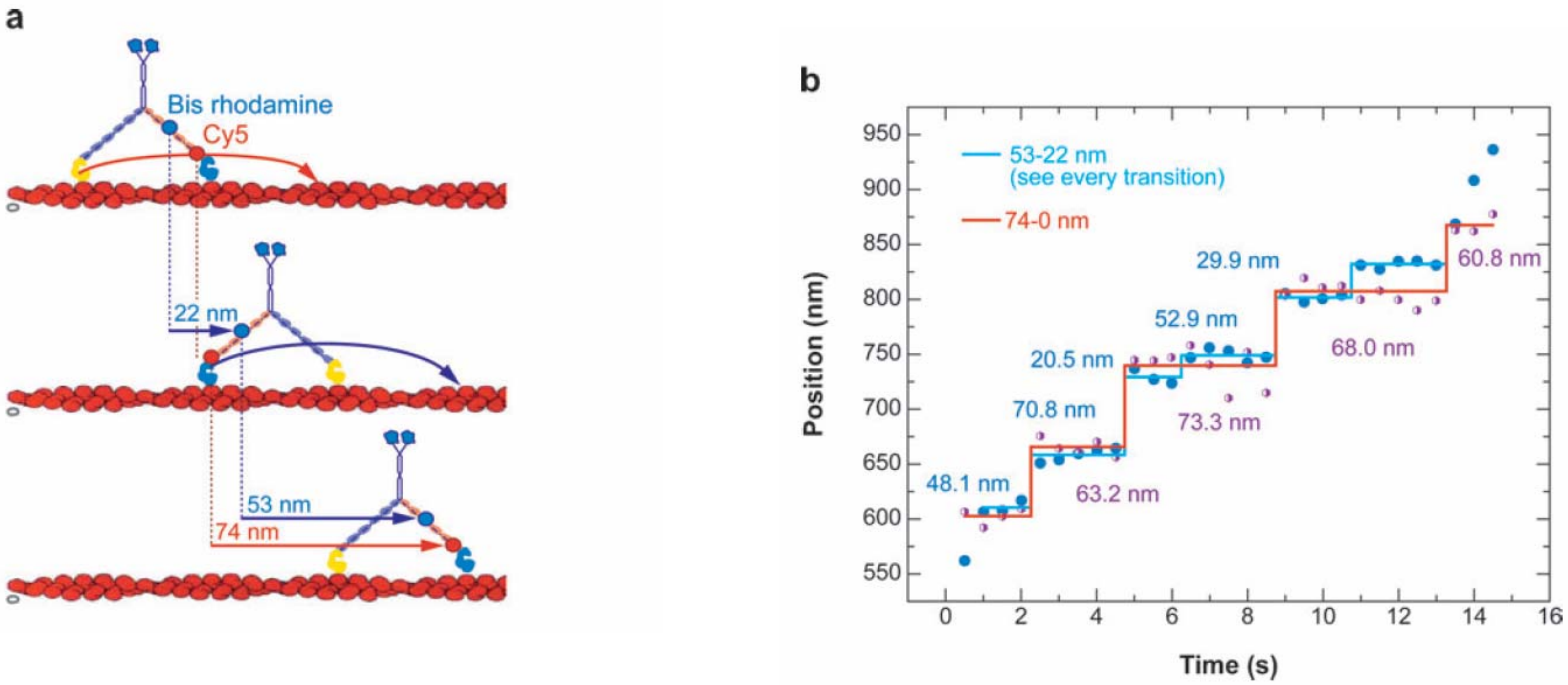

Photo-bleaching

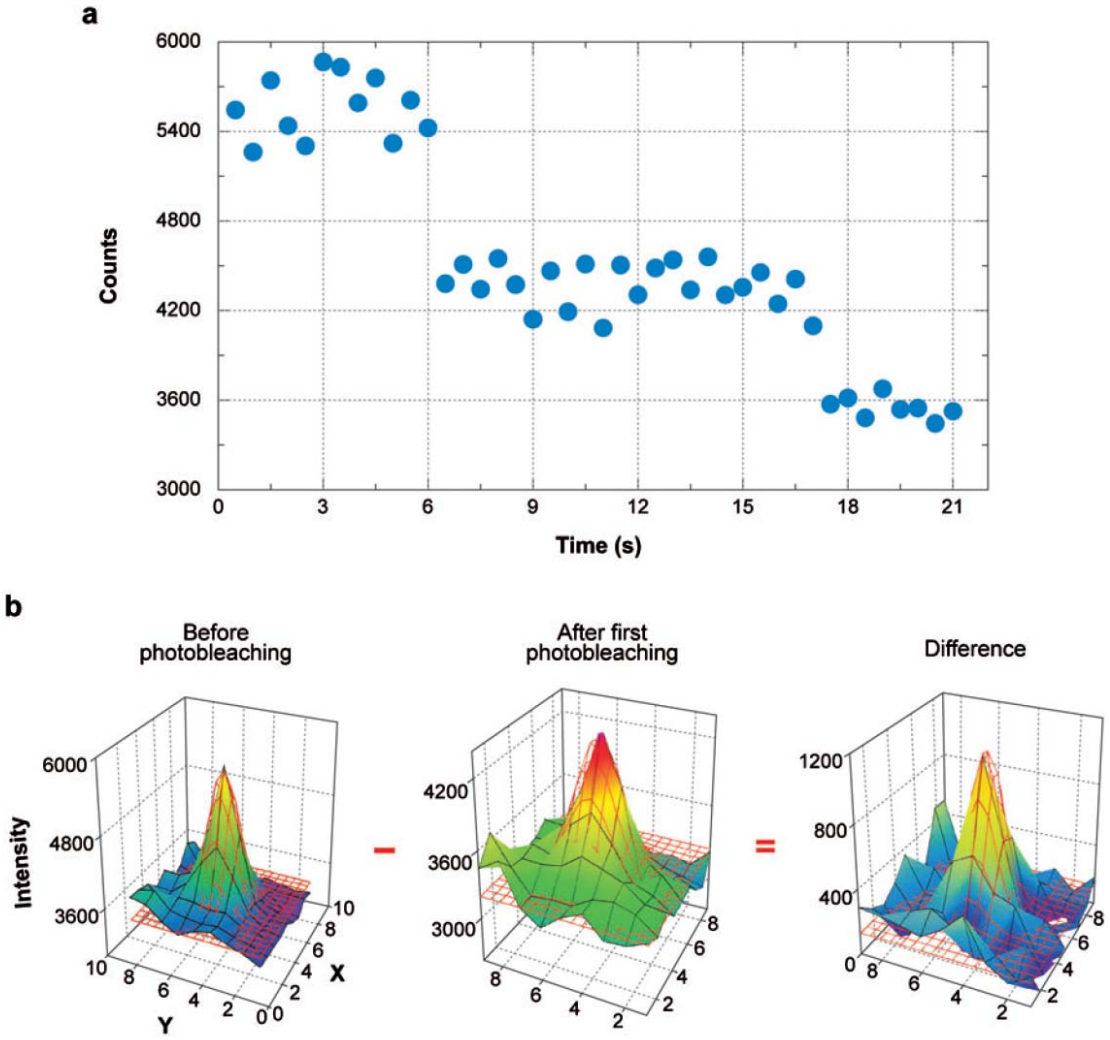

Super-Resolution Micorscopy

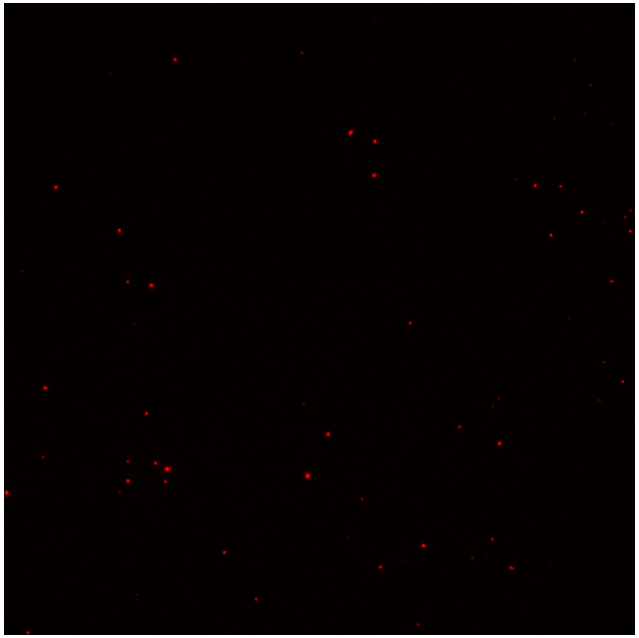

Blinking event of two Qdots

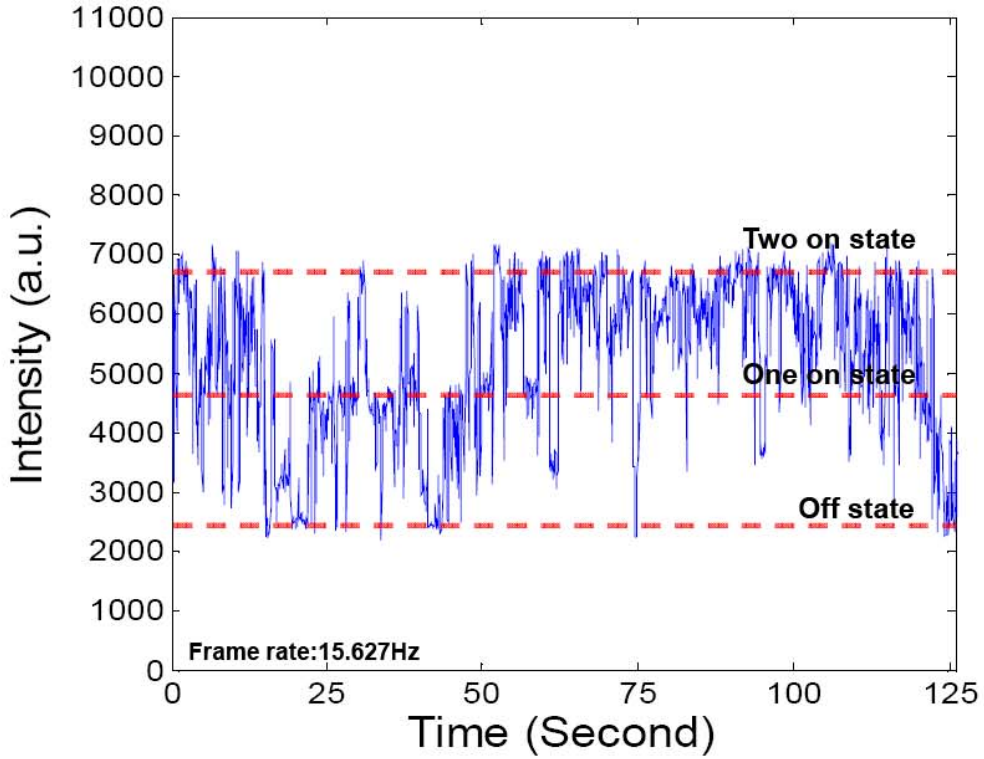

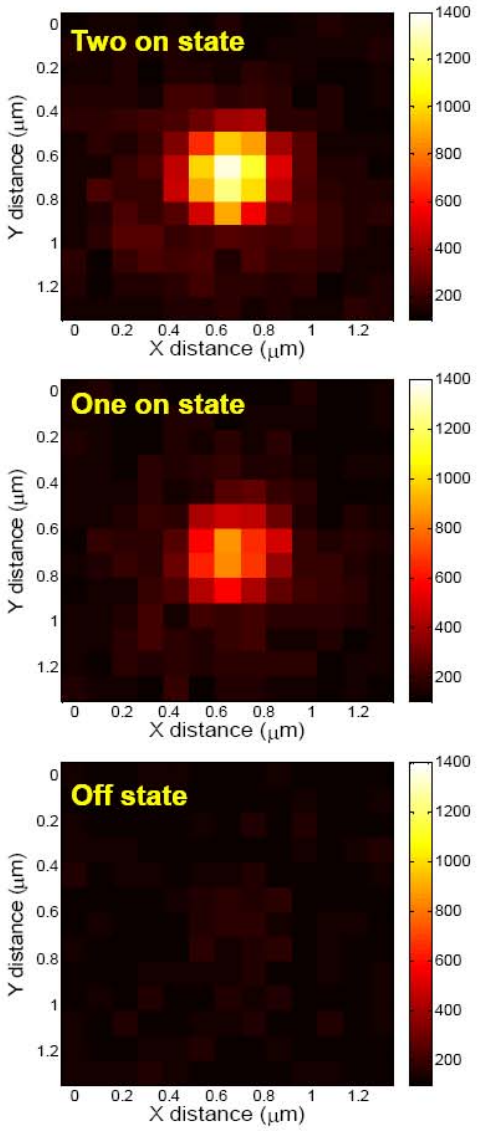

Single QDot

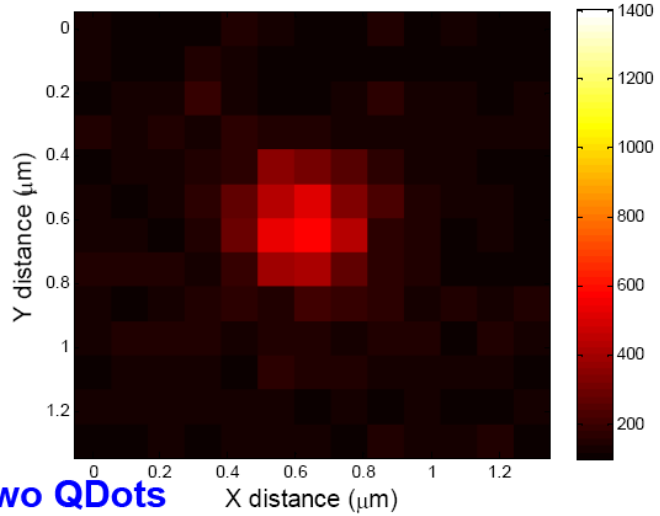

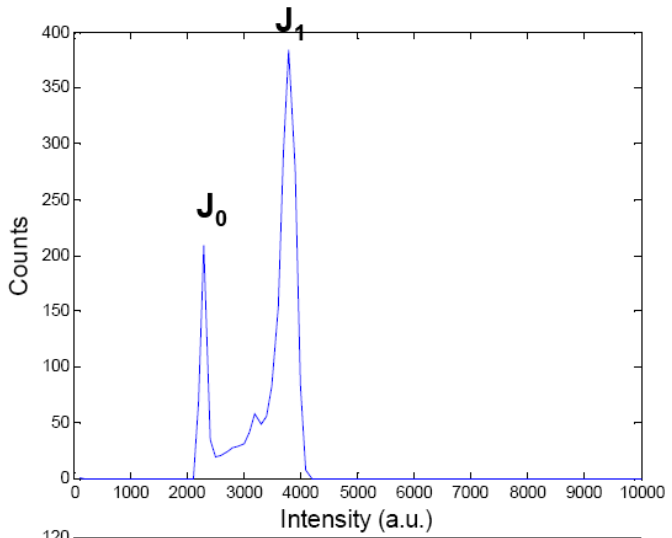

Two QDots

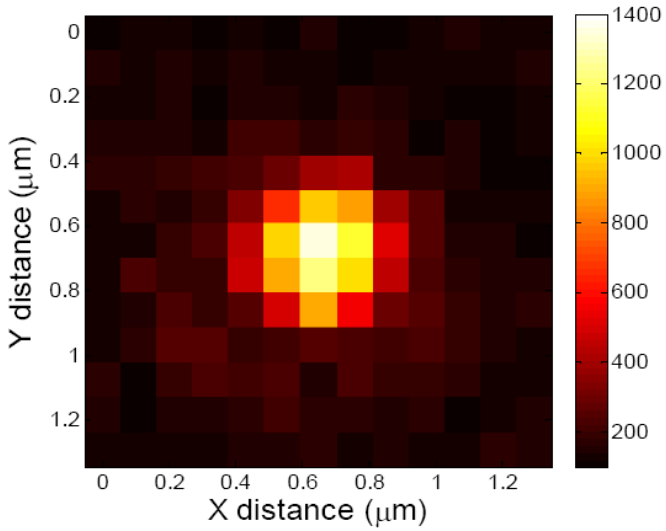

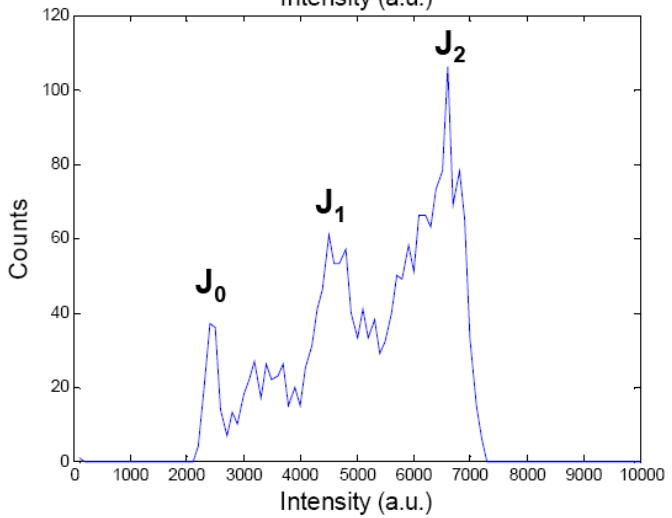

Single QDot case

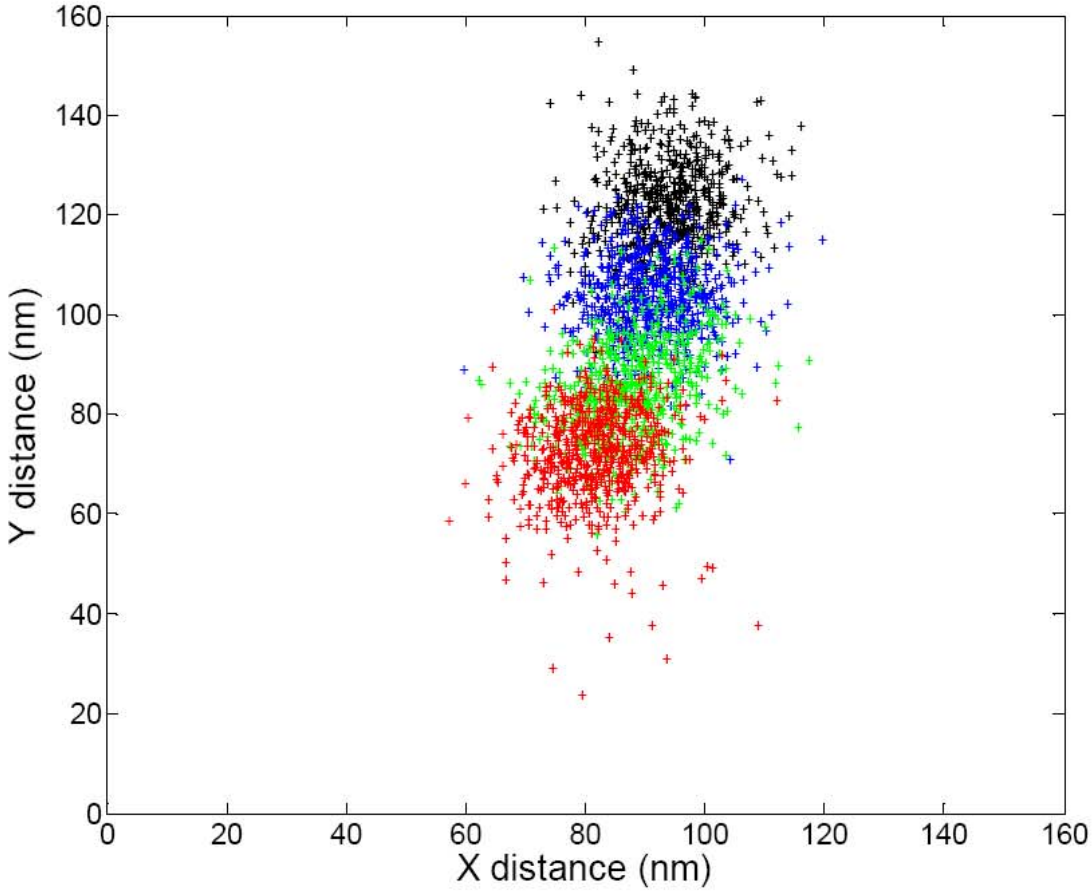

Black spot (1-636)

Standard deviation
=(σx+ σy)/2
=(6.99+9.35)/2=8.17 nm

Blue spot (637-1272)

Standard deviation
=(σx+ σy)/2
=(7.42+7.99)/2=7.70 nm

Green spot (1273-1908)

Standard deviation
=(σx+ σy)/2
=(7.86+9.66)/2=8.76 nm

Red spot (1909-2547)

Standard deviation
=(σx+ σy)/2
=(7.35+9.41)/2=8.38 nm

All spot (1-2547)

Standard deviation
=(σx+ σy)/2
=(8.70+20.80)/2=14.75 nm

Nanometer Distance Measurements between Multicolor Quantum Dots

Received April 10, 2009

Josh Antelman, Connie Wilking-Chang, Shimon Weiss, and Xavier Michalet*

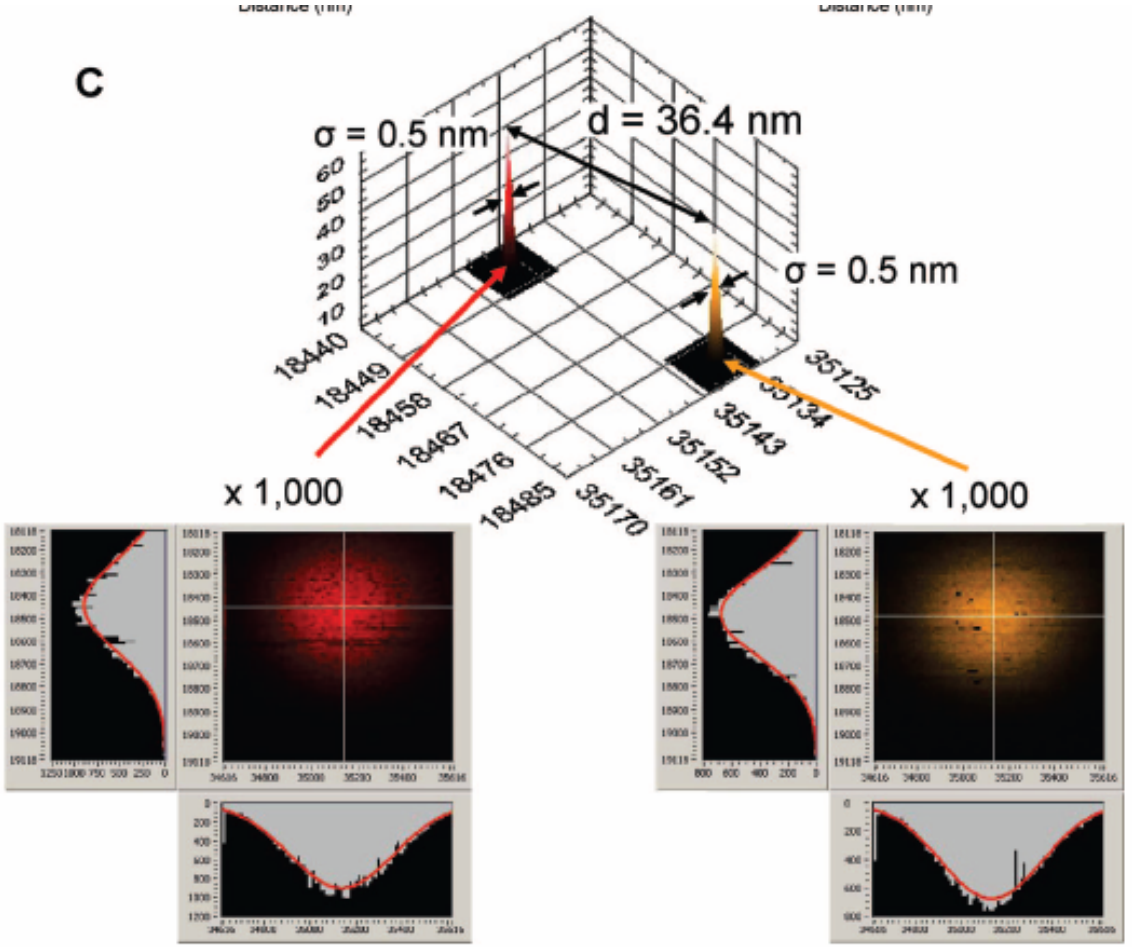

Super-Resolution Microscopy

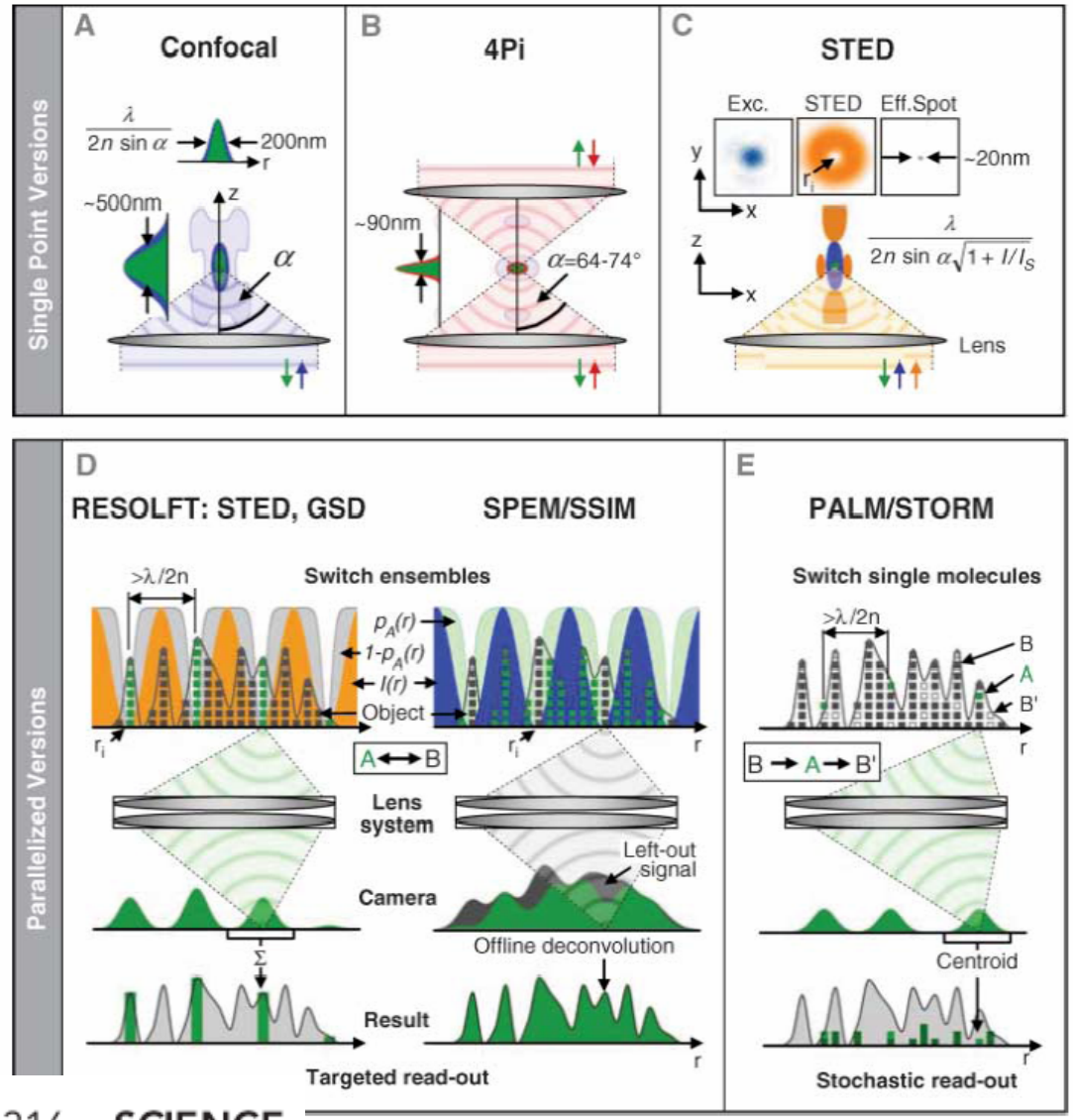

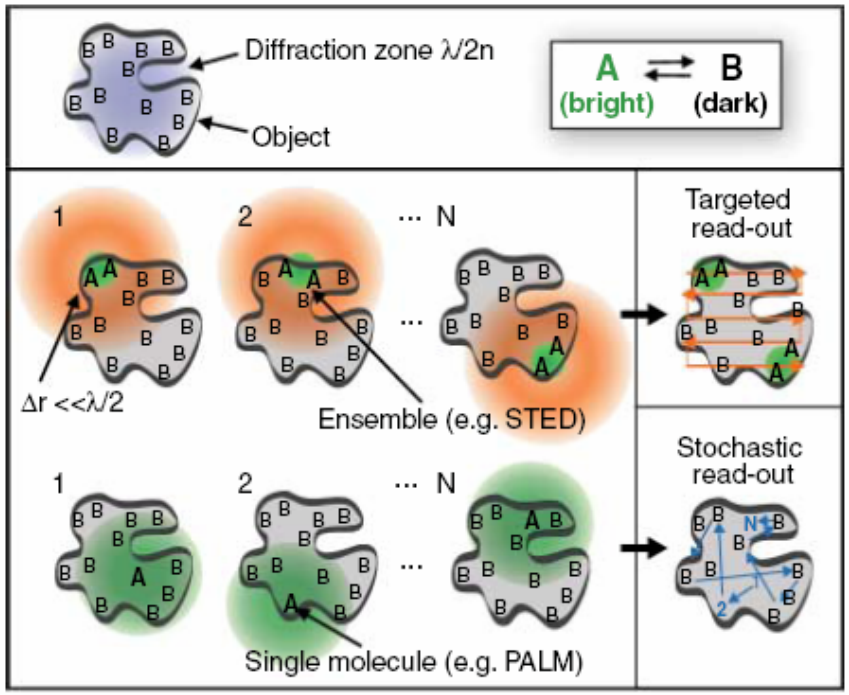

Fig. 2. Targeted versus stochastic time-sequential readout of fluorophore markers of a nanostructured object within the diffraction zone whose lower bound is given by $\lambda/2n$. A and B denote a bright and a dark state, respectively. In the targeted readout mode, one of the two states (here A) is established at a subdiffraction-sized spot at the position of a zero to read out an unknown number of fluorophore molecules. The image is assembled by deliberate translation of the zero. The zero can also be a groove. In the stochastic readout mode, a single switchable fluorophore from a random position within the diffraction zone is switched to a stable state A, while the other molecules remain in B. The coordinate is calculated from the centroid of the diffraction fluorescence spot measured by a pixelated detector. The coordinate pops up stochastically depending on where the interrogated marker molecule is located.

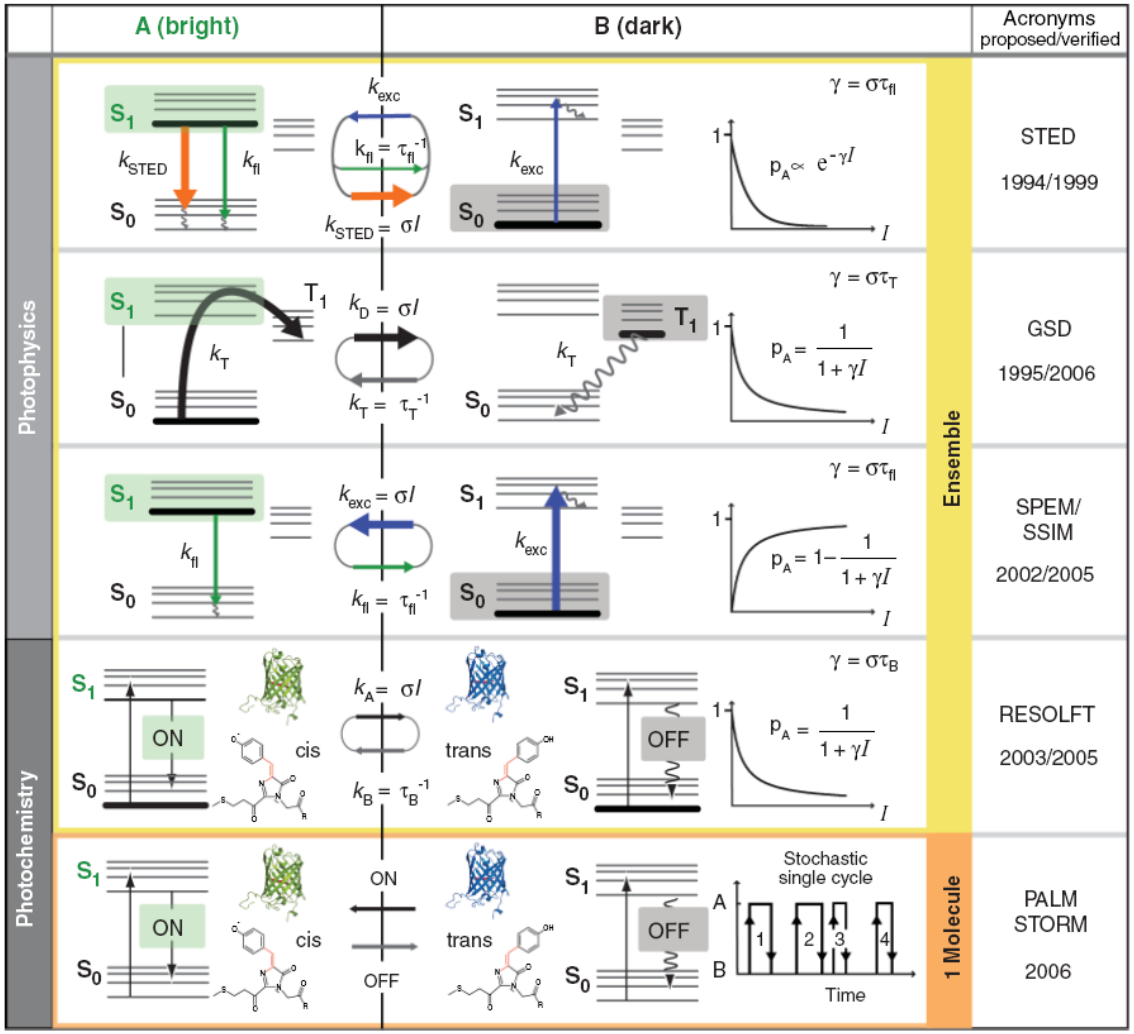

Fig. 3. Bright (**A**) and dark (**B**) molecular states used to break the diffraction barrier. Whereas STED, GSD, and SPEM utilize photophysical transitions, the photoswitching version of the RESOLFT scheme, as well as PALM and STORM, exploit photochemical transitions in which atoms are relocated or bonds formed and broken. PALM and STORM rely on measuring single (or at least identifiable) molecules at a time, whereas the other concepts, although compatible with single-molecule imaging, principally read out ensembles. Ensemble techniques rely on reversible transitions between A and B, as indicated by the rates k. The probability p_A of being in state A depends nonlinearly on the light intensity applied, as indicated by the equations, ensuring that either A or B is confined to a subdiffraction area at a targeted coordinate in space. The $e^{-\gamma I}$ and the $(1 + \gamma I)^{-1}$ dependence entail nonlinearities of infinite order $(\gamma I)^m$; $m \to \infty$. By increasing the lifetime of the chosen states, γ strengthens the nonlinear dependence of p_A, thus enabling huge nonlinearities at low I. This is radically different from m-photon processes that, depending on the concomitant action of m photons and hence just on I^m, are firmly limited to order m (*15*), which in practice is only $m < 4$. Because it operates with single molecules in a known state, the probability concept breaks down in PALM and STORM, but reminiscent of nonlinearity is the optical switching.

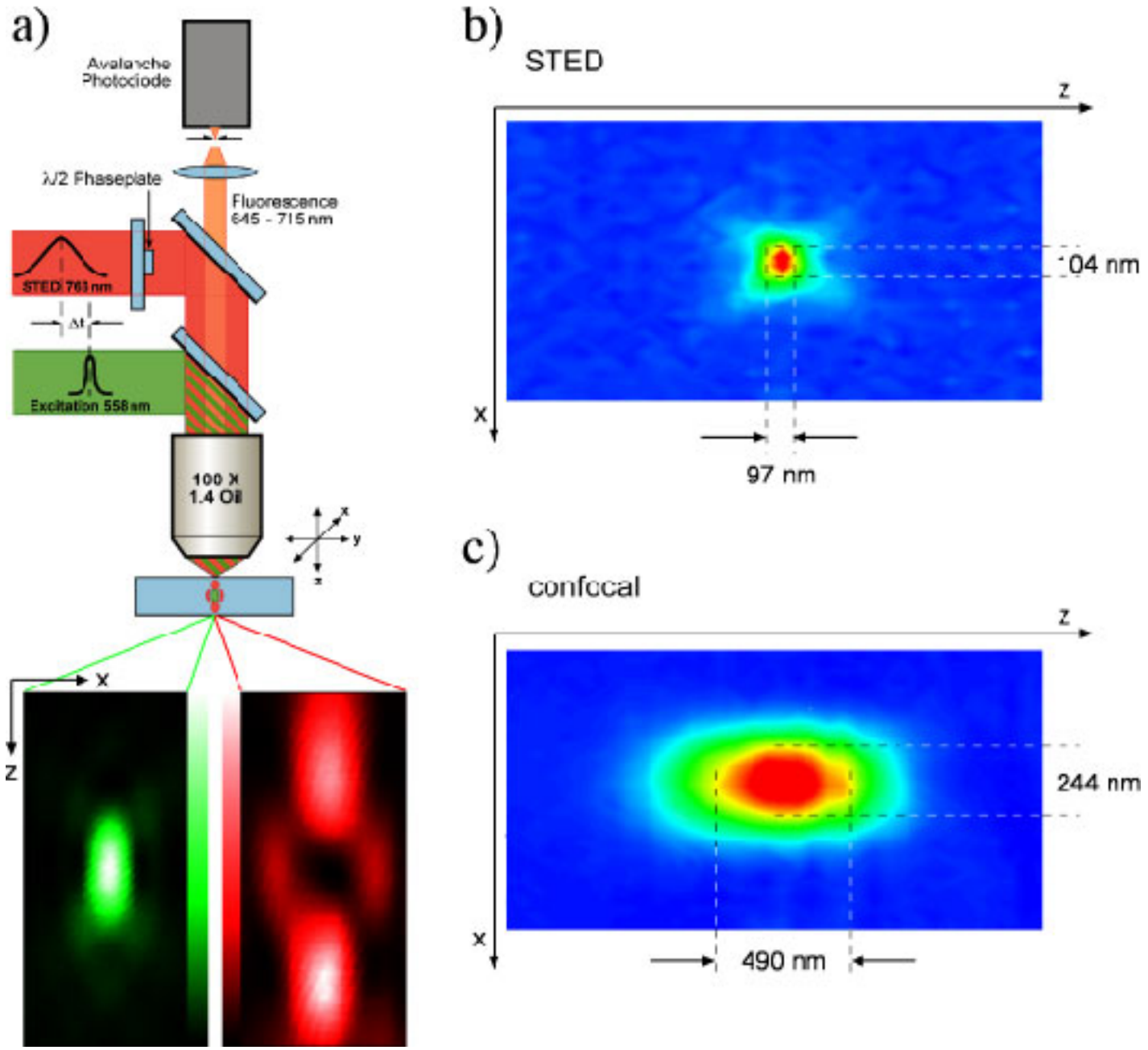
a)
Avalanche Photodiode
λ/2 Phaseplate
Fluorescence 645 - 715 nm
STED 761 nm
Δt
Excitation 558 nm
100 x 1.4 Oil
x
y
z
x
z
b)
STED
z
x
97 nm
c)
confocal
z
x
490 nm
244 nm

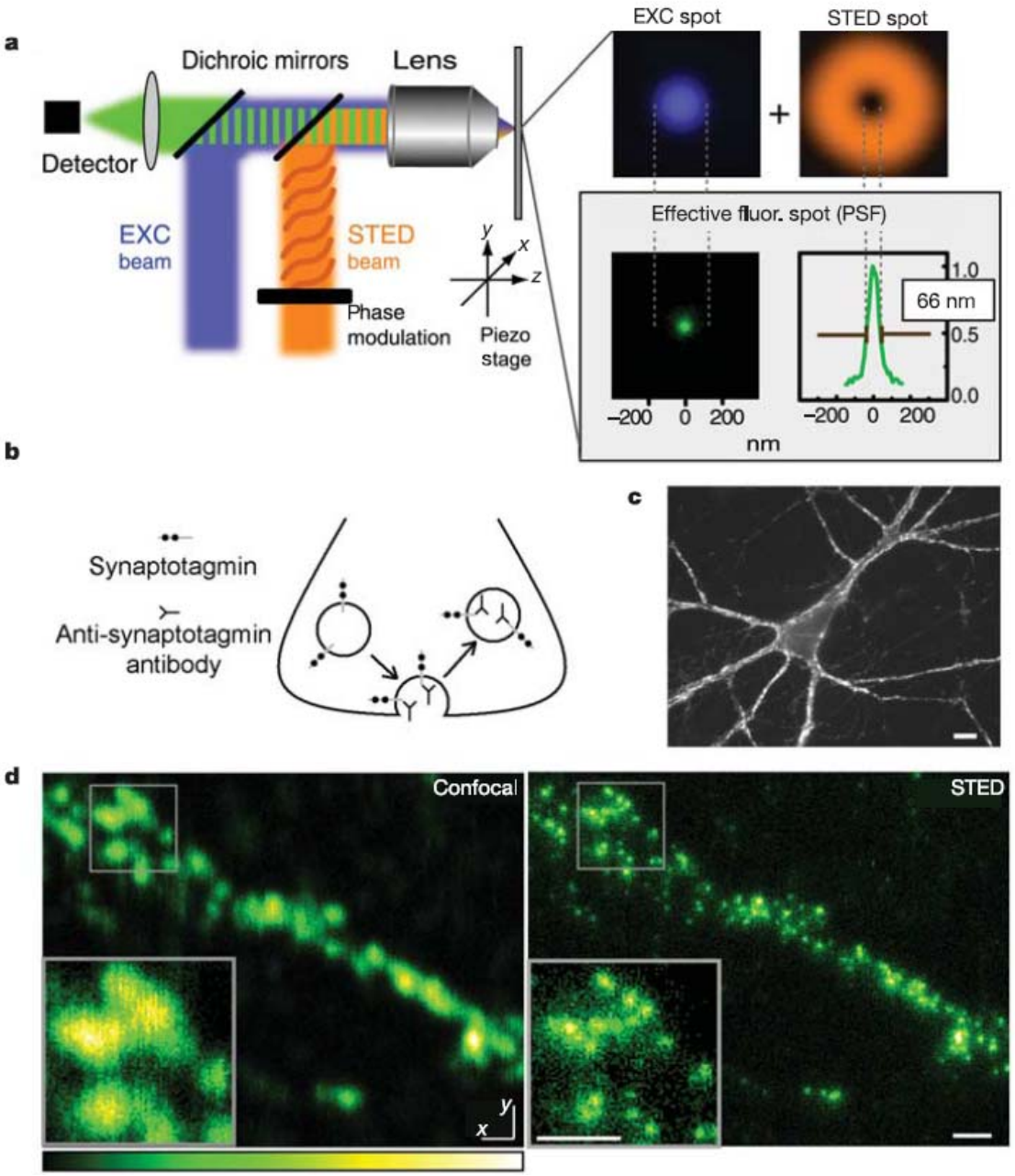
a
Dichroic mirrors
Lens
Detector
EXC
beam
STED
beam
Phase
modulation
Piezo
stage
y
x
z
EXC spot
STED spot
+
Effective fluor. spot (PSF)
1.0
66 nm
0.5
0.0
–200 0 200
–200 0 200
nm
b
Synaptotagmin
Anti-synaptotagmin
antibody
c
d
Confocal
STED
y
x

STED microscopy with continuous wave beams

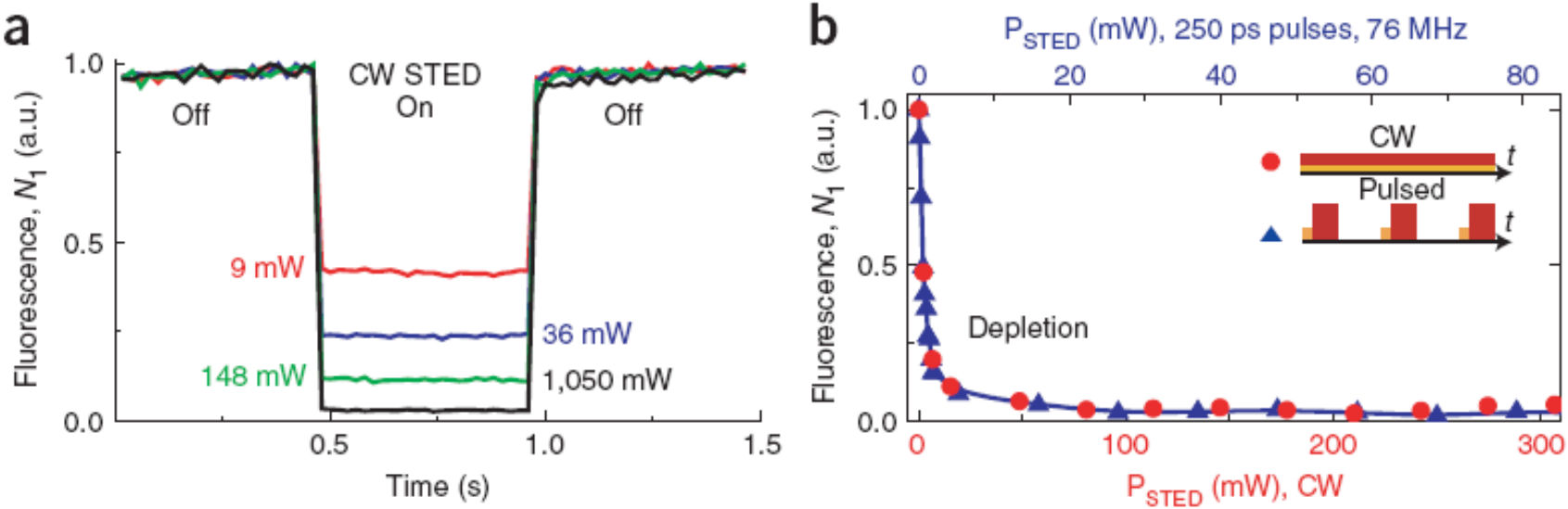

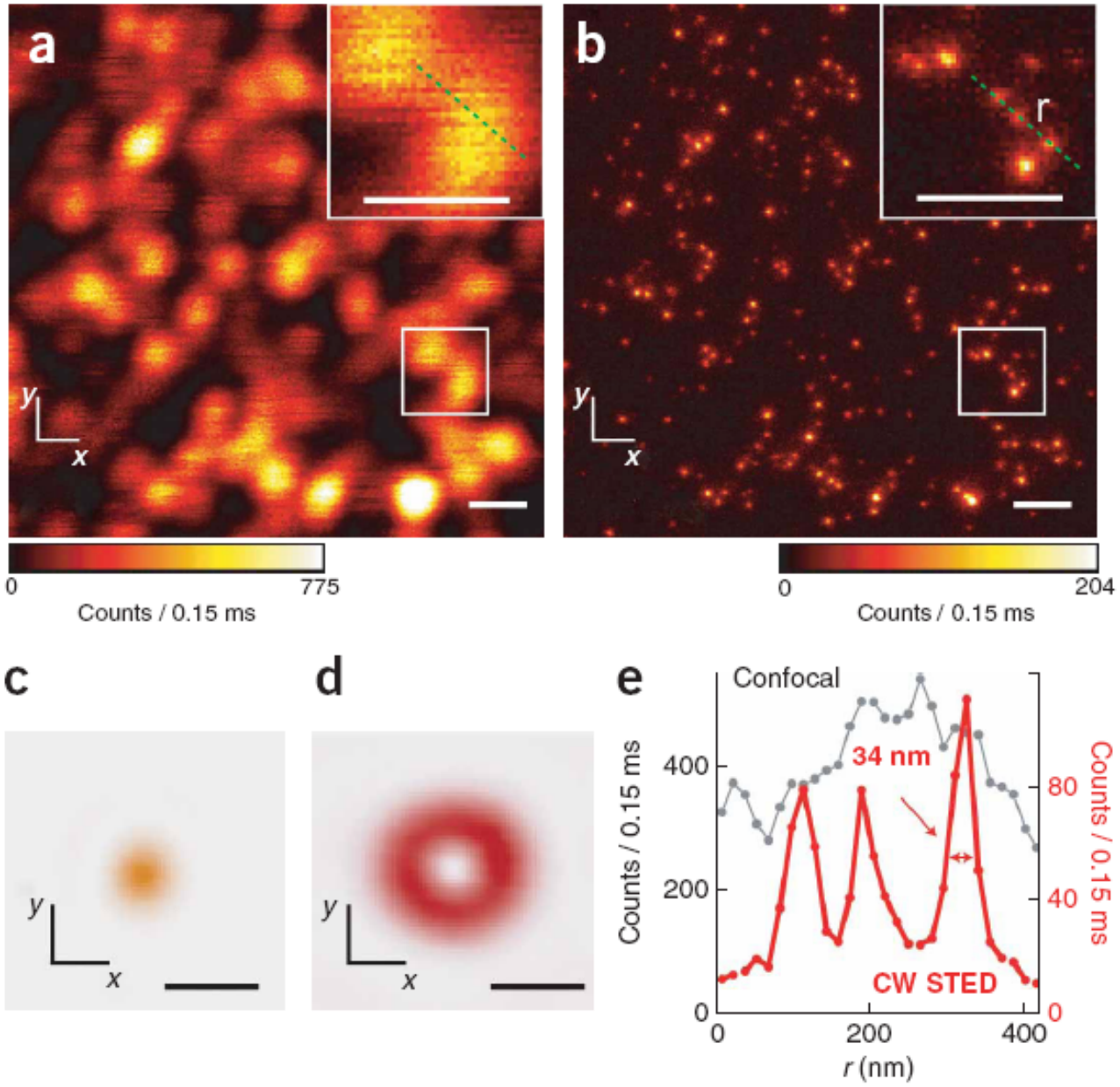
a
b
r
y
x
0
775
Counts / 0.15 ms
0
204
Counts / 0.15 ms
c
d
e
Confocal
34 nm
CW STED
Counts / 0.15 ms
Counts / 0.15 ms
400
200
0
80
40
0
0
200
400
r (nm)

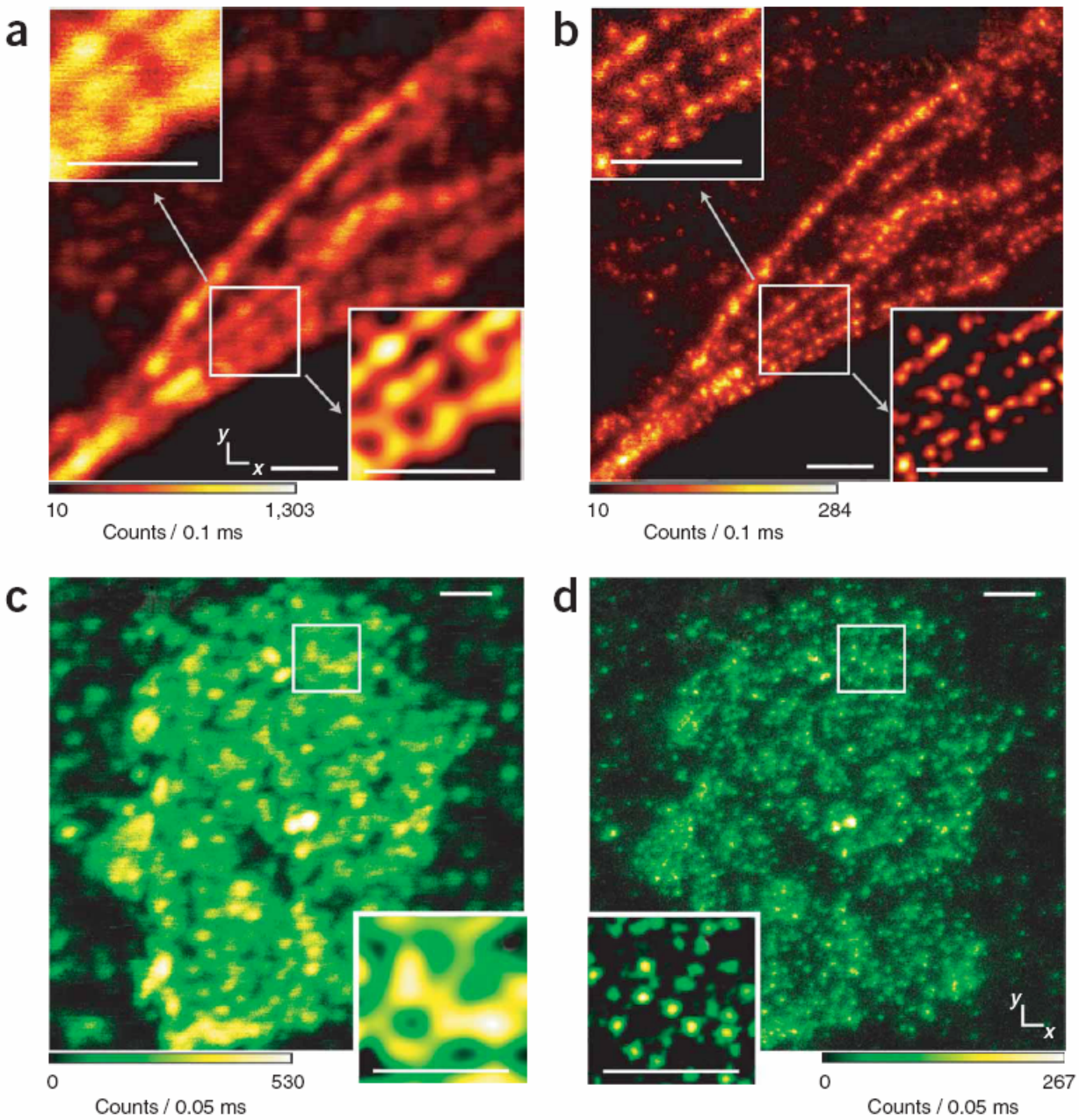
a
y
x
10
1,303
Counts / 0.1 ms
b
10
284
Counts / 0.1 ms
c
0
530
Counts / 0.05 ms
d
y
x
0
267
Counts / 0.05 ms

Video-Rate Far-Field Optical Nanoscopy Dissects Synaptic Vesicle Movement

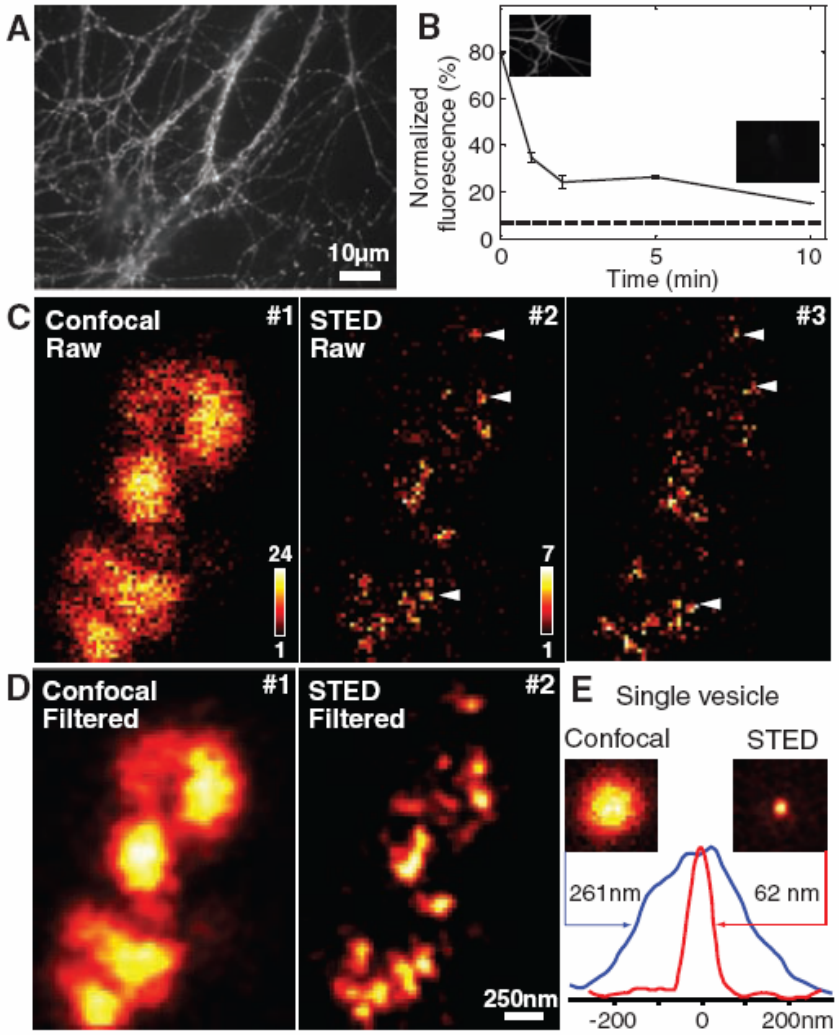

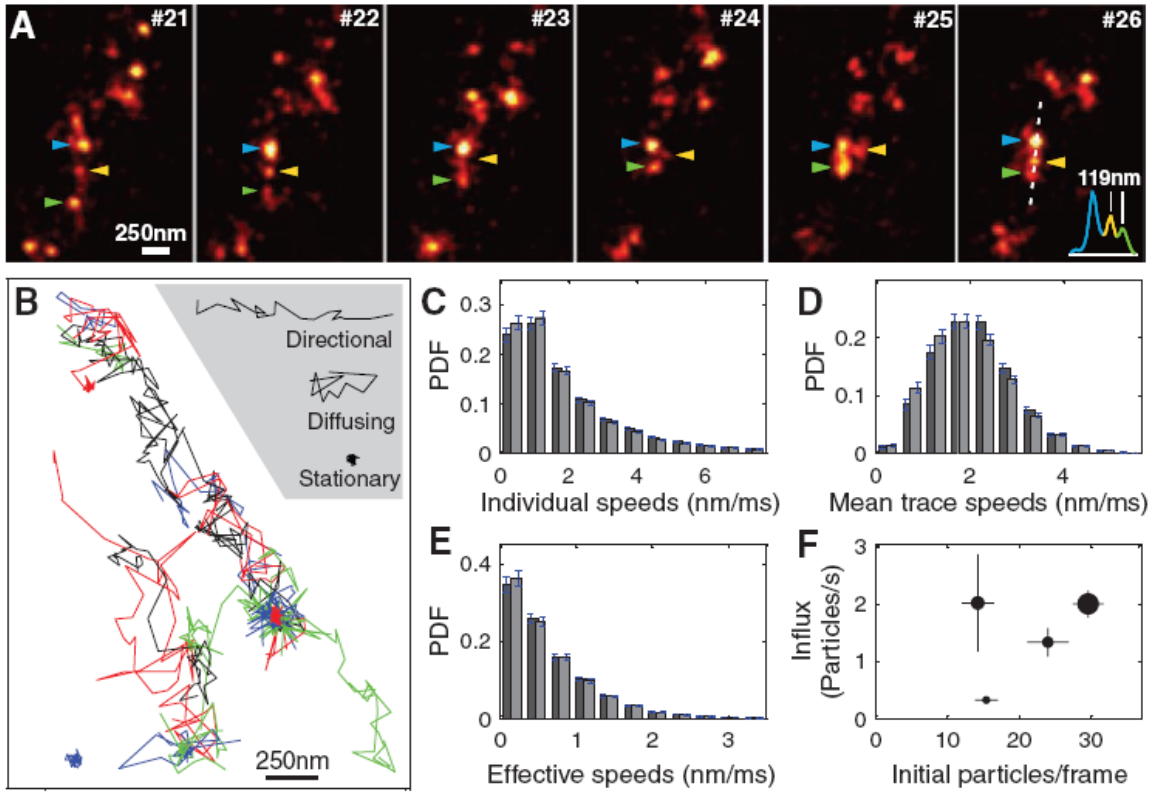

Fig. 2. Characteristics of synaptic vesicle movement. (**A**) Successive STED frames, filtered (movie S1). The arrowheads indicate three vesicles, which were tracked in all frames, localized in a sub-diffraction space. The inset in frame #26 shows an intensity profile along the dotted white line. (**B**) Example vesicle traces in one movie. Occasionally, vesicles may seem trapped in a small area, whereas other traces are reminiscent of active transport (examples in inset). (**C** to **E**) Histograms of vesicle speeds: (C) based on displacement between two consecutive frames, (D) mean speed per trace, and (E) effective speed determined by dividing the distance between the end and the origin of the trace by the trace duration. See (*20*) for details of the analysis. The results are shown as the mean ± SEM, with movies analyzed from four independent experiments. Black bars show results with normal buffer (53 movies); depolarized preparations (Tyrode solution containing 70 mM KCl) are shown in gray (75 movies). (**F**) Number of vesicles (traces) entering the imaged area per second, as a function of the number of vesicles detected in the first frames of the movie. Results from four independent experiments, each consisting of a number of movies, are shown. The circle area is proportional to the number of movies analyzed. PDF: probability density function (probability normalized to unity).

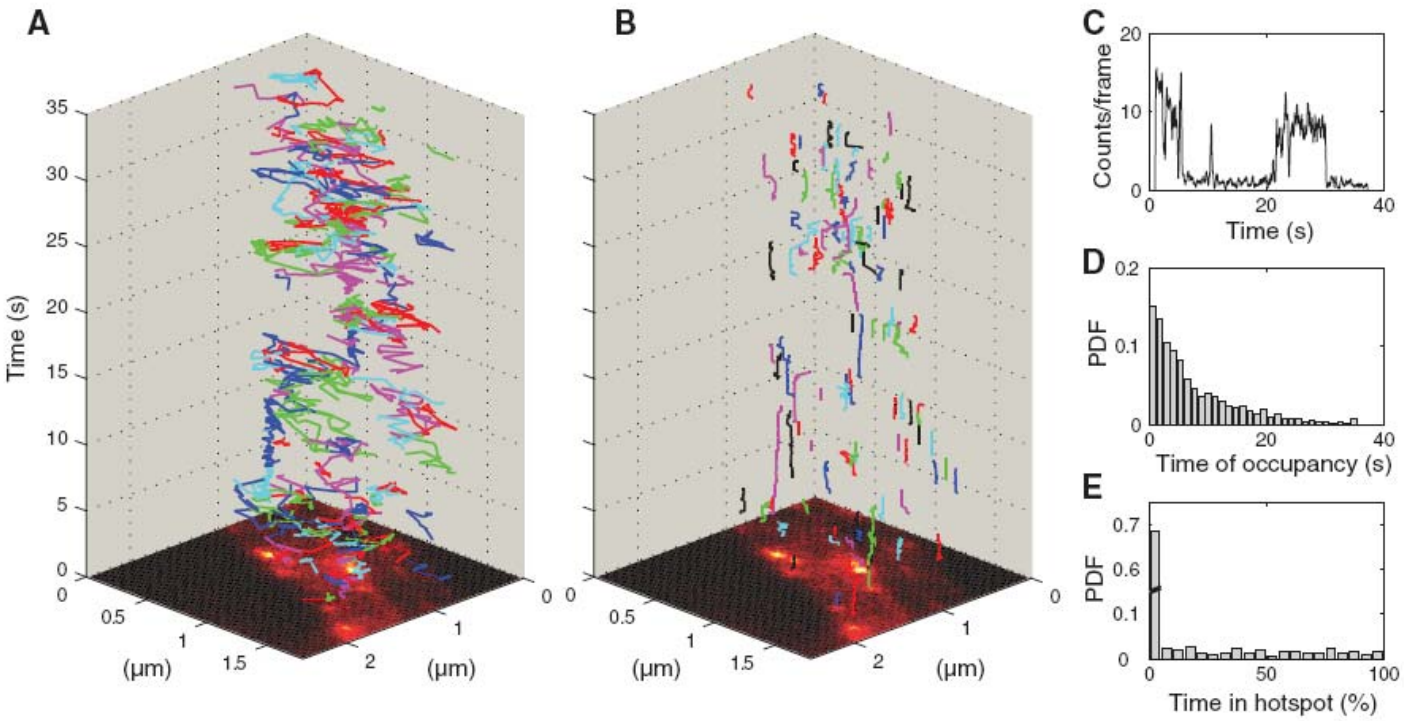

Fig. 4. Hot spots of vesicle localization. Comparison between synaptic vesicle traces (**A**) and hot spot traces (**B**). Hot spots were defined as pointlike objects appearing in a 50-frame moving average; they indicate small areas where fluorescence occurs over longer times (*20*). The average image of the complete movie is placed at the bottom. (**C**) Vesicles can move in and remain trapped in hot spots, as shown here by the strong signal fluctuation in a single hot spot. (**D**) Probability histogram of the occupancy time of the hot spots (the fraction of time they were filled by vesicles). (**E**) Histogram of the percentage of time each vesicle spent in a hot spot.

4 Pi

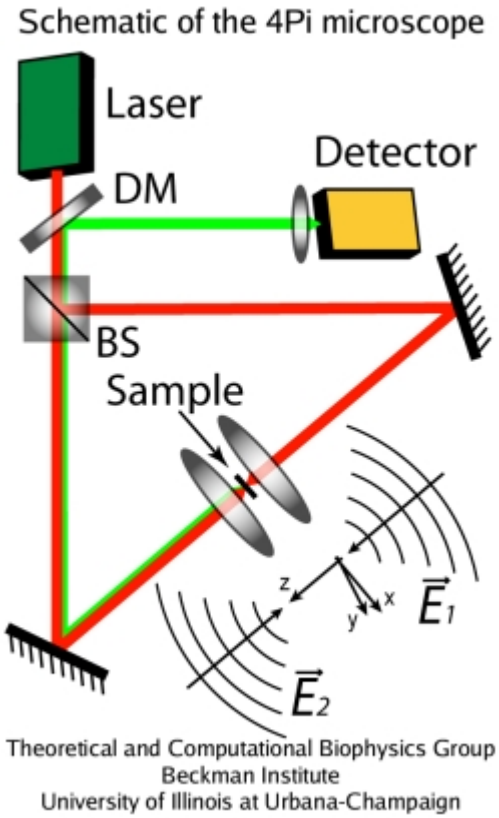
Schematic of the 4Pi microscope
Laser
Detector
DM
BS
Sample
$\vec{E}_1$
$\vec{E}_2$
Theoretical and Computational Biophysics Group
Beckman Institute
University of Illinois at Urbana-Champaign

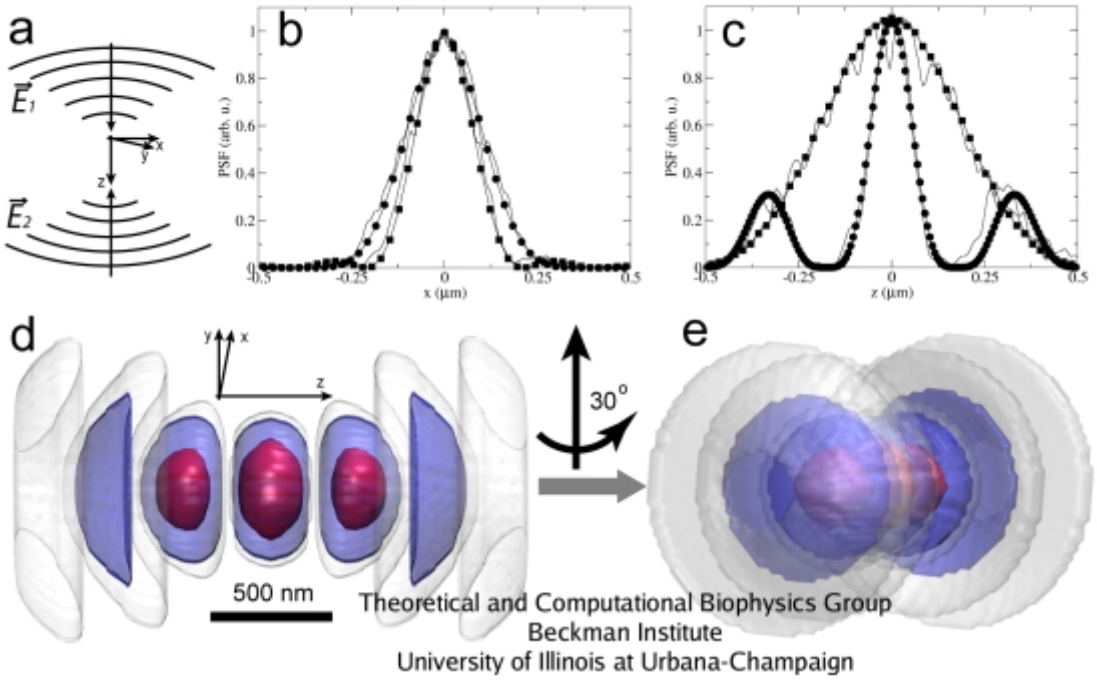
a
b
c
d
e
$\vec{E}_1$
$\vec{E}_2$
PSF (arb. u.)
x (μm)
z (μm)
30°
500 nm
Theoretical and Computational Biophysics Group
Beckman Institute
University of Illinois at Urbana-Champaign

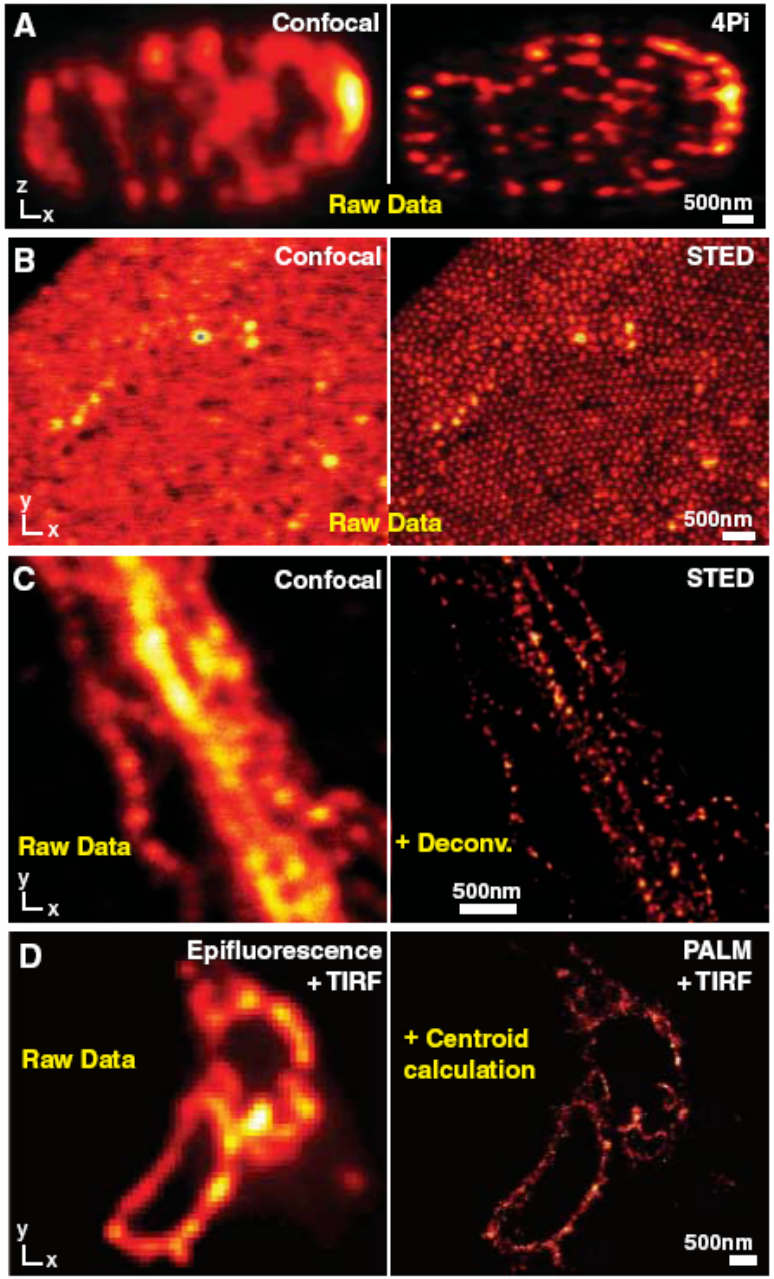

Fig. 4. Side-by-side comparisons. (**A**) Confocal versus 4Pi axial (*xz*) image of microtubules in a neuron: 4Pi image displays 140-nm *z* resolution; lens of $\alpha = 74°$ and with two-photon excitation at 800 nm. The plain 4Pi image is due to a narrow solitary peak without lobes; mathematical lobe-removal is not required. (**B**) Unlike the confocal reference, the STED image reveals the spatial order of self-assembled fused silica nanobeads containing a fluorescence core (*45*). (**C**) Neurofilaments in human neuroblastoma recorded in the confocal mode (left) and with STED after nonlinear deconvolution (right) displaying a focal plane resolution of 20 to 30 nm (*39*). (**D**) Epifluorescence versus PALM recording of a cryoprepared section from a mammalian cell expressing a lysosomal transmembrane protein tagged with a photoswitchable protein; both images were recorded with a TIRF setup. PALM resolution ranges between 20 and 60 nm, whereas individual protein localizations can be 2 nm (*12*).

Imaging Intracellular Fluorescent Proteins at Nanometer Resolution

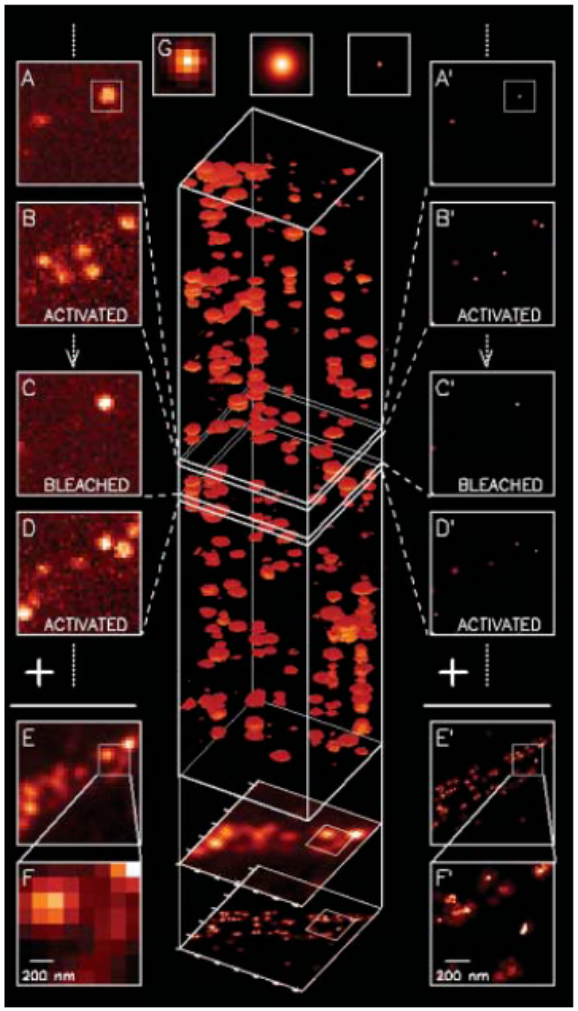

$$(\sigma_{x,y}{}^2)_m \approx \frac{s^2 + a^2/12}{N_m} + \frac{4\sqrt{\pi} s^3 b_m{}^2}{a N_m{}^2}$$

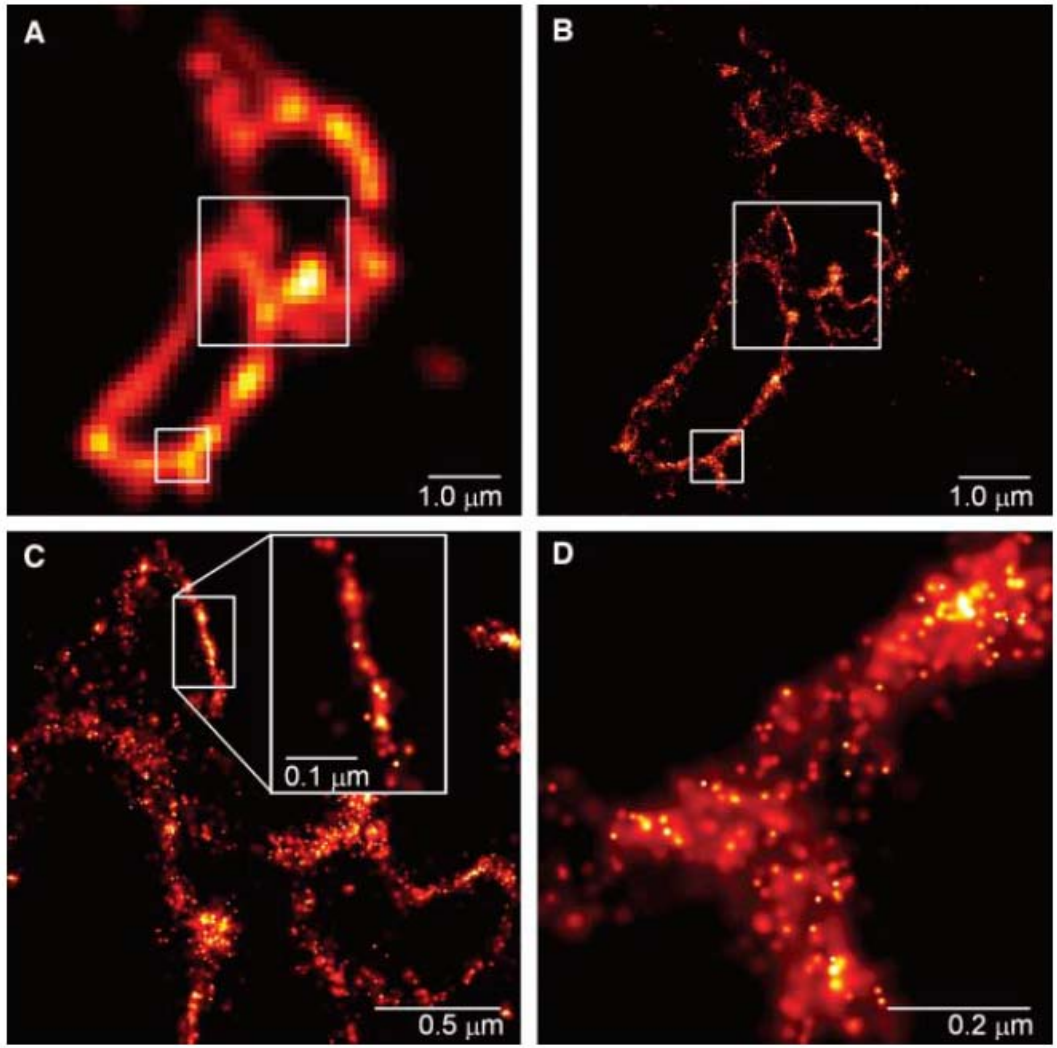

Fig. 2. Comparative summed-molecule TIRF (**A**) and PALM (**B**) images of the same region within a cryo-prepared thin section from a COS-7 cell expressing the lysosomal transmembrane protein CD63 tagged with the PA-FP Kaede. The larger boxed region in (B), when viewed at higher magnification (**C**) reveals smaller associated membranes that may represent interacting lysosomes or late endosomes that are not resolvable by TIRF. In a region where the section is nearly orthogonal to the lysosomal membrane, the most highly localized molecules fall on a line of width ~10 nm (inset). In an obliquely cut region [(**D**), from the smaller boxed region in (B)], the distribution of CD63 within the membrane plane can be discerned.

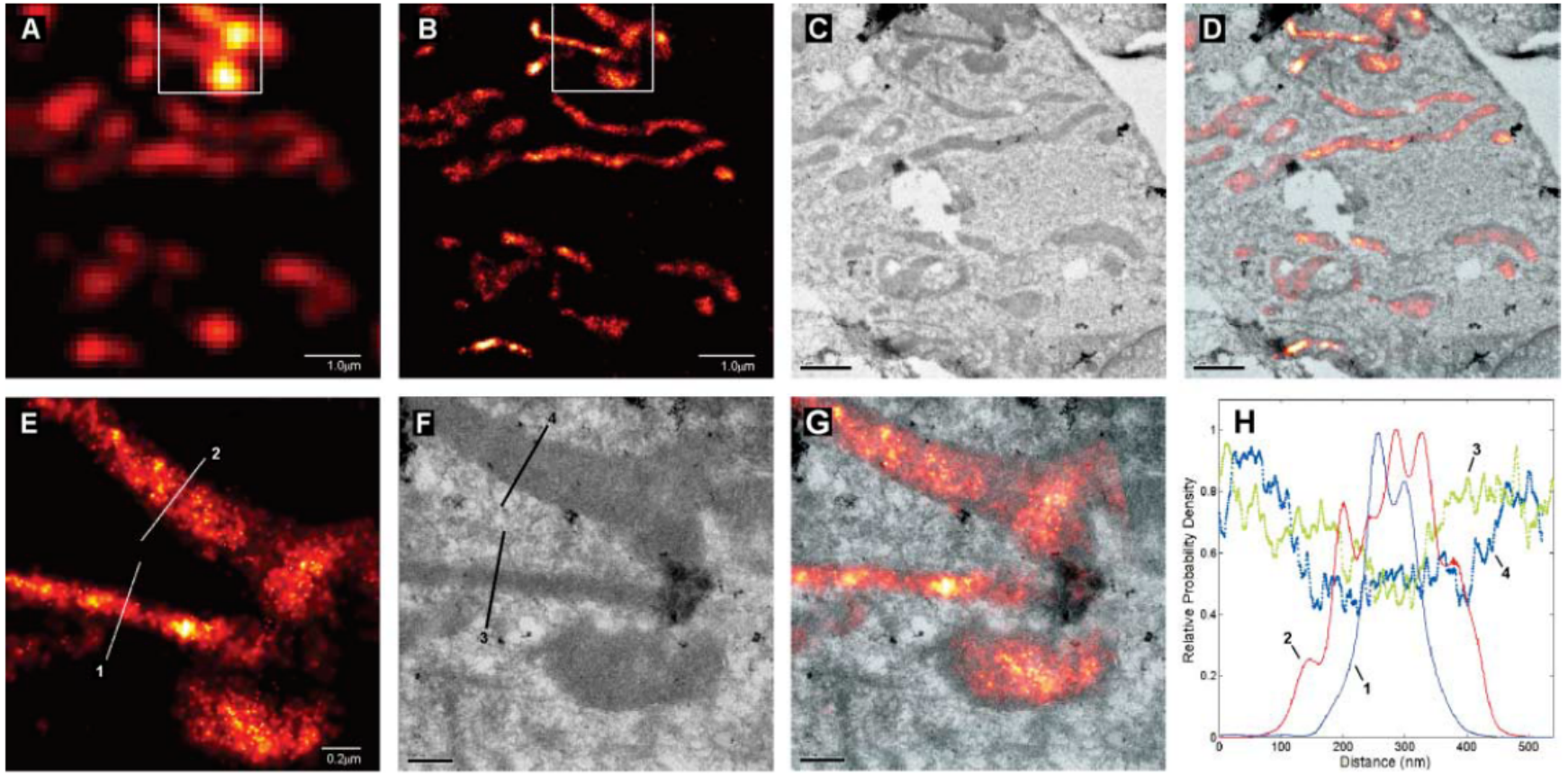

Fig. 3. Comparative summed-molecule TIRF (**A**), PALM (**B**), TEM (**C**), and PALM/TEM overlay (**D**) images of mitochondria in a cryo-prepared thin section from a COS-7 cell expressing dEosFP-tagged cytochrome-C oxidase import sequence. Higher magnification PALM (**E**), TEM (**F**), and overlay (**G**) images within the box in (B) reveal that these matrix reporter molecules extend up to, but not into, the ~20-nm outer mitochondrial membrane. The molecular distribution across two mitochondria along lines 1 and 2 in PALM image (E) are compared in (**H**) to the TEM signal along lines 3 and 4 in (F) across the same mitochondria. Scale bars: 1.0 μm in (A) to (D); 0.2 μm in (E) to (G).

Sub-diffraction-limit imaging by stochastic optical reconstruction microscopy (STORM)

Michael J Rust[1,5], Mark Bates[2,5] & Xiaowei Zhuang[1,3,4]

NATURE METHODS

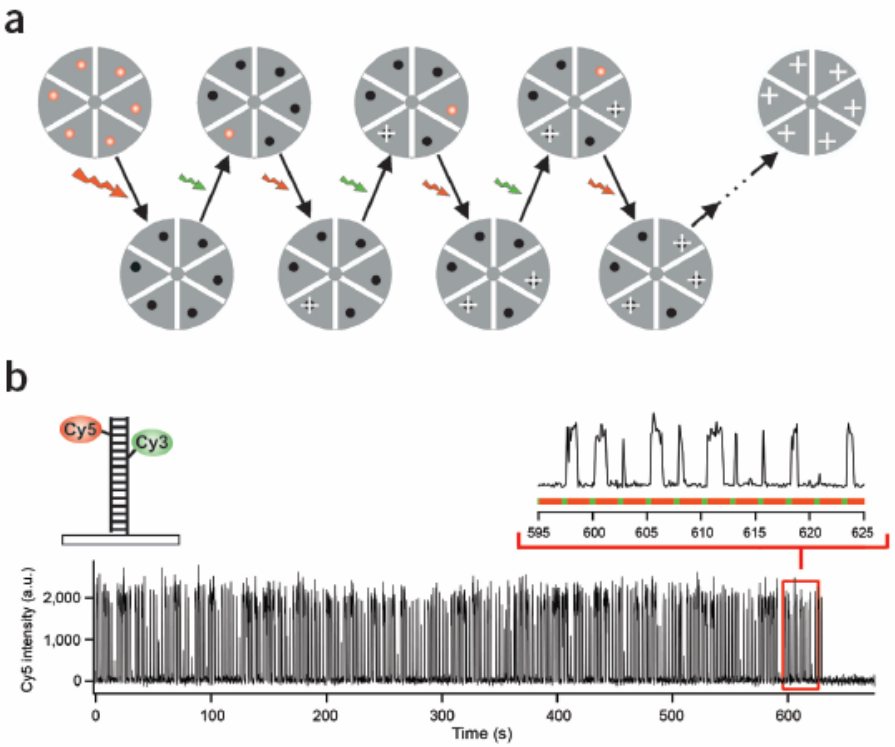

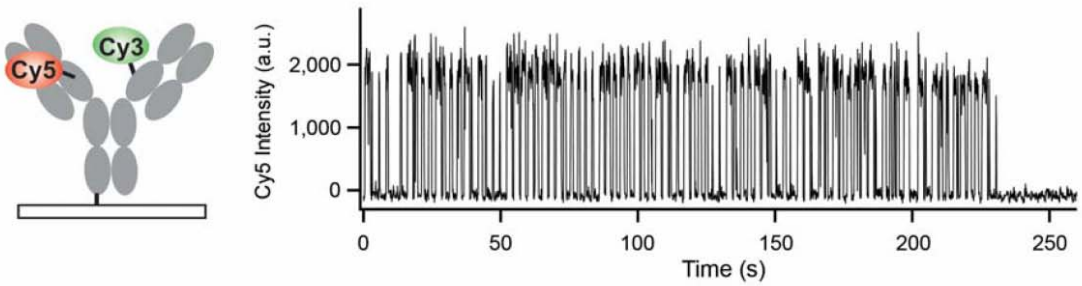

: 2.2 : 1 for Cy3 and 0.1 : 1 for Cy5

Goat anti-mouse secondary antibody labeled with the cyanine switch exhibits photoswitching behavior similar to switch-labeled DNA. The antibody was labeled with Cy3 and Cy5 (as described in **Supplementary Methods** online) and bound to a quartz slide coated with unlabeled mouse anti-transferrin primary antibody. The trace shows the Cy5 fluorescence intensity detected from a single labeled antibody as it switches on and off until permanent photobleaching occurs after 230 seconds. A red laser (633 nm, 30 W/cm^2) is used to excite fluorescence from Cy5 and to switch Cy5 to the dark state. A green laser (532 nm, 1 W/cm^2) is used to switch the Cy5 back to the fluorescent state. The sample was excited with a sequence of alternating green and red laser pulses (0.5 s green followed by 2 s red).

$$I(x,y) = A + I_0 e^{\left[-(x'/a)^2-(y'/b)^2\right]/2}$$

$$x' = (x - x_0)\cos\theta - (y - y_0)\sin\theta$$
$$y' = (x - x_0)\sin\theta + (y - y_0)\cos\theta$$

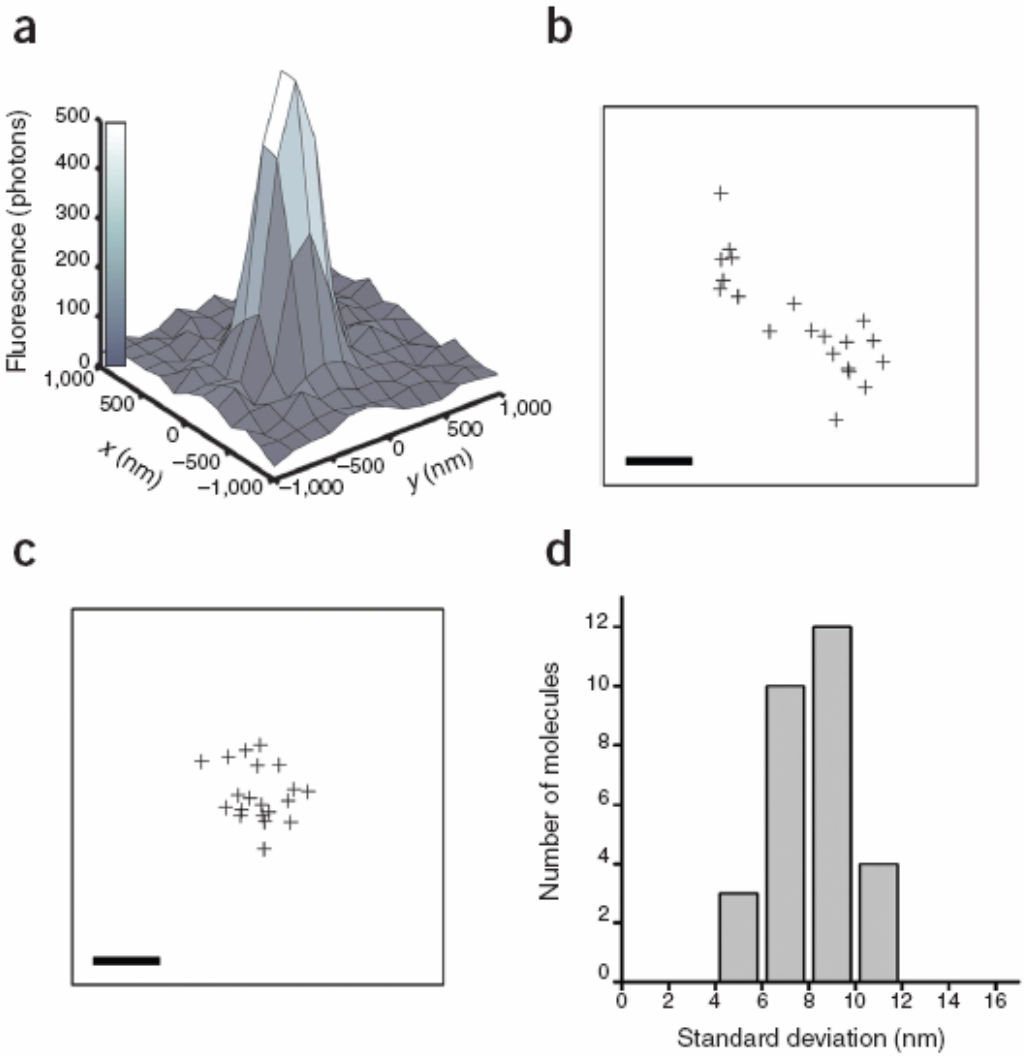

Figure 2 | The high localization accuracy of individual switches during each switching cycle defines the intrinsic resolution of STORM. (**a**) The point spread function (PSF) of the emission from a single switch on DNA during a single switching cycle. Fitting the PSF to a two-dimensional Gaussian (not shown) gives the centroid position of the PSF. (**b**,**c**) The centroid positions of an individual switch determined in 20 successive imaging cycles before (**b**) and after (**c**) correction for sample drift. Scale bars, 20 nm. (**d**) A histogram of the standard deviation of centroid positions. The standard deviation is determined as $(\sigma_x + \sigma_y) / 2$ for each switch using 20 imaging cycles, where σ_x and σ_y are the standard deviations of the centroid positions in the *x* and *y* dimensions. This histogram was constructed from 29 switches.

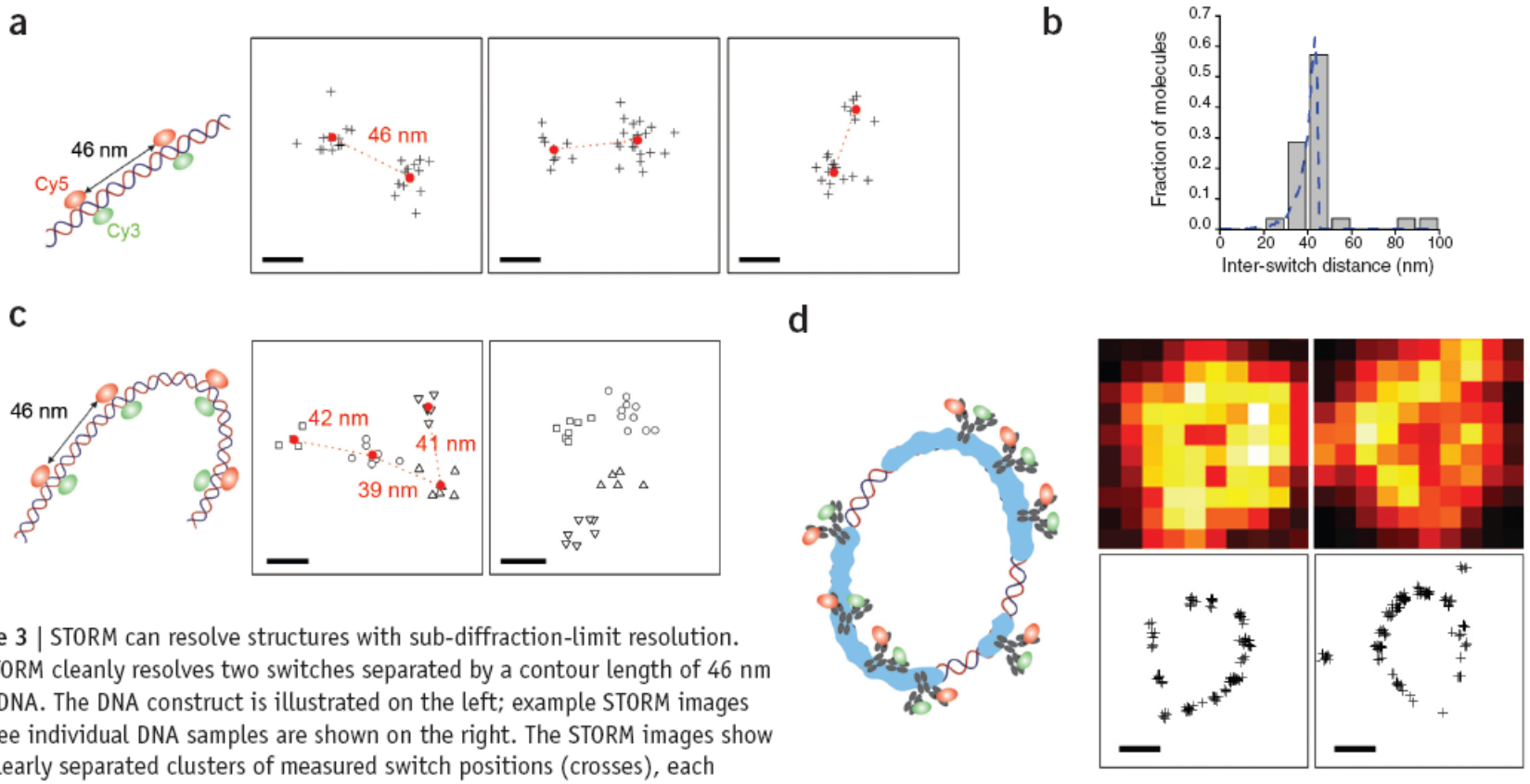

Figure 3 | STORM can resolve structures with sub-diffraction-limit resolution. (**a**) STORM cleanly resolves two switches separated by a contour length of 46 nm on dsDNA. The DNA construct is illustrated on the left; example STORM images of three individual DNA samples are shown on the right. The STORM images show two clearly separated clusters of measured switch positions (crosses), each corresponding to a single switch. The center-of-mass position of each cluster is marked by a red dot. The inter-switch distances are 46 nm, 44 nm and 34 nm for these three examples. Scale bars, 20 nm. (**b**) Comparison between the inter-switch distances measured using STORM (columns) and the predicted distance distribution considering the flexibility of DNA (dashed line). (**c**) STORM images of four switches attached to a dsDNA, pair-wise separated by a contour length of 46 nm. The measured switch positions are clustered by an automated algorithm and different clusters are indicated by different symbols. Scale bars, 20 nm. (**d**) STORM images of RecA-coated circular plasmid DNA. Indirect immunofluorescence images with switch-labeled secondary antibody taken by a total internal reflection microscope (top); the reconstructed STORM images of the same filaments (bottom). Scale bars, 300 nm.

Multicolor Super-Resolution Imaging with Photo-Switchable Fluorescent Probes

SCIENCE VOL 317 21 SEPTEMBER 2007

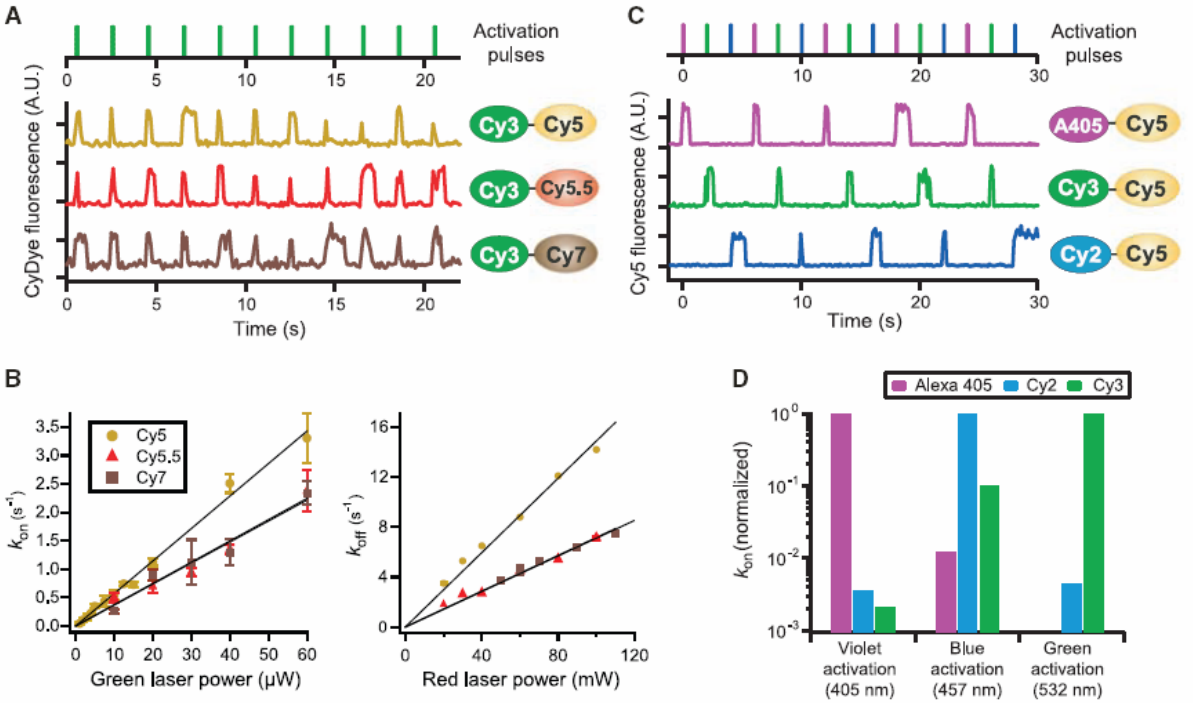

Fig. 1. Photo-switchable probes constructed from activator-reporter pairs. (**A**) Spectrally distinct reporters exhibit photo-switching behavior. The lower panel shows the fluorescence time traces of three photo-switchable reporters Cy5 (dark yellow line), Cy5.5 (red line), and Cy7 (brown line), each paired with a Cy3 dye as the activator on a DNA construct. The upper panel shows the green laser pulses (532 nm) used to activate the reporters. The red laser (657 nm) was continuously on, serving to excite fluorescence from the reporters and to switch them to the dark state. Traces were shifted relative to each other for clarity. (**B**) Switching rate constants k_{on} and k_{off} of the Cy3-Cy5, Cy3-Cy5.5, and Cy3-Cy7 pairs as a function of green and red laser power. Error bars indicate SEM from about three data sets. The laser power to intensity calibration may vary between different samples because of moderate differences in the laser spot size at the sample. (**C**) The same reporter can be activated by spectrally distinct activators. The lower panel shows the fluorescence time traces of Cy5 paired with three different activators, Alexa 405 (magenta line), Cy2 (blue line), and Cy3 (green line). The upper panel shows the violet (405 nm, magenta line), blue (457 nm, blue line), and green (532 nm, green line) activation pulses. (**D**) Normalized activation rate constants of the three dye pairs at three activation wavelengths: 405, 457, and 532 nm. The k_{on} values of Alexa 405-Cy5, Cy2-Cy5, and Cy3-Cy5 were used for normalization at 405, 457, and 532 nm, respectively. The absolute activation rates were rapid for each pair at its corresponding optimal wavelength, with values of 10 s^{-1} or greater at only a few hundred μW of laser power. The activation rate of the Alexa 405-Cy5 pair by the 532-nm laser was too small to be measured reliably.

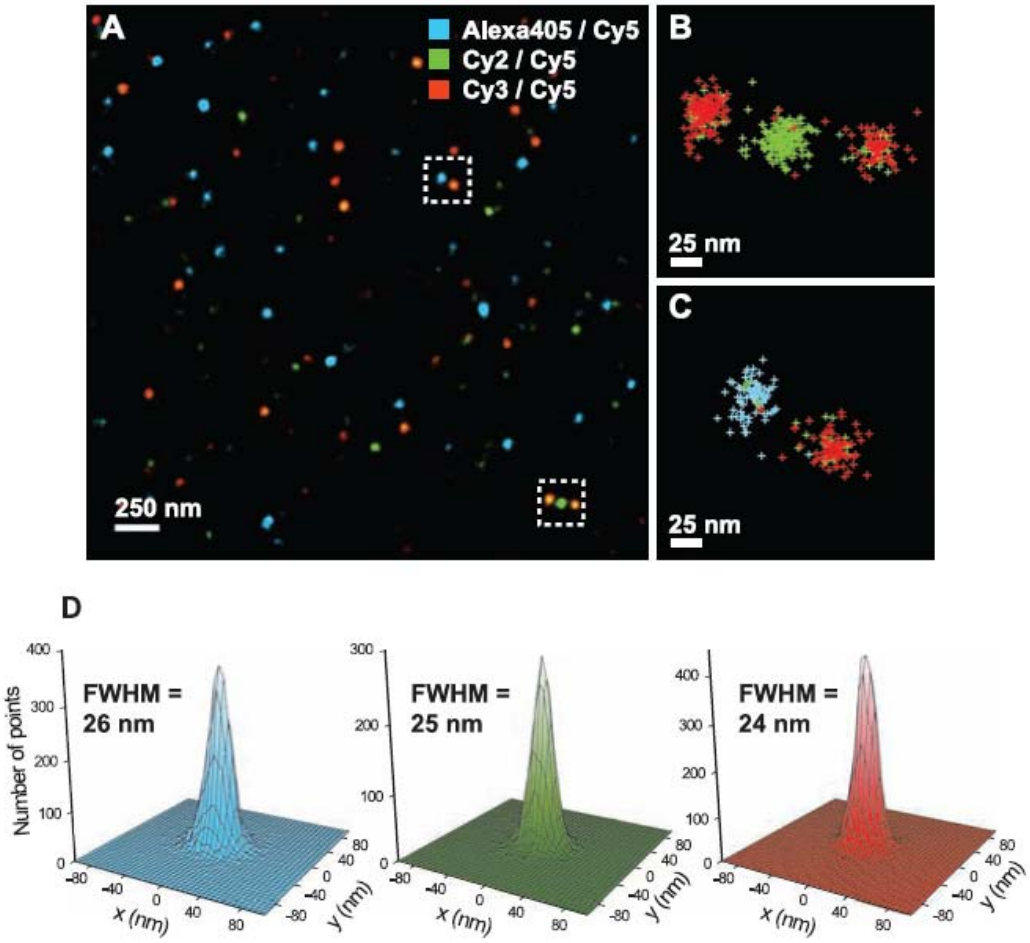

Fig. 2. Three-color STORM imaging of a model DNA sample. (**A**) Three-color STORM image of three different DNA constructs labeled with Alexa 405-Cy5, Cy2-Cy5, or Cy3-Cy5 mixed at a high surface density on a microscope slide. The image was plotted by rendering each localization as a Gaussian peak, the width of which was scaled with the theoretical localization accuracy given by the number of photons detected (*26*). Each colored spot in this image represents a cluster of localizations from a single DNA molecule. A conventional fluorescence image of the same area is shown in fig. S3 for comparison. (**B** and **C**) Higher-magnification views of the boxed regions in (A) show several examples of closely spaced DNA molecules. Each localization was plotted as a cross, colored according to the following code: If the molecule was activated by a 405-, 457-, or 532-nm laser pulse, the color of the cross was assigned as blue, green, or red, respectively. (**D**) The localization distributions of the blue, green, or red clusters. The two-dimensional histograms of localizations were generated by aligning multiple (50 to 60) clusters by their center of mass. The histograms were fit to a Gaussian profile to determine their FWHM.

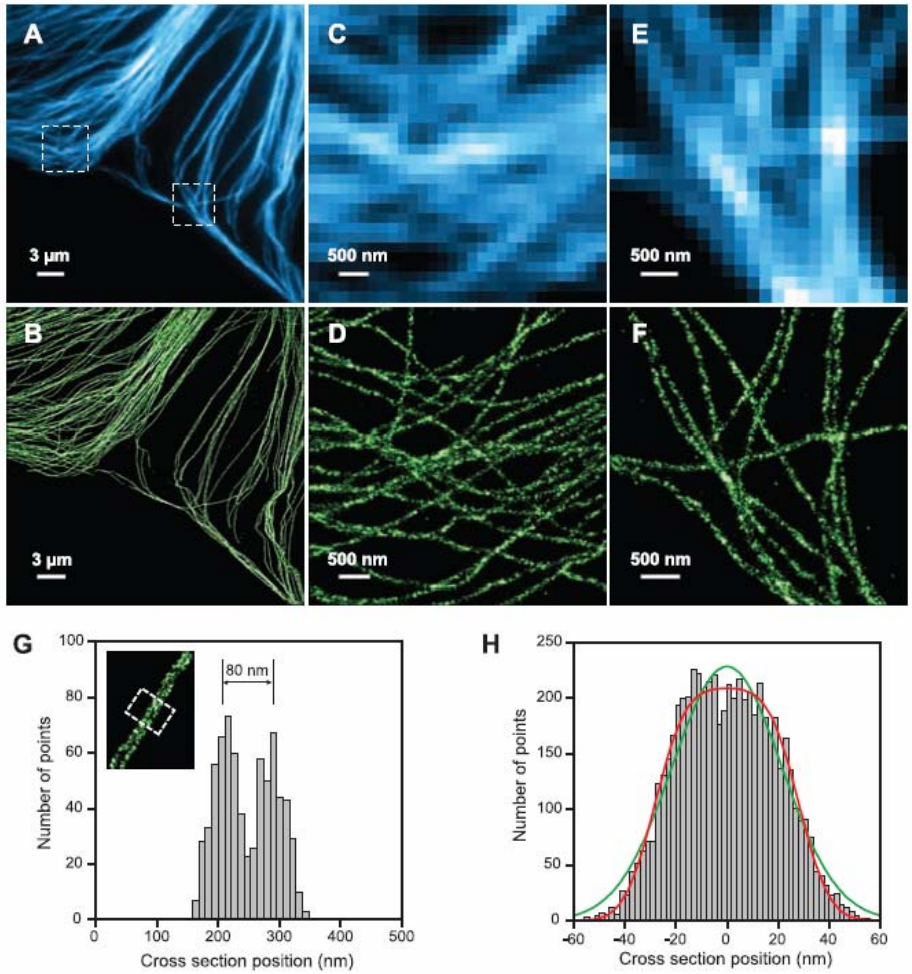

Fig. 3. STORM imaging of microtubules in a mammalian cell. (**A**) Conventional immunofluorescence image of microtubules in a large area of a BS-C-1 cell. (**B**) STORM image of the same area. (**C** and **E**) Conventional and (**D** and **F**) STORM images corresponding to the boxed regions in (A). (**G**) Cross-sectional profiles of two nearby microtubule filaments in the cell. The inset shows the STORM image, and the histogram shows the cross-sectional distribution of localizations within the small regions specified by the white box. (**H**) Cross-sectional profile of a microtubule segment determined from the STORM image. A relatively long segment (~7 µm) was chosen to obtain good statistics. The histogram shows the cross-sectional distribution of localizations. The green line is a single Gaussian fit with FWHM = 51 nm. The red line shows the fit obtained by convolving a rectangular function of width = d with a Gaussian function of FWHM = r. The fit yields d = 56 nm and r = 22 nm, corresponding to the antibody-coated microtubule width and the imaging resolution, respectively.

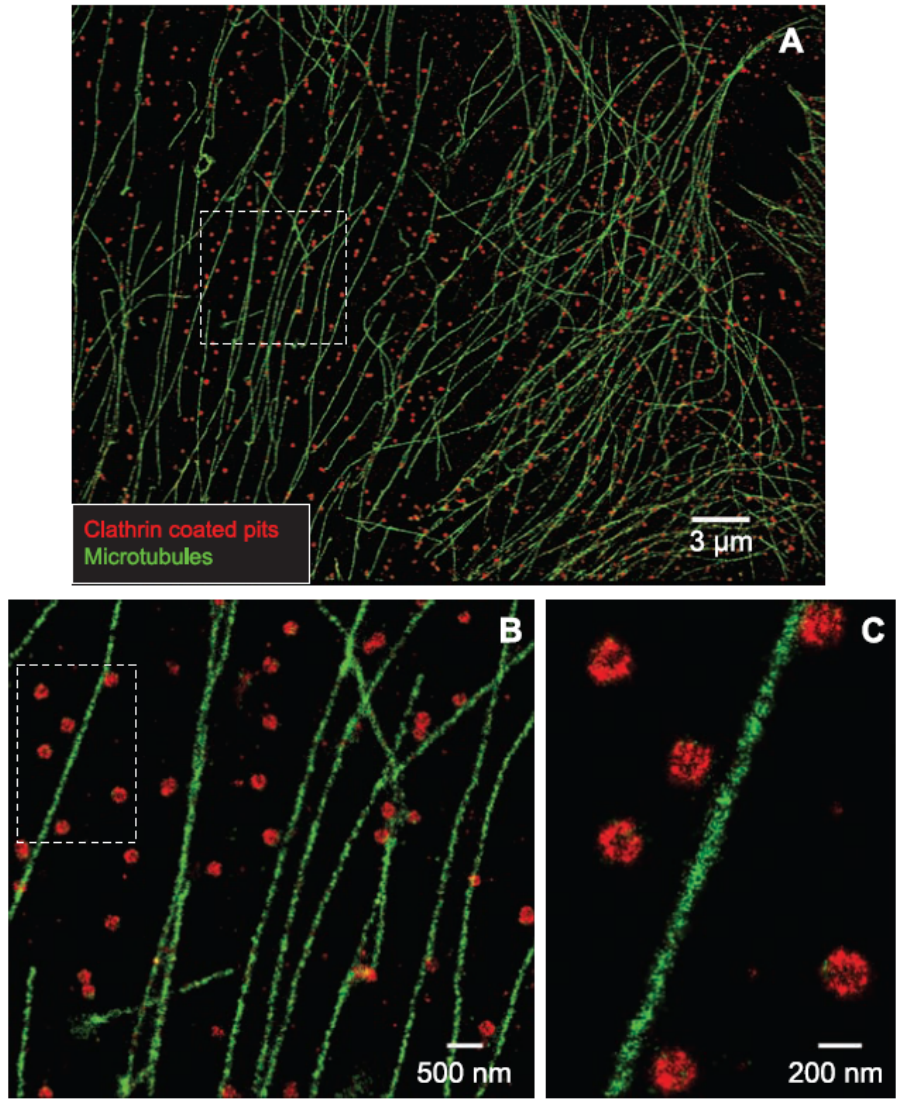

Fig. 4. Two-color STORM imaging of microtubules and CCPs in a mammalian cell. (**A**) STORM image of a large area of a BS-C-1 cell. The secondary antibodies used for microtubule staining were labeled with Cy2 and Alexa 647, and those for clathrin were labeled with Cy3 and Alexa 647. The 457- and 532-nm laser pulses were used to selectively activate the two pairs. Each localization was false colored according to the following code: green for 457-nm activation and red for 532-nm activation. (**B**) STORM image corresponding to the boxed region in (A) shown at a higher magnification. (**C**) Further magnified view of the boxed region in (B).

Three-Dimensional Super-Resolution Imaging by Stochastic Optical Reconstruction Microscopy

8 FEBRUARY 2008 VOL 319 SCIENCE

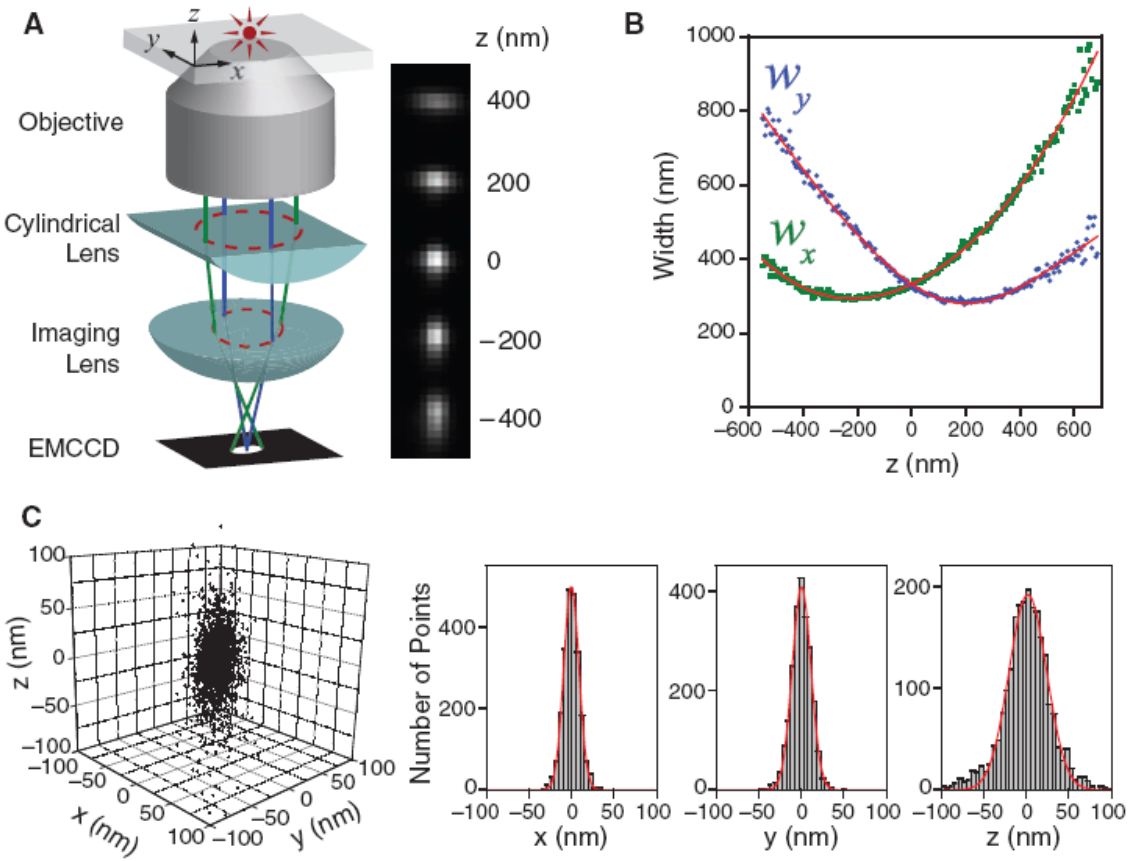

Fig. 1. The scheme of 3D STORM. (**A**) Three-dimensional localization of individual fluorophores. The simplified optical diagram illustrates the principle of determining the *z* coordinate of a fluorescent object from the ellipticity of its image by introducing a cylindrical lens into the imaging path. The right panel shows images of a fluorophore at various *z* positions. EMCCD, electron-multiplying charge-coupled device. (**B**) Calibration curve of image widths w_x and w_y as a function of *z* obtained from single Alexa 647 molecules. Each data point represents the average value obtained from six molecules. The data were fit to a defocusing function (red curve) as described in (*27*). (**C**) Three-dimensional localization distribution of single molecules. Each molecule gives a cluster of localizations due to repetitive activation of the same molecule. Localizations from 145 clusters were aligned by their center of mass to generate the overall 3D presentation of the localization distribution (left panel). Histograms of the distribution in *x*, *y*, and *z* (right panels) were fit to a Gaussian function, yielding standard deviations of 9 nm in *x*, 11 nm in *y*, and 22 nm in *z*.

Fig. 2. Three-dimensional STORM imaging of microtubules in a cell. (**A**) Conventional indirect immunofluorescence image of microtubules in a large area of a BS-C-1 cell. (**B**) The 3D STORM image of the same area, with the *z*-position information color-coded according to the color scale bar. Each localization is depicted in the STORM image as a Gaussian peak, the width of which is determined by the number of photons detected (*5*). (**C** to **E**) The *x-y*, *x-z*, and *y-z* cross sections of a small region of the cell outlined by the white box in (B), showing five microtubule filaments. Movie S1 shows the 3D representation of this region, with the viewing angle rotated to show different perspectives (*27*). (**F**) The *z* profile of two microtubules crossing in the *x-y* projection but separated by 102 nm in *z*, from a region indicated by the arrow in (B). The histogram shows the distribution of *z* coordinates of the localizations, fit to two Gaussians with identical widths (FWHM = 66 nm) and a separation of 102 nm (red curve). The apparent width of 66 nm agrees quantitatively with the convolution of our imaging resolution in *z* (represented by a Gaussian function with FWHM of 55 nm) and the previously measured width of antibody-coated microtubules (represented by a uniform distribution with a width of 56 nm) (*5*).

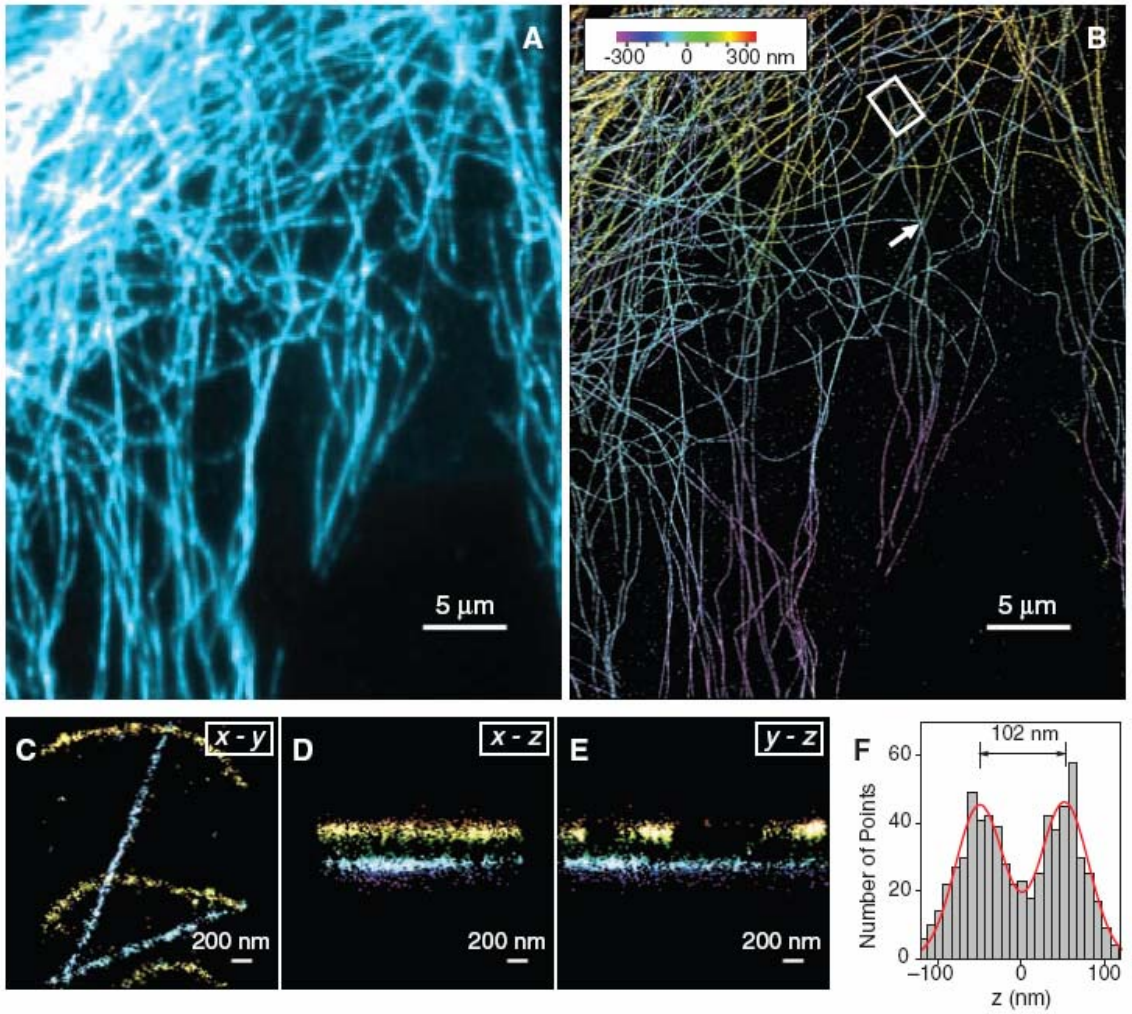

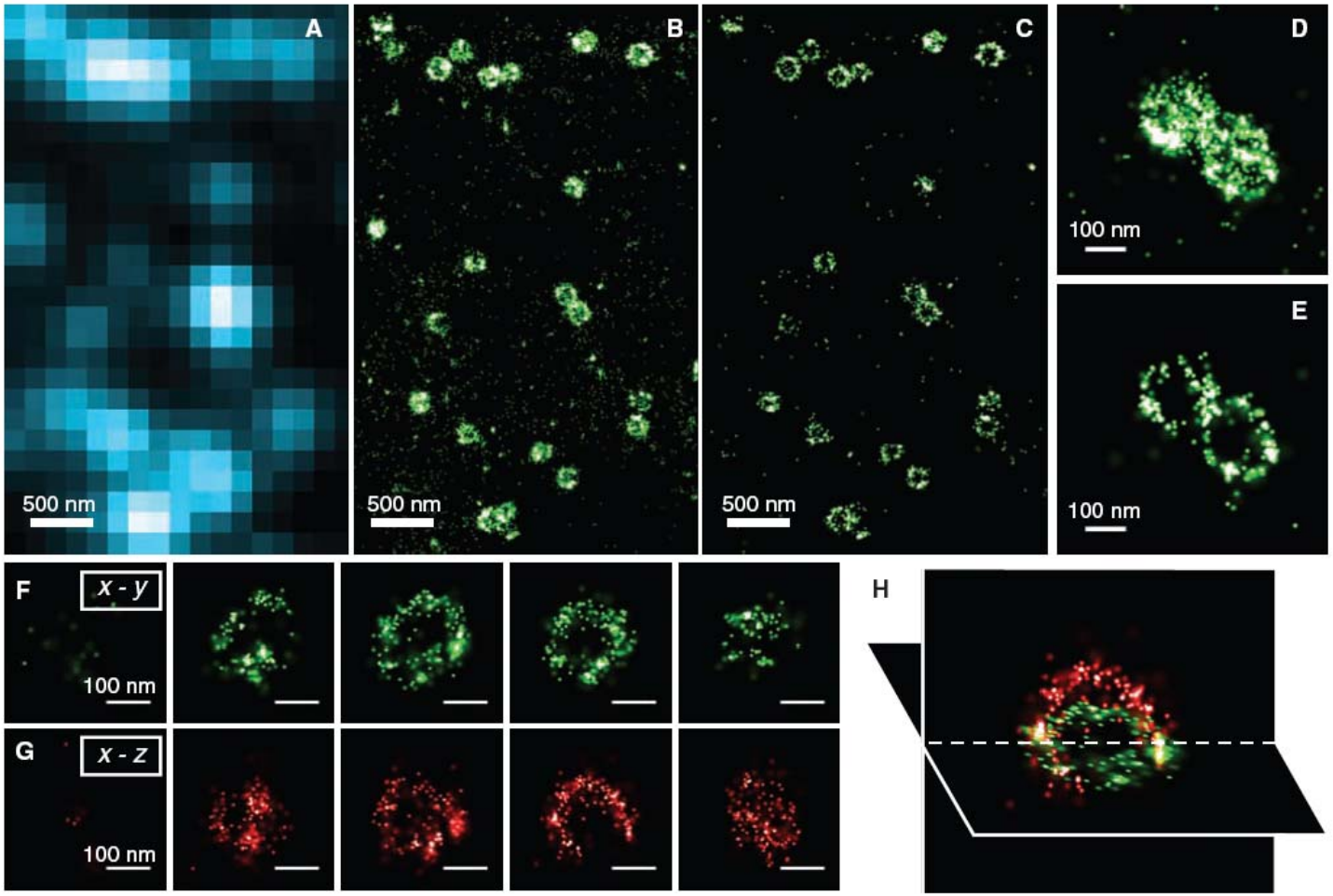

Fig. 3. Three-dimensional STORM imaging of clathrin-coated pits in a cell. (**A**) Conventional direct immunofluorescence image of clathrin in a region of a BS-C-1 cell. (**B**) The 2D STORM image of the same area, with all localizations at different *z* positions included. (**C**) An *x-y* cross section (50 nm thick in *z*) of the same area, showing the ring-like structure of the periphery of the CCPs at the plasma membrane. (**D** and **E**) Magnified view of two nearby CCPs in 2D STORM (D) and their *x-y* cross section (100 nm thick) in the 3D image (E). (**F** to **H**) Serial *x-y* cross sections (each 50 nm thick in *z*) (F) and *x-z* cross sections (each 50 nm thick in *y*) (G) of a CCP, and an *x-y* and *x-z* cross section presented in 3D perspective (H), showing the half-spherical cage-like structure of the pit.

Nonlinear structured-illumination microscopy: Wide-field fluorescence imaging with theoretically unlimited resolution

PNAS | September 13, 2005 | vol. 102 | no. 37 | 13081–13086

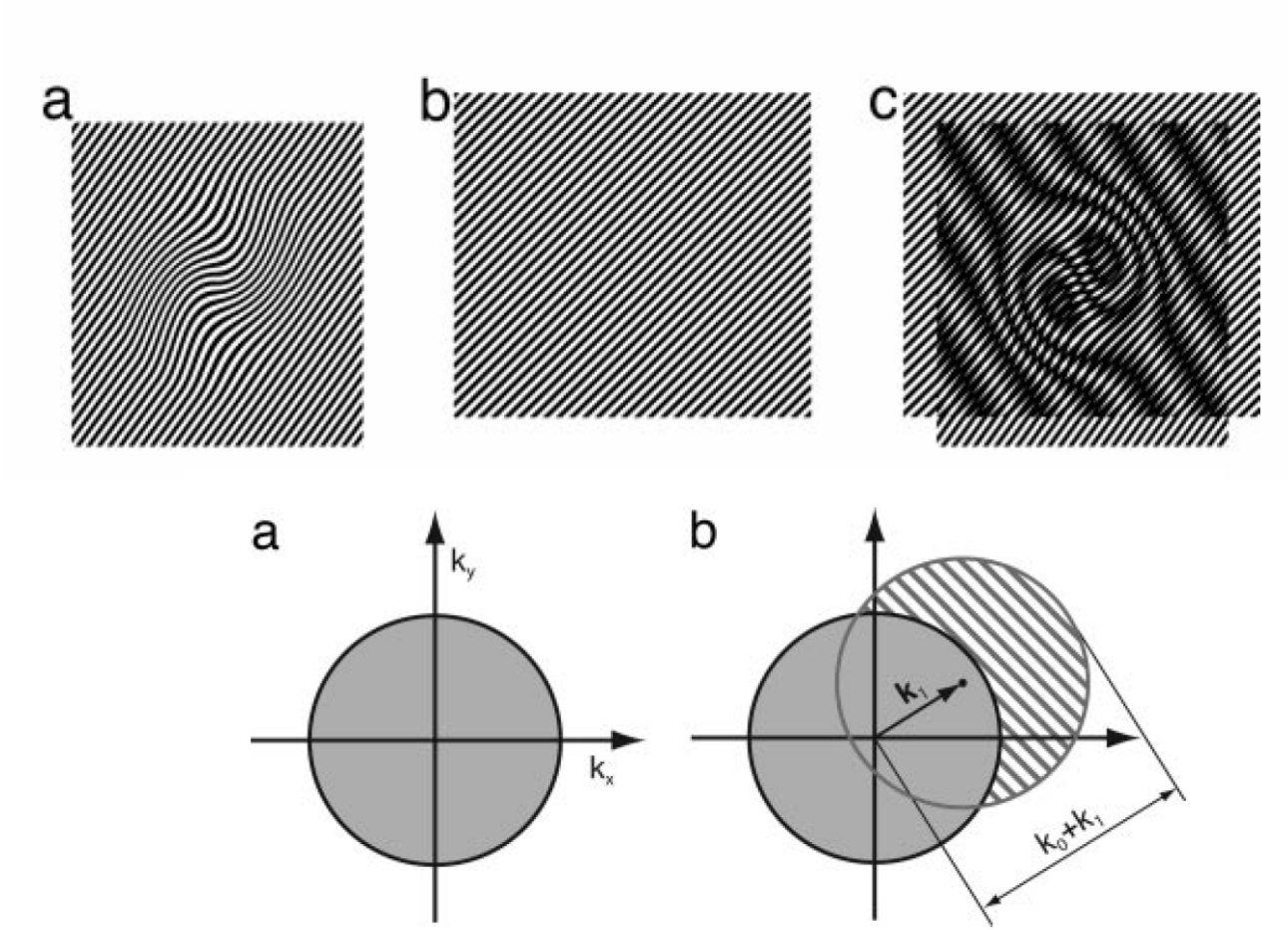

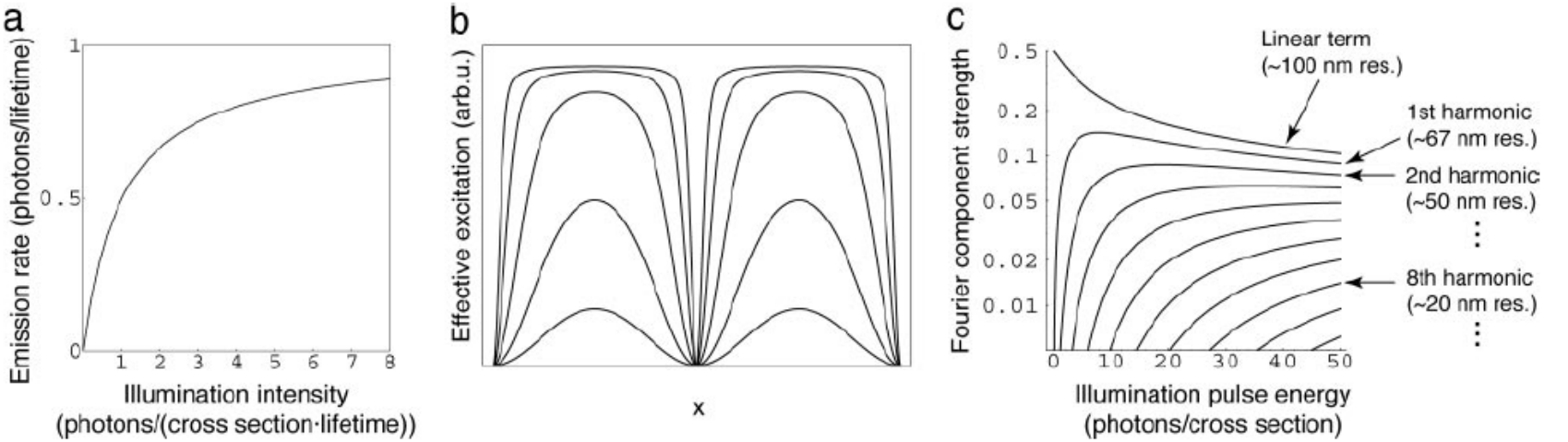
a
Emission rate (photons/lifetime)
1
0.5
0
1 2 3 4 5 6 7 8
Illumination intensity
(photons/(cross section·lifetime))
b
Effective excitation (arb.u.)
x
c
Fourier component strength
0.5
0.2
0.1
0.05
0.02
0.01
0 10 20 30 40 50
Illumination pulse energy
(photons/cross section)
Linear term
(~100 nm res.)
1st harmonic
(~67 nm res.)
2nd harmonic
(~50 nm res.)
8th harmonic
(~20 nm res.)

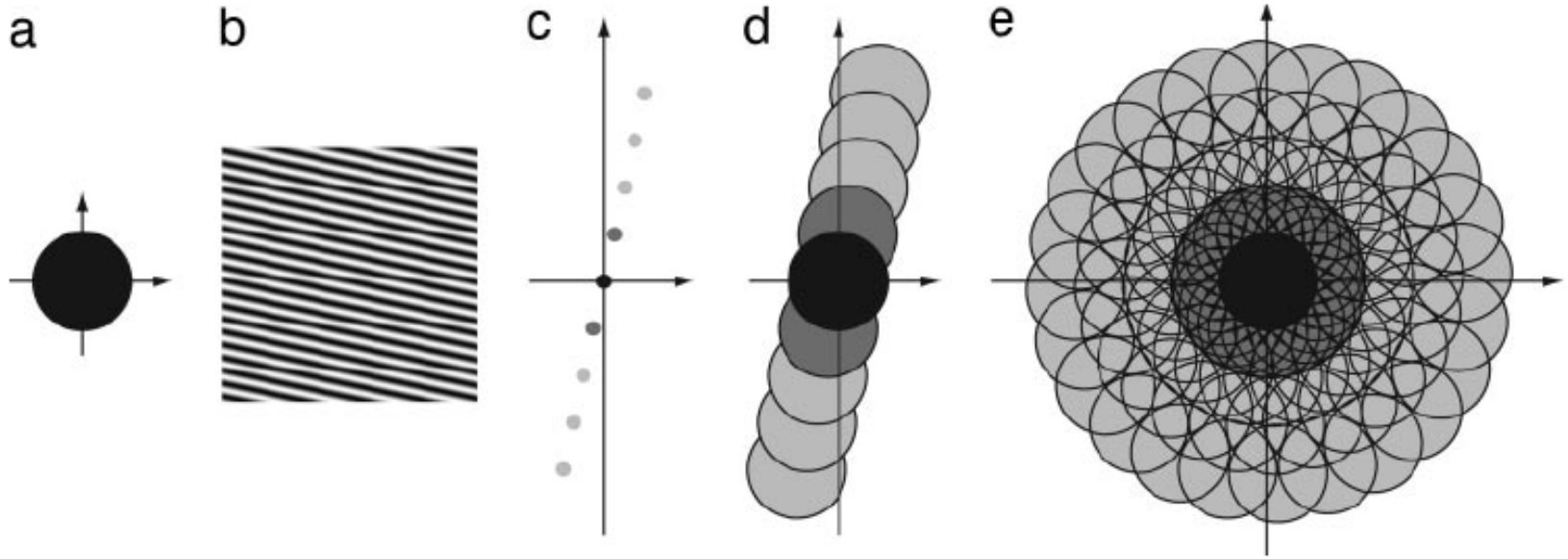
a
b
c
d
e

Super-resolution video microscopy of live cells by structured illumination

Peter Kner[1,2,7,8], Bryant B Chhun[1,8], Eric R Griffis[3,4], Lukman Winoto[5] & Mats G L Gustafsson[5,6]

NATURE METHODS | VOL.6 NO.5 | MAY 2009 | 339

Structured-illumination microscopy can double the resolution of the widefield fluorescence microscope but has previously been too slow for dynamic live imaging. Here we demonstrate a high-speed structured-illumination microscope that is capable of 100-nm resolution at frame rates up to 11 Hz for several hundred time points. We demonstrate the microscope by video imaging of tubulin and kinesin dynamics in living *Drosophila melanogaster* S2 cells in the total internal reflection mode.

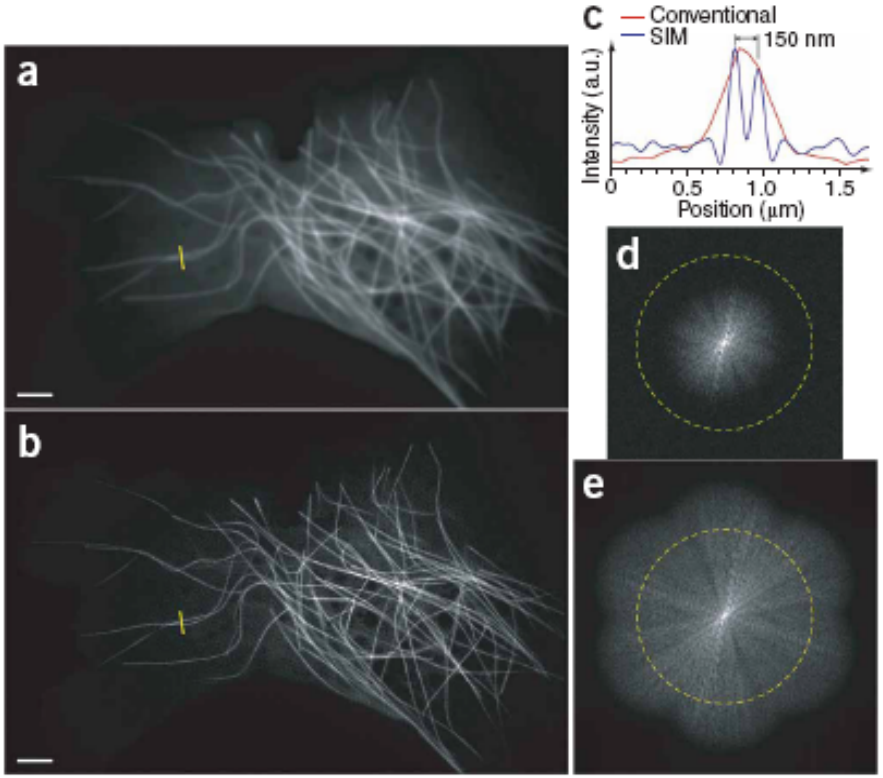

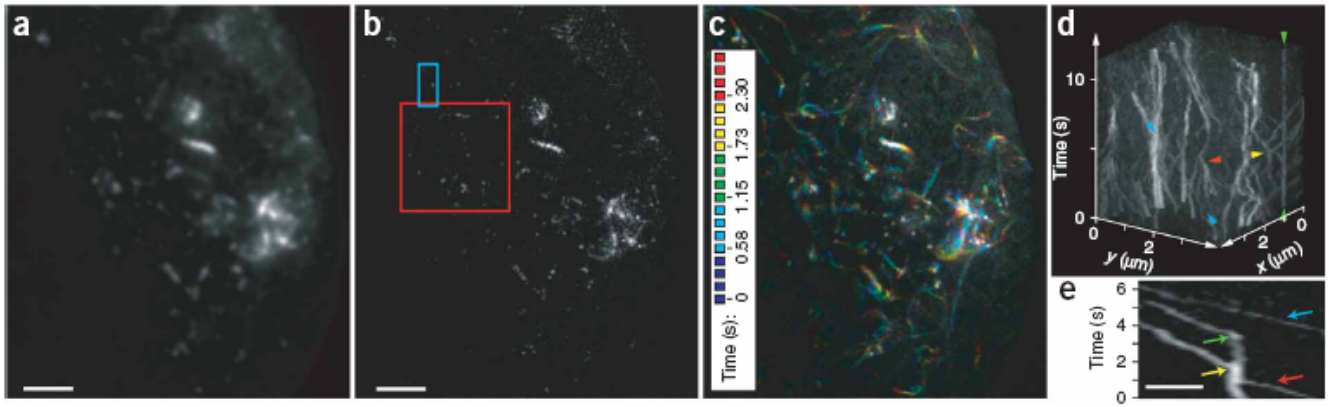

Super-Resolution Imaging by Random Adsorbed Molecule Probes

NANO LETTERS

2008
Vol. 8, No. 4
1159-1162

$$\langle (\Delta x)^2 \rangle = 4\pi^{1/2} s^3 b^2 / a N^2$$

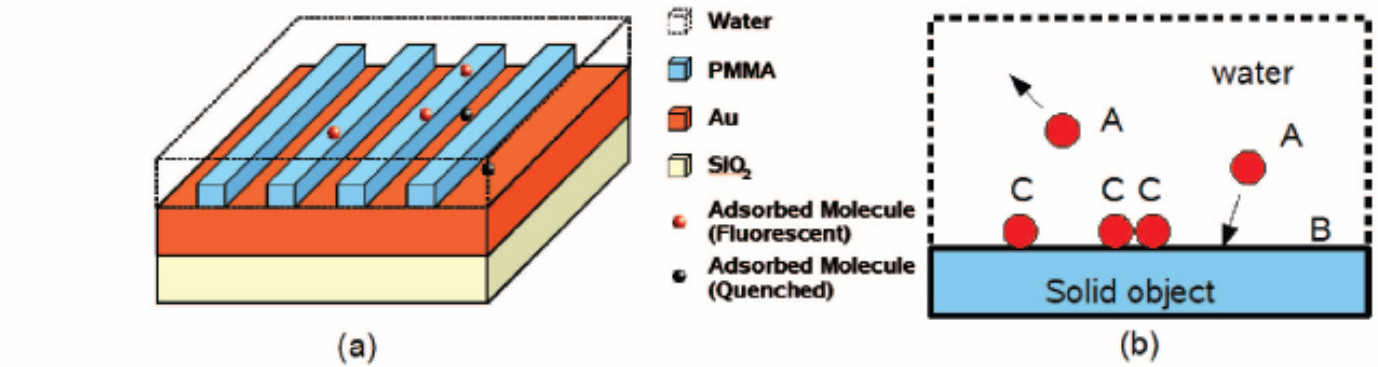

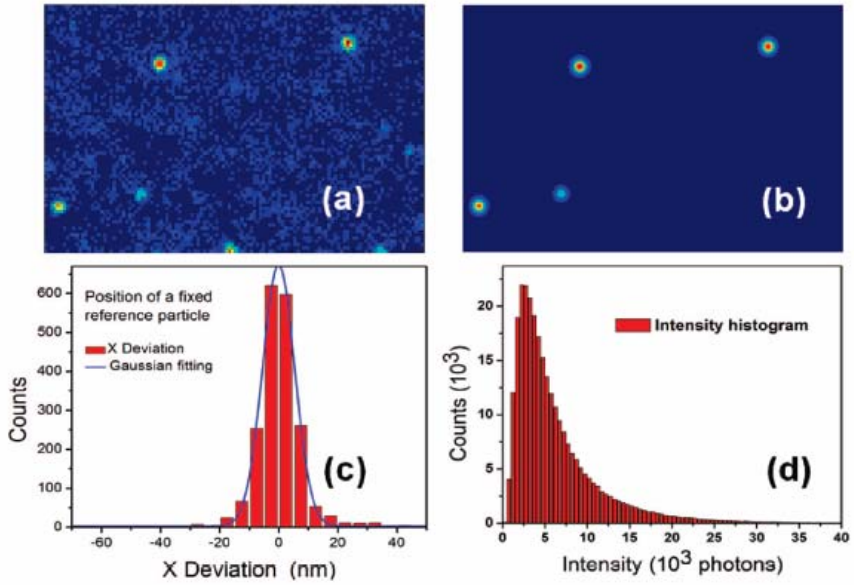

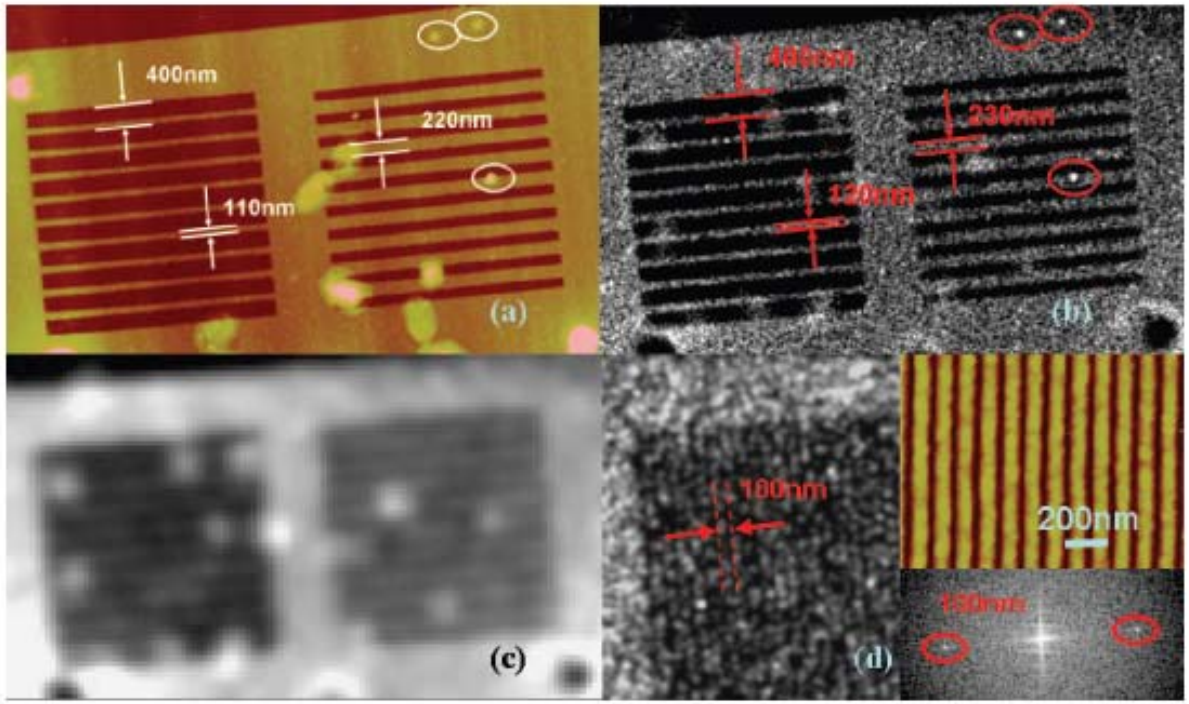

Figure 3. Experimental demonstration of super-resolution imaging. (a) AFM image of the PMMA nanograting structure as the object. The thickness of the PMMA is 60 nm. (b) Computer-rendered super-resolution image from sample in panel a. Each single molecule was rendered using a 2D Gaussian shape PSF with 18 nm fwhm. (c) Fluorescent image from unprocessed data in (b). (d) Super-resolution image of 100 nm period PMMA nanograting. Left image is the experimental result, the top-right image is the AFM measurement, and the bottom-right image is the 2D Fourier transform of the left image (two distinct peaks corresponding to the special frequency of the grating are encircled by red lines).